Development of Early Transition Metal Hydride Catalysts for Ammonia Synthesis

曹 禹

2023

Development of Early Transition Metal Hydride Catalysts for Ammonia Synthesis

A thesis submitted in fulfilment

of the requirements for the degree

of Doctor of Philosophy

Yu Cao

Supervisor: Professor Hiroshi Kageyama

2023

Department of Energy & Hydrogen Chemistry

Graduate School of Engineering

Kyoto University

Table of Contents

General Introduction

Haber-Bosch process

Ammonia is the main agricultural feedstock of synthetic fertilizers and also a potential hydrogen storage molecule.[1] The synthetic ammonia industry is based on the Haber-Bosch process, which involves the exothermic reaction between a mixture of nitrogen gas and hydrogen gas over iron-based catalysts promoted with K_2O and Al_2O_3 at 400−500 °C under high pressure (100−200 atm). High temperature could improve the reaction kinetics and high pressure could benefit a shift of the reaction equilibrium to the product ammonia. It is a high-energy consumption process and consumes 1%~2% of manmade energy per year. The demand of harsh reaction conditions is due to the considerable activation barrier of breaking the N≡N triple bond (bond energy 945 kJ/mol).[2] Therefore, it is of great significance for the development of ammonia synthesis process with low energy consumption and high thermodynamic efficiency.

Activation of Nitrogen. Since N_2 dissociation is usually regarded as the rate-limiting step in the Haber−Bosch process, it is crucial to identify catalyst capable of activating N_2. Catalysts based on transition metals, such as promoted Fe and Ru-based catalysts, have been used as the main effective catalysts for ammonia synthesis.[3] Transition metal atom has both occupied and empty *d* orbitals and the N_2 molecule has occupied bonding orbitals and empty antibonding π-orbitals (π^*), as shown in Figure 1a. By electron donation from N_2 occupied σ orbitals to the transition metal empty *d* orbital and a π backdonation from transition metal occupied *d* orbitals to the empty π^* antibonding orbitals of the N_2 molecules (Figure 1b), the N≡N bond is weakened.[4] The addition of electron donors, such as alkali and alkaline earth metal oxides, can further enhance the electron-donating power to N_2 antibonding π^* orbitals and benefit the cleavage of N_2. Recently, some electrides and hydride compounds, which have low work function, high electron density and strong reducing power, have been found to behave as outstanding support materials and/or promoters for Ru. The presence of electron and H^- in the support material was demonstrated to be of great significance for the excellent catalytic ammonia synthesis performance, which will be introduced later.

Nitrogen Fixation Pathways. Generally, catalytic nitrogen reduction involves the following fundamental steps: adsorption of N_2, hydrogenation of the adsorbed nitrogen, and the desorption of ammonia molecules. Depending on the adsorption and hydrogenation modes of N_2, the mechanisms can be classified into dissociative pathways and associative pathways.[5] On the typical heterogeneous catalysts in the conventional thermalcatalytic process, the N_2 reduction proceeds via a dissociative pathway, where the N≡N bond is cleaved firstly on the surface and then the adsorbed nitrogen is stepwise hydrogenated to form ammonia (Figure 2a). Different from the dissociation mechanism, the associative pathway achieves cleavage of the N≡N bond upon the release of ammonia molecules through two routes, i.e., the distal pathway and the alternating pathway. In the distal associative pathway, the terminal nitrogen is hydrogenated preferentially, releasing one ammonia molecule and then another adsorbed N atom is further hydrogenated to ammonia (Figure 2b). In the alternating associative pathway, the nitrogen atoms of adsorbed N_2 are hydrogenated

alternatively (Figure 2c). N_2 fixation on nitrogenases and organometallic complexes in biological and homogeneous catalysis is widely believed to proceed in the associative pathway, with the aid of multiple electrons and protons transfer. Recently, there are a few reports on heterogenous catalyst systems in which efficient N_2 activation and conversion to ammonia were performed via an associative mechanism, such as the well-defined Mo-hydride grafted on silica ([(≡Si–O–)MoH_x]),[6] Ni/LaN,[7] Li_4RuH_6,[8] Ru ACCs.[9] In these cases, N_2 is chemisorbed and activated on surface transition metal cluster centers or nitrogen vacancies sites and then undergo hydrogenation to release ammonia molecules.

Mars-van Krevelen mechanism. N_2 fixation can also be achieved via the Mars-van Krevelen (MvK) mechanism over metal nitrides, such as Co_3Mo_3N.[10] In this mechanism, the catalyst surface itself is an active part, i.e., the hydrogenation of lattice nitrogen in Co_3Mo_3N could occur, releasing ammonia and producing corresponding lattice vacancies which are subsequently replenished from gas phase N_2, as shown in Figure 3. It was demonstrated in the reaction of Co_3Mo_3N with Ar/H_2, where ammonia and Co_6Mo_6N phase were produced, indicating lattice N in Co_3Mo_3N are reactive and mobile. Further, heating Co_6Mo_6N in presence of H_2/N_2 or N_2 gas could regenerate back to Co_3Mo_3N.[11] Isotopic N exchange experiments also demonstrated that the lattice N was exchangeable in this system.[12] It should be noted that compared with the conventional associative and dissociative N_2 fixation mechanism, the first step in the MvK mechanism does not require the adsorption of N_2 to the pristine catalyst surface, which means that the formation of the first ammonia molecule does not involve the breaking down of the triple bond in the N_2 molecule, thus benefits a lower energy barrier of ammonia production. In addition to the above N-based MvK mechanism, ammonia synthesis over some hydride-catalysts have been reported to go through a H-based MvK mechanism, i.e., the lattice hydrides are involved in the ammonia production, which will be discussed later.

Sabatier principle and volcano curve. Highly active ammonia synthesis catalysts can be predicted based on the Sabatier principle, which states that the best catalysts should bind atoms or molecules with an intermediate binding energy: not too weak in order to be able to activate the reactants, and not too strong in order to be able

to desorb the products.[13] Therefore, the activity trends among various transition metals for ammonia synthesis can be clearly illustrated by a volcano curve (Figure 4), which displays the turnover frequency against nitrogen adsorption energy.[14] According to the Sabatier principle and the volcano curve, Fe, Ru-based catalysts are the optimal materials for the Haber-Bosch process because these materials have moderate nitrogen adsorption energy. However, early and late transition metals, which have either larger or smaller nitrogen adsorption energy, cannot catalyze ammonia synthesis effectively. A rational strategy for catalyst design is to combine the metals from each side of the volcano map, such as Co (which is too weakly binding with N) and Mo (which is too strongly binding with N), to arrive at an optimum nitrogen adsorption energy.[15] Interestingly, some impressive hydride catalyst systems have been reported as promising alternatives to the conventional fused-Fe and promoted-Ru catalysts, exhibiting the possibility to break the scaling rules.

Hydrides catalyzed ammonia synthesis

A hydride is a compound with negatively charged hydrogen anion (H^-). As opposed to other anions, H^- is highly flexible in size with ionic radii of 130-153 pm (found in metal hydrides).[16] H^- is recognized as a soft but strong Lewis base as well as a potent electron donor, allowing various applications in hydride ion conductivity, topochemical synthesis, catalysis, etc. One important field which has gained strong attention in recent years is the development of hydride catalysts for heterogenous nitrogen fixation to ammonia under mild reaction conditions.[17] Some representative works, including transition metal (TM)-LiH composite, complex hydrides, mixed-anion hydrides, electride hydrides, etc., as shown in Figure 5, will be summarized and discussed in the following part.

Complex hydrides. Complex hydride is a class of compounds with a general formula of $M(XH_n)_m$, where M is usually a metal cation and X is a metal or nonmetal element which sets up covalent or ionocovalent bonding with H.[18] Early 3*d* transition metals are not focal catalytic candidates for ammonia synthesis because they generally have strong affinities to N, which would hinder the conversion of intermediate to

products and exhibit negligible catalytic activity. Impressively, Chen group has developed a composite catalyst system of 3*d* early transition metals (nitrides)-LiH (TM spans from V to Ni), which can effectively break the volcano relationship through a two active center strategy,[19] where TM(N) is supposed to be the active site responsible for N_2 activation and dissociation, and LiH behaves as a strong reducing agent to remove the activated N from TM(N) to form [LiNH]. The generated [LiNH] could undergo the following hydrogenation to release ammonia molecule and regenerate LiH (Figure 6). Further investigations showed that other alkalis and alkaline earth hydrides, such as KH, BaH_2 and CaH_2, can synergize with Mn nitrides and thus lead to effective ammonia synthesis.[20]

Mechanistic investigations on LiH–Fe composite catalyst by gas-phase optical spectroscopy coupled with mass spectrometry and quantum chemical calculations revealed the existence of lithium-iron complex hydride (Li_4FeH_6) species at the surface/interface of the Fe-LiH catalyst, which may behave as the active centers to readily activate and hydrogenate N_2.[21] Later, ternary ruthenium complex hydrides (Li_4RuH_6 and Ba_2RuH_6) were developed for ammonia synthesis with superior activity under mild conditions.[8] Ba_2RuH_6/MgO significantly outperforms the most active Ru catalysts reported to date, and its activity at 523 K is over one order of magnitude higher than the benchmark Cs-promoted Ru/MgO catalyst. The DFT calculations show that the Li_4RuH_6 surface has electron-rich $[RuH_6]^{4-}$ centers for non-dissociative N_2 reduction.[22] The hydridic H transports electron and proton between the centers, and the Li cations stabilizes N_xH_y intermediates species (Figure 7).

Electride hydrides. Electrides are materials in which electrons behave as anions.[23] Due to the very low work function and high electron density, electrides could be used as electron-donor to Ru metal particles and therefore the N≡N bond is weakened as a result of back donation from Ru *d*-orbitals to the antibonding orbitals of N_2.[24] An inorganic electride $[Ca_{24}Al_{28}O_{64}]^{4+}(e^-)_4$ (denoted as C12A7:e^-, in which electrons are occupied in the cages of C12A7 framework) supported Ru (Figure 8) has been reported to exhibit outstanding catalytic activity for ammonia synthesis under mild reaction conditions.[25] The smooth electron injection from C12A7:e^- to Ru activates N_2 with low activation barrier, indicating that the rate-determining step of

Ru/C12A7:e^- catalyzed ammonia synthesis is not N_2 dissociation but the subsequent N−H bond formation steps. Furthermore, the dissociative adsorption hydrogen atoms on the Ru surface could spill over onto C12A7:e^- and be captured as H^- in the nanocages via the reaction with electrons in the cages.[26] Such smooth reversible exchangeability between electrons and H^- ions at low temperatures would prevent the strong adsorption of hydrogen in the Ru surface and therefore suppress hydrogen poisoning of the Ru.

In addition, it has been reported that a two-dimensional electride, $Ca_2N:e^-$ combined with ruthenium nanoparticles (Ru/$Ca_2N:e^-$) exhibits efficient and stable catalytic activity down to 200 ºC. $Ca_2N:e^-$ could be completely converted into Ca_2NH during the ammonia synthesis and the high catalytic activity of Ru/Ca_2NH would be ascribed to a unique feature of H^- ion such as the strong reducing power.[27] Furthermore, the formation of an N−H bond proceeds through a lattice H^- ion-mediated Mars−van Krevelen (MvK) type mechanism (Figure 9). The computational results suggest that surface electride, $[Ca_2N]^+ \cdot H_{1-x}^- e_x^-$ are formed by Ru catalysts during the reaction, and the formation of the low work function surface facilitates N_2 dissociation on the Ru surface via electron transfers from the anionic electrons to the supported Ru particles.

Mixed-anion hydrides. A mixed-anion compound is a solid-state material containing more than one anionic species in a single phase, such as oxyhydrides, which contain oxide and negatively charged hydride ions. The hydrogen anion within an oxide framework is easily exchangeable and thus can lead to unique chemical transformations.[28] We have developed a mixed-anion hydride compound $BaTiO_{3-x}H_x$ for ammonia synthesis,[29] which has activity comparable to conventional supported Ru catalysts such as Cs-Ru/MgO or Ru/$BaTiO_3$. It was proposed that the H^- in the $BaTiO_{2.5}H_{0.5}$ lattice may take part in the catalysis via a hydrogen-based Mars van Krevelen mechanism. Interestingly, conventional scaling rules predict no activity of Ti element due to strong nitrogen adsorption energy, but by introducing hydride, the formerly overlooked metal behaves as an active catalyst without resorting to precious metals. In addition, the synthesis activity of ammonia is examined when Ru, Fe, and Co particles are supported onto the oxyhydride $BaTiO_{2.5}H_{0.5}$. The activity for Fe and

Co increases by a factor of 70–400, making them more active than Ru/MgO which is a conventional Ru catalyst.[30] Later, we found *Ln*HO (*Ln* = Sm, Gd) supported Ru catalysts exhibited superior catalytic activity rate than $BaTiO_{2.5}H_{0.5}$, which could be due to the pressure induced anion order-disorder transition (H^-/O^{2-}) making the hydride size flexible with easy H^- diffusion during the reaction.[31] Moreover, various hydride-based materials, such as $LnH_{3-2x}O_x$ (*Ln* = La, Ce, Y),[32] $BaCeO_{3-x}N_yH_z$,[33] CaHF,[34] Ba-Cr-N-H,[35] etc., have been examined as attractive catalysts and/or catalytic supports for Ru catalysts, demonstrating that hydride materials have high potential for ammonia synthesis. The critical roles for hydrides in recent investigations on the nitrogen fixation with enhanced catalytic performance is summarized in Figure 10. In general, hydrides have strong electron-donating capabilities and could benefit N≡N bond cleavage. The high hydrogen lability and diffusion (solubility) could lead to suppression of hydrogen poisoning effect. In addition, the scaling relations can be even broken or circumvented, providing more possibilities for searching efficient catalysts for ammonia synthesis.

Aims and outline

Ammonia is not only vital for the production of fertilizers and industrial chemicals, but also a potential hydrogen storage material and future fuel alternative. The development of new and efficient ammonia synthesis catalysts is extremely challenging, especially for ammonia synthesis under mild reaction conditions. In addition, early or late transition metals are incapable to catalyze this reaction efficiently, because they have either larger or smaller nitrogen adsorption energy, leading to poor turnover rates. Recent works have shown the great possibility to break scaling relations by hydride catalysts with superior catalytic performance. There is still much to discover about the scientific principles and technological applications of early transition metal hydrides for ammonia synthesis. The typical problems include: the bulk structure and hydride composition need to be further optimized; the activity is still low and the reaction conditions are at high pressure/high temperature; there is an enhancement of activity by introducing hydrides into the early transition metals, however there is no

real data to explain such hydride-promoting mechanism, thus it is necessary to go deeper and know why hydrides work; how to expand the scope of catalytically active metals as well as hydride catalysts.

The previous research results of our group, i.e., TiH_2 and $BaTiO_{2.5}H_{0.5}$,[29] showed that by introducing hydride, the repertoire of heterogeneous catalysts can be expanded to include formerly overlooked early transition metal elements and unexamined compositions without resorting to precious metals. Therefore, in this thesis, the goal is to keep finding whether such kinds of "dead elements" for ammonia synthesis will have their springtime. The author focused on the development of ammonia synthesis over several early transition metal-based hydride catalysts, including $VH_{0.39}$, $NbH_{0.6}$, Ca_3CrN_3H and $ZrCr_2N_xH_y$ compounds, and investigated their ammonia synthesis performance and catalytic reaction mechanism. The main contents include the following aspects:

(1) Early transition metal hydride compounds $VH_{0.39}$ and $NbH_{0.6}$ were developed as catalysts for ammonia synthesis. A number of strategies were used to realize the superior activity of vanadium for this reaction, including introducing hydrides within the early transition metal catalysts; optimizing structures with enhancing facile diffusion of hydride/nitride through the bulk lattice; choosing elements with suitable M-N bond strengths. The approach is very unique due to the activity of vanadium hydride, most likely with an active composition of $VH_{0.44}N_{0.16}$, is superior to the previously reported TiH_2 and $BaTiO_{2.5}H_{0.5}$, and comparable to the noble metal catalyst Cs-Ru/MgO at 400 °C and 5 MPa. These results show that there is more potential for developing new single-phase hydride catalysts of previously overlooked elements without sacrificing activity.

(2) It is of much scientific importance to further develop new compounds as ammonia synthesis catalysts and find out effective approaches for N_2-to-NH_3 conversion. Topochemical reactions have led to great progress in the discovery of new metastable compounds with novel chemical and physical properties. With these reactions, the overall crystal structure of the host material is generally maintained. Here the author reported a topochemical synthesis of a hexagonal nitride hydride, *h*-Ca_3CrN_3H, by heating an orthorhombic nitride, *o*-Ca_3CrN_3, under hydrogen gas at 673

K, accompanied by a rotational structural transformation. The hydrogen intercalation modifies the Ca-N rock-salt-like atomic packing in *o*-Ca_3CrN_3 to a face-sharing octahedral chain in *h*-Ca_3CrN_3H, mimicking a 'hinged tessellation' movement. Impressively, the new compound *h*-Ca_3CrN_3H exhibited stable ammonia synthesis activity when used as ammonia synthesis catalyst. The catalytic performance is interesting, considering that Cr metal is not active element for ammonia synthesis.

(3) The author has unexpectedly found a topochemical synthesis involving an unusual structural transformation from orthorhombic Ca_3CrN_3 to hexagonal antiperovskite Ca_3CrN_3H which possesses ammonia synthesis activity. Here, the catalytic performance of this new Ca_3CrN_3H compound and the mechanistic details for dinitrogen reduction and ammonia formation over the Ca_3CrN_3H catalyst are further explored experimentally and theoretically. Ca_3CrN_3H exhibits superior ammonia synthesis activity and the absence of hydrogen poisoning is presumably associated with the facile hydride diffusion within face-shared 1-D octahedral channel of Ca_3CrN_3H, as well as the superior hydrogen exchangeability of lattice hydride with reactant H_2 gas. DFT calculations reveal that ammonia synthesis proceeds through an associative mechanism. The surface Ca_3 hollow sites formed at the Ca_3CrN_3H (001) surface play a critical role in N_2 adsorption and activation to the successive hydrogenation.

(4) Early transition metal-based intermetallic compounds, such as AB_2 (e.g. ZrV_2, $ZrMn_2$, $ZrCr_2$), can reversibly absorb large amounts of hydrogen and are of great interest for hydrogen storage. It has been widely accepted that dissociative hydrogen chemisorption could proceed easily on the surface, allowing the rapid formation of intermetallic hydrides. Such intermetallic hydride compounds could exhibit various interesting surface properties and will presumably be catalytically active for ammonia synthesis. Here the author found a dissociative hydrogen chemisorption together with nitrogen storage proceed on AB_2-type Laves phase intermetallic compounds, $ZrCr_2$, to form intermetallic nitride hydrides. The potential of Zr-based AB_2-type intermetallic hydrides as ammonia synthesis catalysts was further explored.

References

[1] R. Schlögl, *Angew. Chem. Int. Ed.* **2003**, *42*, 2004–2008.

[2] S. L. Foster, S. I. P. Bakovic, R. D. Duda, S. Maheshwari, R. D. Milton, S. D. Minteer, M. J. Janik, J. N. Renner, L. F. Greenlee, *Nat. Catal.* **2018**, *1*, 490–500; Q. Wang, J. Guo, P. Chen, *J. Energy Chem.* **2019**, *36*, 25–36.

[3] V. S. Marakatti, E. M. Gaigneaux, *ChemCatChem* **2020**, *12*, 5838–5857; J. Humphreys, R. Lan, S. Tao, *Adv. Energy Sustain. Res.* **2021**, *2*, 2000043.

[4] S. Wang, F. Ichihara, H. Pang, H. Chen, J. Ye, *Adv. Funct. Mater.* **2018**, *28*, 1803309.

[5] H. Fang, D. Liu, Y. Luo, Y. Zhou, S. Liang, X. Wang, B. Lin, L. Jiang, *ACS Catal.* **2022**, *12*, 3938–3954.

[6] L. M. Azofra, N. Morlanés, A. Poater, M. K. Samantaray, B. Vidjayacoumar, K. Albahily, L. Cavallo, J. M. Basset, *Angew. Chem. Int. Ed.* **2018**, *57*, 15812–15816.

[7] T. N. Ye, S. W. Park, Y. Lu, J. Li, M. Sasase, M. Kitano, T. Tada, H. Hosono, *Nature* **2020**, *583*, 391–395.

[8] Q. Wang, J. Pan, J. Guo, H. A. Hansen, H. Xie, L. Jiang, L. Hua, H. Li, Y. Guan, P. Wang, W. Gao, L. Liu, H. Cao, Z. Xiong, T. Vegge, P. Chen, *Nat. Catal.* **2021**, *4*, 959–967.

[9] L. Li, Y. F. Jiang, T. Zhang, H. Cai, Y. Zhou, B. Lin, X. Lin, Y. Zheng, L. Zheng, X. Wang, C. Q. Xu, C. tong Au, L. Jiang, J. Li, *Chem* **2022**, *8*, 749–768.

[10] Z. Qiao, D. Johnson, A. Djire, *Cell Rep. Phys. Sci.* **2021**, *2*, 100438.

[11] D. Mckay, D. H. Gregory, J. S. J. Hargreaves, S. M. Hunter, X. Sun, *Chem. Commun.* **2007**, 3051–3053.

[12] S. M. Hunter, D. H. Gregory, J. S. J. Hargreaves, M. Richard, D. Duprez, N. Bion, *ACS Catal.* **2013**, *3*, 1719–1725.

[13] A. Vojvodic, J. K. Nørskov, *Natl. Sci. Rev.* **2015**, *2*, 140–143.

[14] A. J. Medford, A. Vojvodic, J. S. Hummelshøj, J. Voss, F. Abild-Pedersen, F. Studt, T. Bligaard, A. Nilsson, J. K. Nørskov, *J. Catal.* **2015**, *328*, 36–42.

[15] R. Kojima, K. I. Aika, *Chem. Lett.* **2000**, *1*, 514–515; C. J. H. Jacobsen, S. Dahl, B. S. Clausen, S. Bahn, A. Logadottir, J. K. Nørskov, *J. Am. Chem. Soc.* **2001**, *123*, 8404–8405.

[16] H. Kageyama, K. Hayashi, K. Maeda, J. P. Attfield, Z. Hiroi, J. M. Rondinelli, K. R. Poeppelmeier, *Nat. Commun.* **2018**, *9*, 772.

[17] Q. Wang, J. Guo, P. Chen, *Joule* **2020**, *4*, 705–709; Q. Wang, Y. Guan, J. Guo, P. Chen, *Cell Rep. Phys. Sci.* **2022**, *3*, 100779.

[18] T. He, H. Cao, P. Chen, *Adv. Mater.* **2019**, 1902757; J. Guo, P. Chen, *Acc. Chem. Res.* **2021**, *54*, 2434–2444.
[19] P. Wang, F. Chang, W. Gao, J. Guo, G. Wu, T. He, P. Chen, *Nat. Chem.* **2017**, *9*, 64–70.
[20] F. Chang, Y. Guan, X. Chang, J. Guo, P. Wang, W. Gao, G. Wu, J. Zheng, X. Li, P. Chen, *J. Am. Chem. Soc.* **2018**, *140*, 14799–14806.
[21] P. Wang, H. Xie, J. Guo, Z. Zhao, X. Kong, W. Gao, F. Chang, T. He, G. Wu, M. Chen, L. Jiang, P. Chen, *Angew. Chem. Int. Ed.* **2017**, *56*, 8716–8720.
[22] C. Liu, Q. Wang, J. Guo, T. Vegge, P. Chen, H. A. Hansen, *ACS Catal.* **2022**, *12*, 4194–4202; Q. Wang, J. Guo, P. Chen, *Chem* **2021**, *7*, 3203–3220.
[23] H. Hosono, M. Kitano, *Chem. Rev.* **2021**, *121*, 3121–3185.
[24] M. Hara, M. Kitano, H. Hosono, *ACS Catal.* **2017**, *7*, 2313–2324.
[25] M. Kitano, Y. Inoue, Y. Yamazaki, F. Hayashi, S. Kanbara, S. Matsuishi, T. Yokoyama, S.-W. Kim, M. Hara, H. Hosono, *Nat. Chem.* **2012**, *4*, 934–940.
[26] M. Kitano, S. Kanbara, Y. Inoue, N. Kuganathan, P. v. Sushko, T. Yokoyama, M. Hara, H. Hosono, *Nat. Commun.* **2015**, *6*, 6731.
[27] M. Kitano, Y. Inoue, H. Ishikawa, K. Yamagata, T. Nakao, T. Tada, S. Matsuishi, T. Yokoyama, M. Hara, H. Hosono, *Chem. Sci.* **2016**, *7*, 4036–4043.
[28] Y. Kobayashi, O. J. Hernandez, T. Sakaguchi, T. Yajima, T. Roisnel, Y. Tsujimoto, M. Morita, Y. Noda, Y. Mogami, A. Kitada, M. Ohkura, S. Hosokawa, Z. Li, K. Hayashi, Y. Kusano, J. E. Kim, N. Tsuji, A. Fujiwara, Y. Matsushita, K. Yoshimura, K. Takegoshi, M. Inoue, M. Takano, H. Kageyama, *Nat. Mater.* **2012**, *11*, 507–511; T. Yajima, F. Takeiri, K. Aidzu, H. Akamatsu, K. Fujita, W. Yoshimune, M. Ohkura, S. Lei, V. Gopalan, K. Tanaka, C. M. Brown, M. A. Green, T. Yamamoto, Y. Kobayashi, H. Kageyama, *Nat. Chem.* **2015**, *7*, 1017–1023; Y. Tang, Y. Kobayashi, K. Shitara, A. Konishi, A. Kuwabara, T. Nakashima, C. Tassel, T. Yamamoto, H. Kageyama, *Chem. Mater.* **2017**, *29*, 8187–8194.
[29] Y. Kobayashi, Y. Tang, T. Kageyama, H. Yamashita, N. Masuda, S. Hosokawa, H. Kageyama, *J. Am. Chem. Soc.* **2017**, *139*, 18240–18246.
[30] Y. Tang, Y. Kobayashi, N. Masuda, Y. Uchida, H. Okamoto, T. Kageyama, S. Hosokawa, F. Loyer, K. Mitsuhara, K. Yamanaka, Y. Tamenori, C. Tassel, T. Yamamoto, T. Tanaka, H. Kageyama, *Adv. Energy Mater.* **2018**, 1801772.
[31] H. Yamashita, T. Broux, Y. Kobayashi, F. Takeiri, H. Ubukata, T. Zhu, M. A. Hayward, K. Fujii, M. Yashima, K. Shitara, A. Kuwabara, T. Murakami, H. Kageyama, *J. Am. Chem. Soc.* **2018**, *140*, 11170–11173.

[32] K. Ooya, J. Li, K. Fukui, S. Iimura, T. Nakao, K. Ogasawara, M. Sasase, H. Abe, Y. Niwa, M. Kitano, H. Hosono, *Adv. Energy Mater.* **2021**, *11*, 2003723.
[33] M. Kitano, J. Kujirai, K. Ogasawara, S. Matsuishi, T. Tada, H. Abe, Y. Niwa, H. Hosono, *J. Am. Chem. Soc.* **2019**, *141*, 20344–20353.
[34] M. Hattori, S. Iijima, T. Nakao, H. Hosono, M. Hara, *Nat. Commun.* **2020**, *11*, 2001.
[35] Y. Guan, W. Zhang, Q. Wang, C. Weidenthaler, A. Wu, W. Gao, Q. Pei, H. Yan, J. Cui, H. Wu, S. Feng, R. Wang, H. Cao, X. Ju, L. Liu, T. He, J. Guo, P. Chen, *Chem Catal.* **2021**, 1042–1054.

Figures

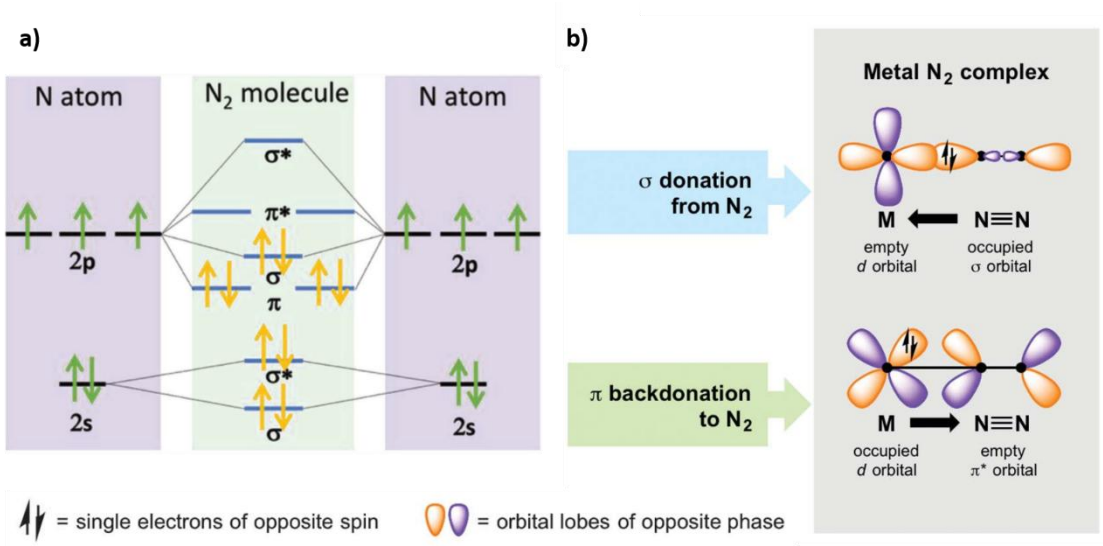

Figure 1. a) The diagrams of N atomic orbitals and their hybridization of N_2 molecular orbitals. b) Simplified schematic of bonding end-on-bound transition metal N_2 complexes. Reproduced from ref. 4.

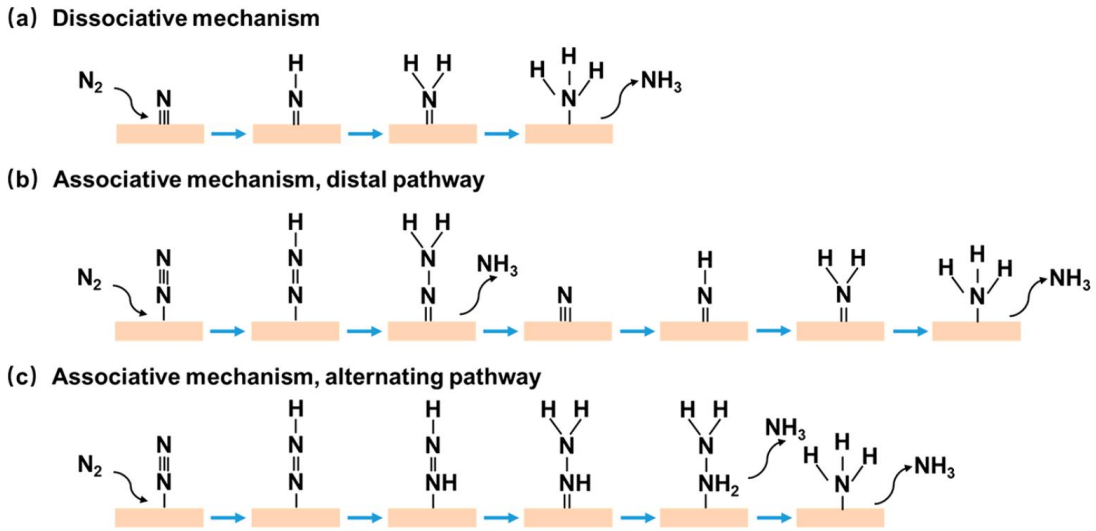

Figure 2. Possible reaction mechanisms for N_2 reduction to ammonia. Reproduced from ref. 5.

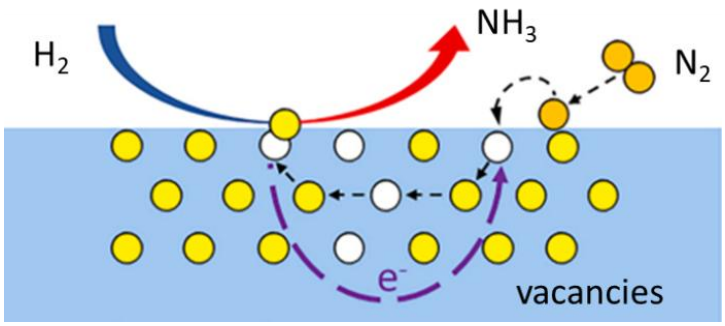

Figure 3. The MvK mechanism of ammonia synthesis over Co_3Mo_3N catalysts.

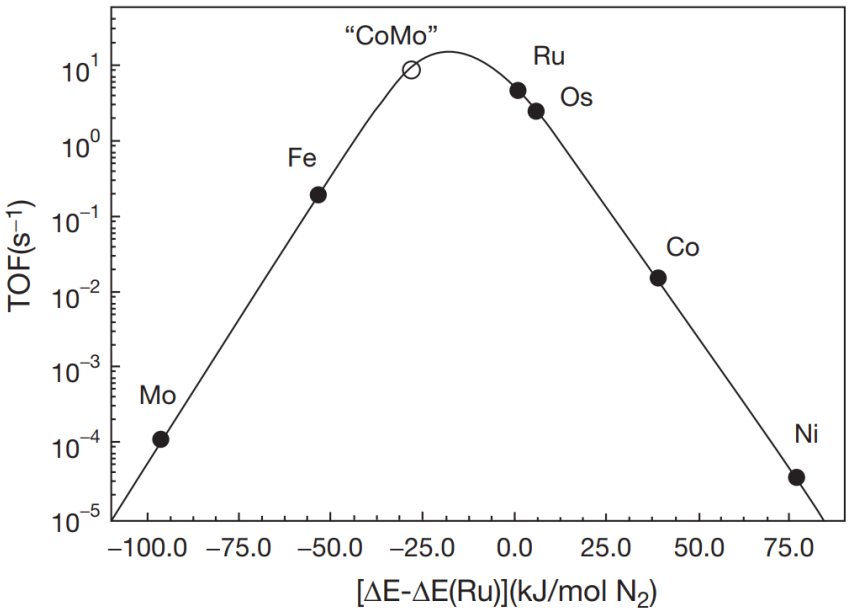

Figure 4. Scaling relationship and volcano curve. Reproduced from ref. 15.

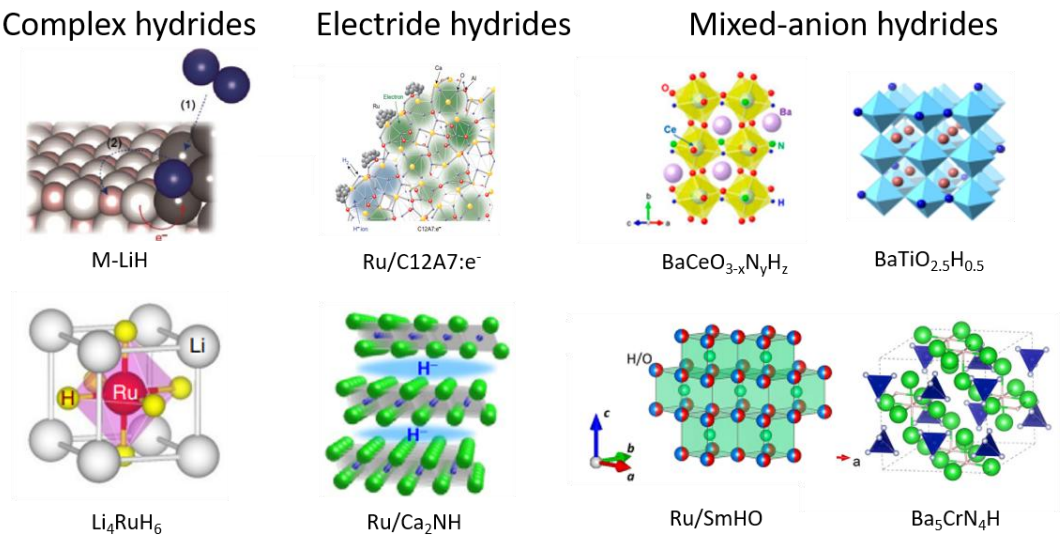

Figure 5. Representative heterogenous hydride catalysts for nitrogen fixation to ammonia. Reproduced from refs. 8, 19, 23, 29, 31 and 35.

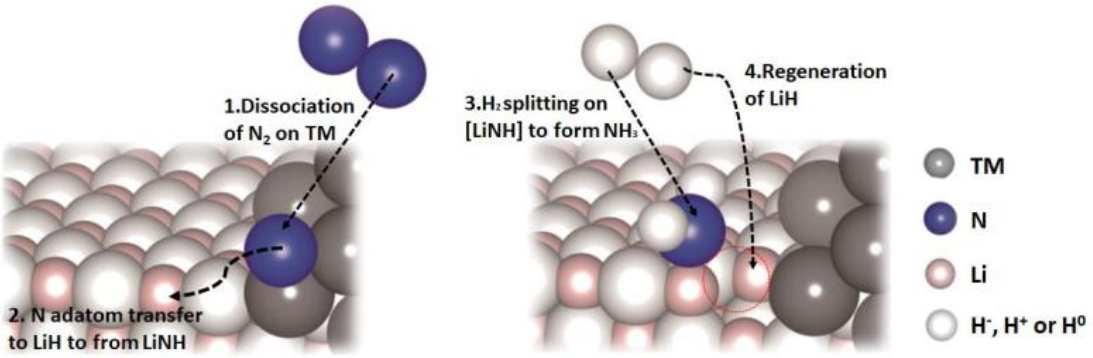

Figure 6. Possible pathway for the ammonia synthesis over TM-LiH composite catalyst. Reproduced from ref. 19.

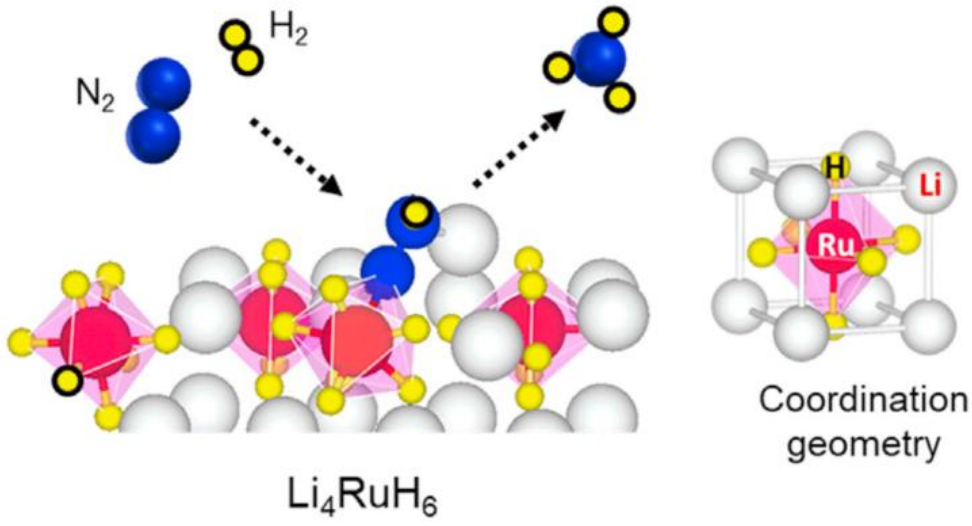

Figure 7. The coordination of Li_4RuH_6 and the possible reaction pathway of ammonia synthesis over Li_4RuH_6 surface. Reproduced from ref. 22.

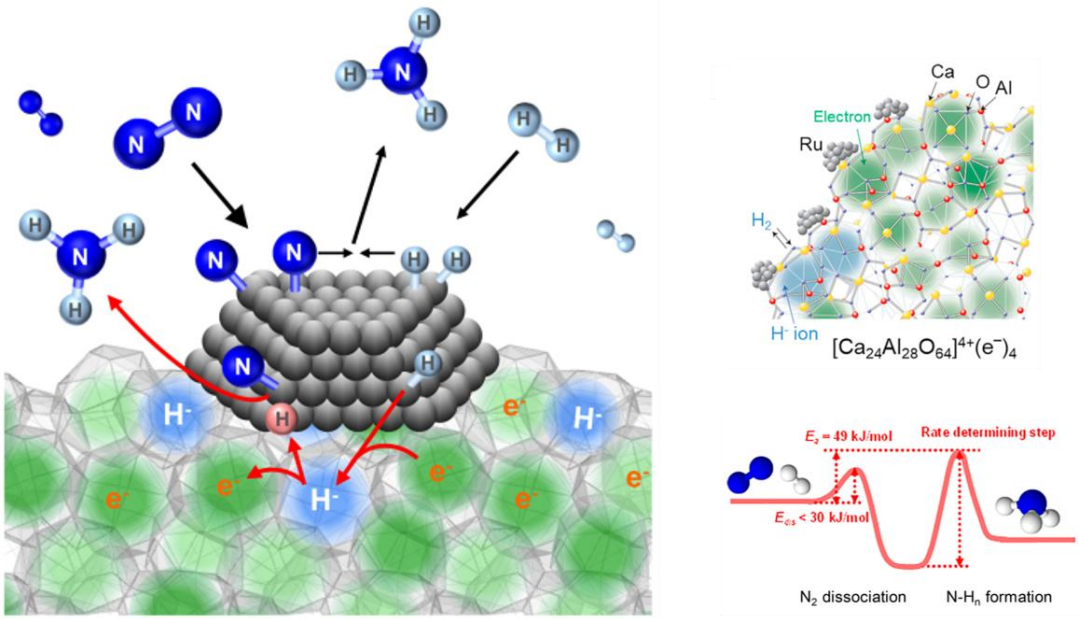

Figure 8. Schematic model of Ru/C12A7:e^- and possible pathway for the ammonia synthesis over Ru/C12A7:e^-: H captured at the cages of C12A7:e^- to form H^- (prevents H poisoning); H^- reacted with N species on Ru; e^- regenerated in the cage of C12A7. Reproduced from ref. 23.

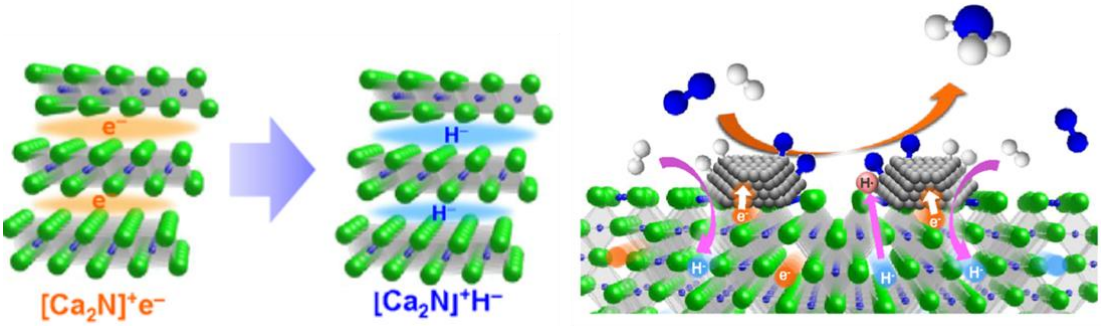

Figure 9. Schematic illustration of structural conversion of $Ca_2N{:}e^-$ into Ca_2NH during ammonia synthesis and the ammonia synthesis mechanism over Ru/Ca_2NH. Reproduced from ref. 23.

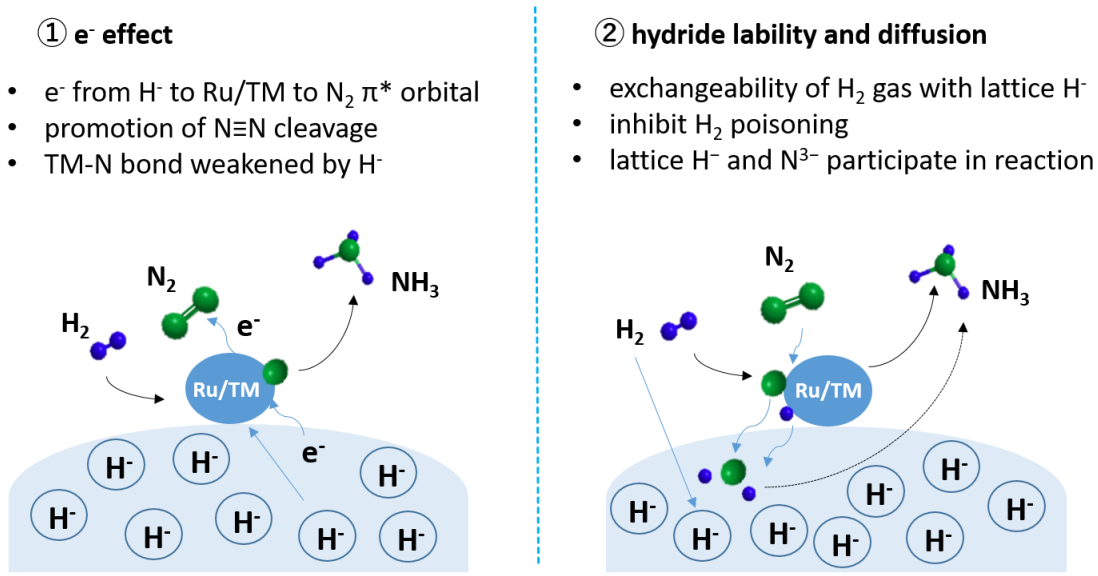

Figure 10. The critical roles for hydrides in recent investigations on the nitrogen fixation.

Chapter 1.

Vanadium Hydride as an Ammonia Synthesis Catalyst

1.1. Introduction

The Haber-Bosch process is a mainstay reaction for the synthesis of ammonia, which is not only vital for the production of fertilizers and industrial chemicals, but also a potential hydrogen storage material and future fuel alternative.[1] Enormous effort has been made in developing transition metal catalysts for ammonia synthesis in the last decade.[2] The activity trends among various metals can be clearly illustrated by a 'volcano' curve, which displays the turnover frequency against the heat of the adsorption of nitrogen on the catalyst particle.[3] Hence, in general, active elements are limited to mid-to-late transition metals (e.g., Ru, Fe, Co, etc.),[4] and only a few early 3*d* transition metals (e.g., from Sc to Mn) are capable to catalyze this reaction

efficiently.[5-7] Normally, these early 3*d* transition metals bind adsorbates too strongly, leading to poor turnover rates.

It will be interesting to find whether such kinds of "dead elements" for ammonia synthesis will have their springtime. There are a few cases of breaking scaling rules. Chen *et al*. have reported LiH or other alkali and alkaline earth hydrides assisting early 3*d* transition metals, including vanadium, via nitrogen transfer and hydrogenation processes.[5,6] Another successful example is our previous report of the hydride-containing titanium-based compounds (TiH_2 and $BaTiO_{2.5}H_{0.5}$) as catalysts for ammonia synthesis without any Ru or Fe; here Ti is the active center.[7] The presence of hydride is critical for activating nitrogen and its subsequent hydrogenation to form ammonia. By introducing hydride, the repertoire of heterogeneous catalysts can be expanded to include formerly unexamined composition without resorting to precious metals. These results imply that other early transition metals may also act as active catalysts when combined with hydrides.

In all of these studies with TiH_2, $BaTiO_{2.5}H_{0.5}$,[7] and more recently, by Kitano *et al.* with $BaCeO_{3-x}H_yN_z$,[8] there is evidence of a Mars-van Krevelen mechanism [9] of hydride (and nitride). This requires the facile diffusion of hydride/nitride species throughout the bulk lattice. TiH_2, and more indirectly, the perovskites $BaTiO_{2.5}H_{0.5}$ and $BaCeO_{3-x}H_yN_z$ are all based on face-centered cubic (fcc) type close-packed structures. We suspected that if all other conditions are the same, then the more open body-centered cubic (bcc)-based structures should have better hydride/nitride diffusion, and hence higher catalytic activity. Certain transition metals and their hydrides, such as V, V_2H, Nb, and NbH are all based on bcc metal arrangements, and this is why vanadium metal is used for hydrogen separation membranes.[10] In fact, a vanadium membrane reactor has been used to demonstrate NH_3 synthesis, but with very small apparent yield.[11] On top of this, as we discuss later, V and Nb have relatively low M-N bond energies among the early transition metals, which should be beneficial for catalytic activity. On a different note, recently, vanadium complexes bearing anionic pyrrole-based PNP-type pincer and aryloxy ligands have been developed for homogeneous nitrogen fixation into ammonia and hydrazine under mild reaction conditions.[12] Hence

there is much motivation to further test these early transition metal hydrides for activity with ammonia synthesis.

1.2. Experimental

Preparation of Catalysts. Commercial samples of VH_x (99%, Kojundo Chemical Lab. Co., Ltd., powder 150 μm mesh, x = 0.39 which has been determined by combustion elemental analysis), TiH_2 (98%, Aldrich), vanadium (99.9%, Kojundo Chemical Lab. Co., Ltd., powder 300 μm mesh), VN and ZrH_2 (99%, Alfa Aesar, 325 mesh powder) were milled using a high-energy planetary ball mill (Fritsch P5). Each sample was put into an Ar-filled alumina pot with alumina balls and was ball-milled for 12 hrs at a rotation speed of 240 rpm before the catalytic test to reduce the size of particle (the final surface area ~1.5 m^2/g) and expose non-oxidized surfaces. $NbH_{0.6}$ was synthesized by mechanical alloying as reported previously.[13] Here, a 1.5g commercial sample of Nb (99%, Kojundo Chemical Lab. Co., Ltd., *ca.* 20 μm) was charged to a gas-tight milling pot in a N_2 glovebox, after which the atmosphere was exchanged by repeatedly introducing H_2 (2.5 atm, 6 times). The sample was then ball-milled with intermittent H_2 introduction (10 hrs milling, 3 times at 320 rpm). All the milled powders were subsequently handled under argon or nitrogen.

Ammonia synthesis. A 0.1 g sample of each catalyst was suspended in a 3/8" stainless steel tube on a bed of quartz wool. Blank tests using the reactor tube and quartz wool did not give any measurable catalytic activity. Catalyst samples were initially treated with flowing H_2 (90 mL/min) at 400 °C at a heating and cooling rate of 6 °C/min. Catalytic runs were then conducted at 5 MPa (gauge pressure), with a flow rate of 110 sccm. Unless otherwise noted, the synthesis gas composition was N_2 : H_2 : Ar = 22.5 : 67.5 : 10, where Ar was initially intended to serve as an internal standard for calibrating a mass spectrometer. Commercially supplied gases with O_2 < 2 ppm and H_2O < 5 ppm were purified with an in-line H_2O/O_2 filter to achieve ppt-level purity. Ammonia formation was quantified by an aqueous trap (1.87×10^{-5} M NH_4Cl, 333 mL) and an ammonia-selective electrode (Horiba X 5002A).

Kinetic Studies. Apparent activation energies were measured at 5 MPa, over temperatures range from 325 to 400 °C, with a flow rate of 110 mL min^{-1} in both heating and cooling processes. For N_2 and H_2 reaction order measurements, gas compositions of N_2:H_2:Ar were 10:50:40, 16.7:50:33.3, 25:50:25, and 33.3:50:16.7 for determining the N_2 order, and 16.7:33.3:50, 16.7:50:33.3, and 16.7:83.3:0 for determining the H_2 order. All measurements were conducted at 5 MPa, 400 °C at a flow rate of 110 mL min^{-1}. Reaction orders of NH_3 were determined by varying the conversion rate, achieved by changing the flow rate of the gas (22.5:67.5:10) between 50, 110, 150, and 200 mL min^{-1}. The data were analyzed using the method of Aika et al.[14]

H/D exchange. A sample of ball-milled $VH_{0.39}$ or TiH_2 (approx. 20 mg) was loaded into a Pt pan without exposure to air by covering with a small amount of dry hexane. The Pt pan was then loaded into a Netzsch TG-DTA2000SE/H system coupled to a Bruker MS9610. The hexane was removed under D_2/Ar flow (5 : 95) at 80 ˚C for 0.5 h, and then ramped to 800 ˚C at various heating rates while downstream gases were monitored.

Catalyst characterization. Powder X-ray diffraction (XRD) patterns were collected by sealing samples in capillaries and using a Bruker Advance D8 diffractometer (Bruker) with Mo K_α radiation in Debye-Scherrer geometry. Combustion elemental analysis for nitrogen was conducted at the School of Pharmacy, Kyoto University. Surface areas were obtained by a MicrotracBEL BELSORP mini II instrument (MicrotracBEL Corp.) using nitrogen adsorption and a single-point BET method.

Bottleneck calculation. Hydride diffusion has been discussed in terms of bottleneck. Hydride migrate between the lattice and interstitial sites through the face of a triangle bounded on one side by the B cation and other two nearest-neighbor A cations. The center of the void is determined by the three cations and the inscribed circle represents the position of the minimum energy path for hydride migration.

1) V_2D

The bottleneck radius, R_{bn}, of the V_2D (alpha 655083 *Im*-3*m*) is defined by[15]

$$R_{bn} = a_0\left(\frac{3}{4}a_0 - \sqrt{2}r_B\right) - [(r_A - r_B)(r_A + r_B)] \times \left[2(r_A - r_B) + \sqrt{2}a_0\right]^{-1}$$

a_0 - lattice parameter - 3.140 Å; r_A - radius of the A cation - 1.34 Å; r_B - radius of the B cation (In this case, A and B are both vanadium, thus r_A equals r_B); R_{bn} = 1.4443 Å.

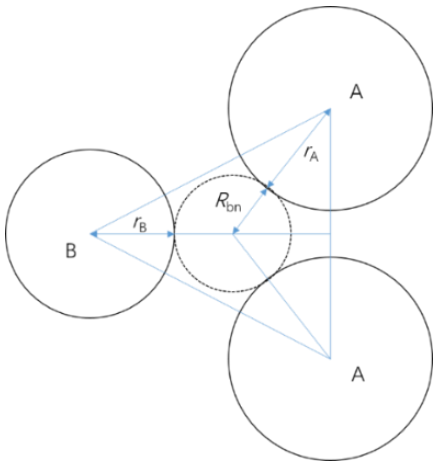

2) TiH_2

The bottleneck radius, R_{bn}, of the cubic *fl*uorite TiH_2 (*Fm*-3*m*) is de*fi*ned by[16]

$$R_{bn} = \frac{l_{A-A}}{\sqrt{3}} - r_A$$

$l_{A\text{-}A}$ - the distance between A cations - 3.154 Å; r_A - radius of the A cation - 0.75 Å; R_{bn} = 1.0710 Å.

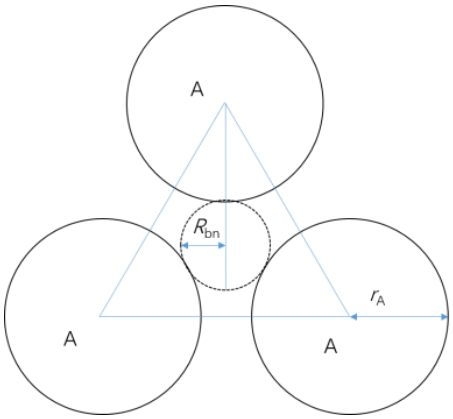

1.3. Results and discussions

We conducted ammonia synthesis tests on milled samples of $VH_{0.39}$, TiH_2, V, VN, $NbH_{0.6}$, and ZrH_2 and compared them to the well-known Ru catalyst Cs-

Ru/MgO.[17,18a] The results, obtained at 400 °C under 5 MPa, are shown in Figure 1-1. $VH_{0.39}$ demonstrated an excellent catalytic activity (3.2 mmol·g^{-1}·h^{-1}) for the first 12 hours, superior to Cs-Ru/MgO (2.7 mmol·g^{-1}·h^{-1}) despite the lack of ruthenium. The presence of hydride seems to be critical for the high activity of $VH_{0.39}$, since V nor VN are not significantly active under our probed conditions. We further note that $VH_{0.39}$ exhibited higher catalytic activity than previously reported TiH_2 (2.2 mmol·g^{-1}·h^{-1}), at least for its initial activity. $NbH_{0.6}$ also exhibited activity (0.4 mmol·g^{-1}·h^{-1}), while ZrH_2 proved to be inactive.

To examine the stability of the $VH_{0.39}$ catalyst, the reaction time was extended. As shown in Figure 1-2, a deactivation is noticeable at the early stage of the reaction and afterwards the conversion stabilizes in steady-state conditions, showing good stability even after 7 days (2.0 mmol·g^{-1}·h^{-1}) with the final turnover number (TON) (with respect to lattice hydride) greater than 130. We suspect that during ammonia synthesis, $VH_{0.39}$ is converted into $VH_{0.44}N_{0.16}$, which is the stable active composition. Such partial nitridation occurs for $BaTi(O, H)_3$ perovskite.[7] The nitride formation during the initial period may lead to slight deactivation. Despite slight nitride formation, there is no noticeable further convesion to VN under the experimental conditions, indicating the catalyst is (meta)stable. We were unable to conduct a stability test for Cs-Ru/MgO, but a recent study has reported the activity of Cs-Ru/MgO over 100 h.[18b] It was shown that the stability of Cs-Ru/MgO (at 360˚C, 1.0 MPa) begins to decrease from about 30 h. For $VH_{0.39,}$ deactivation takes place at an early stage of the reaction at 400 °C, 5 MPa, and then the conversion stabilizes under steady-state conditions and displays good stability even after 7 days. This result indicates the stability of $VH_{0.39}$ in Fig. 1(b) is at least comparable to Cs-Ru/MgO.

We have also conducted H/D exchange reactions, by passing D_2 over the hydride samples while heating, and examining HD release peak temperatures downstream (Figure 1-3). Our previous studies with NaH and other oxyhydrides show that this can be used as a measure of hydride exchangeability or diffusion.[19] This in turn can be related to the catalytic activity for these hydride-type catalysts. In general, the $VH_{0.39}$ sample shows a significantly lower H/D exchange temperature (300 ~ 350 ˚C, in blue) compared to titanium hydride (450 ~ 700 ˚C, in red). We conducted our

ammonia synthesis at 400 ˚C, so the $VH_{0.39}$ catalyst should be continuously exchanging hydrogen with the surrounding gas, while for TiH_2 this process is still somewhat limited.

As we have found with hydride-based catalysts in general, it is necessary to check the composition and structure of the catalyst after the reaction, as it often changes, and reflects the true nature of the catalyst better. Since $VH_{0.39}$ showed the highest activity, we focus on this catalyst. Combustion elemental analysis shows that the $VH_{0.39}$ composition increases in hydride and nitride content to an overall bulk composition of $VH_{0.44}N_{0.16}$ during ammonia synthesis. XRD patterns (Figure 1-4) show no noticeable VN peaks, but rather a slight increase in lattice parameter and cell volume. This can be largely ascribed to nitrogen incorporation, as the hydrogen content does not change as much as the nitrogen. As there have been no vanadium hydride-nitrides reported yet, it would be interesting to investigate this in a further study with careful neutron/X-ray diffraction measurements on more crystalline samples. In any event, the nitride-hydride composition again reminds us of the Mars van Krevelen mechanism and consequent activity for ammonia synthesis.

At this point, it is important to consider the various structures involved. In our previous paper, we summarized how Ti, TiH_2, and TiN are all related.[7] Ti metal is hexagonally close-packed (hcp), while for TiH_2 and TiN, there is a fcc-packed Ti atom lattice with hydride and nitride occupying tetrahedral and octahedral sites, respectively. V, though, has a bcc metal-packed structure [20] (Figure 1-5), which is largely preserved with hydrogenation but not nitrogenation. The V-H system has been summarized by Schober *et al.*[21] There is some minor ambiguity between V-H and V-D structures, and H-site disorder among the few structural studies, but generally, at room temperature V_2H adopts the β structure shown in Figure 1-4, of either *C*1*m*1 symmetry[22] or $I4_1/amd$ symmetry.[23-26] At higher temperatures (> 150 ˚C) during ammonia synthesis, the hydride should become disordered and occupy slightly different sites of the α phase (*Im*-3*m*).[22,27] In all of these structures, despite slight distortions, the V remains in a bcc-type packing arrangement, but for VN, the vanadium atoms must rearrange to fcc packing arrangement.[28] The results suggest that there may be a smooth interconversion between V and V_2H but not to VN, consistent with the

following facts: 1) vanadium can absorb hydrogen and easily form the stable V_2H; 2) basically no VN was detected after ammonia synthesis. In addition, for the V-H(D) system, other $VH(D)_x$ phases with x>0.5 exist, such as α-$VD_{0.8}$ (*Im*-3*m*).[29] The deuterium is mainly distributed over the tetrahedral sites, with a small fraction of the deuterium situated in octahedral sites. The vanadium arrangement is the same with V_2H (bcc structure). Therefore, it is quite conceivable that $VH_{0.44}N_{0.16}$ could also exist, with the small amount of nitride occupying the tetrahedral or octahedral sites, since the V framework can remain essentially unchanged.

Nb and NbH also have bcc-type packing arrangements, with H again occupying tetrahedral sites. ZrH_2 is more subtle, as depending on small stoichiometry differences and temperature,[30] a fluorite structure (δ phase) with close-packed Zr, or more open body-centered tetragonal (bct) type ε phase (*I*4/*mmm*) with hydride can be obtained.[31] Our room temperature XRD measurements show a bct-type ε phase; we have not yet confirmed the structure at 400 ˚C during ammonia synthesis.

On a simplistic level, we may correlate the activities, where metals packed in a looser arrangement (bcc, bct: V_2H, NbH) have high hydrogen permeation, as is well known for hydrogen separation membranes. For more ionic systems such as *Ln*HO (*Ln* = lanthanide), we previously examined the bottleneck in to describe H^- conductivity;[16] a similar analysis (see Experimental) can be done to compare V_2H and TiH_2. Doing so gives respective bottle necks of 1.44 Å (V_2D) and a 1.07 Å (TiH_2); the easier diffusion path in V_2H would be advantageous for Mars van Krevelen mechanisms.

It is often insightful to compare catalysts by their kinetic parameters. The activation energy and reaction orders with respect to N_2, H_2, and NH_3 are plotted in Figure 1-6a−d. The activation energy, obtained over a range of 325−400 °C at 5 MPa for vanadium hydride is 118 kJ/mol, which is comparable to conventional Ru catalysts (85−121 kJ/mol)[8] and higher than previously reported $BaTiO_{2.5}H_{0.5}$ and TiH_2 catalysts (70−80 kJ/mol).[7] These results indicate that vanadium hydride has no obvious promoting effect to lower the energy barrier for ammonia synthesis. Kinetic analyses were carried out at 400 °C and 5 MPa to gain reaction orders on N_2, H_2, and NH_3 (α, β, and γ, respectively). Notably, the N_2 reaction order for $VH_{0.39}$ is quite low, unlike

conventional Ru (or Fe) catalysts (α close to 1). Additionally, $VH_{0.39}$ exhibits a large positive H_2 order, in contrast to conventional Ru catalysts ($\beta < 0$), demonstrating that hydrogen poisoning can be effectively prevented over active catalytic sites.

It is also necessary to consider the relevant M-H and M-N bond strengths, as this is what primarily determines the feasibility of any surface catalytic reaction. The early transition metals in pure metal form generally have M-N bonds which are too strong for ammonia synthesis, thus putting them at the far left of the usual volcano plot.[3] In Figure 1-7, for Ti, V, Zr, and Nb, we compare the heats of formation of the metal nitrides and the calculated heats of N_2 adsorption, based on literature values.[32,33] Both axes have been arranged such that the metals at the top of the plot have strong M-N bonds, implying that metals at the top are the most inactive, and conventionally active metals such as Ru or Fe would lie at the bottom, out of scale. (The heat of formation of Fe_4N is only -12.5 kJ/mol; pure Ru itself does not form nitrides.The initial heat of chemisorption of N_2 on Fe or Ru is 293 kJ/mol (Expt.) and 92-167 kJ/mol (Expt.), respectively.[32]) The effect of hydride for $VH_{0.39}$, TiH_2, and $NbH_{0.6}$, then, is that the active area has been pushed upwards, to include V, Nb, and Ti, but not quite to ZrH_2. As we noted in previous study,[7] the effect of hydride is that it counteracts the negative effects of overly strong M-N bonds. The precise mechanism of this effect is still undetermined, but here we show that this effect is not just limited to titanium, as in our previous report, but also to the other early transition metals such as V and Nb. Wang *et al.* have demonstrated a similar effect for V, Cr, and Mn when the pure metals were mixed with LiH,[5] but here we find single-phase hydrides have the same ability, and note that the bulk structure and diffusion should also be considered.

1.4. Conclusion

In conclusion, the simple hydrides $VH_{0.39}$ and $NbH_{0.6}$ catalyzed ammonia synthesis at 400 °C under 5 MPa, with demonstrated robust catalytic activity for $VH_{0.39}$. The bcc metal lattice, together with the advantageous M-N bond strengths contributes to an improved activity over closely packed fcc TiH_2 or $BaTiO_{2.5}H_{0.5}$. We have not yet been able to separate the effects of changing the metal vs. structure/permeability;

alloying other species to Ti or V to alter the structure without overly changing bond strengths would help in this regard. In general, the precise mechanism of how hydride weakens the M-N bond is still not clear, but it appears to cover a reasonable scope (Ti, V, Nb) enabling further studies and expansion of this field.

References

[1] a) S. L. Foster, S. I. P. Bakovic, R. D. Duda, S. Maheshwari, R. D. Milton, S. D. Minteer, M. J. Janik, J. N. Renner, L. F. Greenlee, *Nat. Catal.* **2018**, *1*, 490–500; b) R. Schlögl, *Angew. Chem. Int. Ed.* **2003**, *42*, 2004–2008.

[2] a) Y. Tang, Y. Kobayashi, N. Masuda, Y. Uchida, H. Okamoto, T. Kageyama, S. Hosokawa, F. Loyer, K. Mitsuhara, K. Yamanaka, Y. Tamenori, C. Tassel, T. Yamamoto, T. Tanaka, H. Kageyama, *Adv. Energy Mater.* **2018**, *8*, 1801772; b) M. Kitano, Y. Inoue, Y. Yamazaki, F. Hayashi, S. Kanbara, S. Matsuishi, T. Yokoyama, S. W. Kim, M. Hara, H. Hosono, *Nat. Chem.* **2012**, *4*, 934–940; c) M. Kitano, Y. Inoue, H. Ishikawa, K. Yamagata, T. Nakao, T. Tada, S. Matsuishi, T. Yokoyama, M. Hara, H. Hosono, *Chem. Sci.* **2016**, *7*, 4036–4043; d) Y. Inoue, M. Kitano, K. Kishida, H. Abe, Y. Niwa, M. Sasase, Y. Fujita, H. Ishikawa, T. Yokoyama, M. Hara, et al., *ACS Catal.* **2016**, *6*, 7577–7584; e) M. Kitano, Y. Inoue, M. Sasase, K. Kishida, Y. Kobayashi, K. Nishiyama, T. Tada, S. Kawamura, T. Yokoyama, M. Hara, H. Hosono, *Angew. Chem. Int. Ed.* **2018**, *57*, 2648–2652; f) W. Gao, P. Wang, J. Guo, F. Chang, T. He, Q. Wang, G. Wu, P. Chen, *ACS Catal.* **2017**, *7*, 3654–3661; g) P. Wang, H. Xie, J. Guo, Z. Zhao, X. Kong, W. Gao, F. Chang, T. He, G. Wu, M. Chen, L. Jiang, P. Chen, *Angew. Chem. Int. Ed.* **2017**, *56*, 8716–8720.

[3] a) C. J. H. Jacobsen, S. Dahl, B. G. S. Clausen, S. Bahn, A. Logadottir, J. K. Nørskov, *J. Am. Chem. Soc.* **2001**, *123*, 8404–8405; b) A. J. Medford, A. Vojvodic, J. S. Hummelshøj, J. Voss, F. Abild-Pedersen, F. Studt, T. Bligaard, A. Nilsson, J. K. Nørskov, *J. Catal.* **2015**, *328*, 36–42; c) A. Vojvodic, A. J. Medford, F. Studt, F. Abild-Pedersen, T. S. Khan, T. Bligaard, J. K. Nørskov, *Chem. Phys. Lett.* **2014**, *598*, 108–112.

[4] a) W. Gao, J. Guo, P. Chen, *Chinese J. Chem.* **2019**, *37*, 442–451; b) F. Rosowski, A. Hornung, O. Hinrichsen, D. Herein, M. Muhler, G. Ertl, *Appl. Catal., A* **1997**, *151*, 443−460; c) N. Saadatjou, A. Jafari, S. Sahebdelfar, *Chem. Eng. Commun*. **2015**, *202*, 420–448; d) J. C. Liu, X. L. Ma, Y. Li, Y. G. Wang, H. Xiao, J. Li, *Nat. Commun.* **2018**, *9*, 1610; e) S. Hagen, R. Barfod, R. Fehrmann, C. J. H. Jacobsen, H. T. Teunissen, I. Chorkendorff, *J. Catal*. **2003**, *214*, 327−335; f) K. Sato, K. Imamura, Y. Kawano, S. Miyahara, T. Yamamoto, S. Matsumura, K. Nagaoka, *Chem. Sci.* **2017**, *8*, 674−679; g) Y. Ogura, K. Sato, S. Miyahara, Y. Kawano, T. Toriyama, T. Yamamoto, S. Matsumura, S. Hosokawa, K. Nagaoka, *Chem. Sci.* **2018**, *9*, 2230−2237; h) M. Nishi, S. Y. Chen, H. Takagi, *ChemCatChem* **2018**, *10*, 3411–3414.

[5] P. Wang, F. Chang, W. Gao, J. Guo, G. Wu, T. He, P. Chen, *Nat. Chem.* **2017**, *9*, 64–70.

[6] F. Chang, Y. Guan, X. Chang, J. Guo, P. Wang, W. Gao, G. Wu, J. Zheng, X. Li, P. Chen, *J. Am. Chem. Soc.* **2018**, *140*, 14799–14806.
[7] Y. Kobayashi, Y. Tang, T. Kageyama, H. Yamashita, N. Masuda, S. Hosokawa, H. Kageyama, *J. Am. Chem. Soc.* **2017**, *139*, 18240–18246.
[8] M. Kitano, J. Kujirai, K. Ogasawara, S. Matsuishi, T. Tada, H. Abe, Y. Niwa, H. Hosono, *J. Am. Chem. Soc.* **2019**, *141*, 20344–20353.
[9] C. Doornkamp, V. Ponec, *J. Mol. Catal. A Chem.* **2000**, *162*, 19–32.
[10] A. Y. Esayed, D. O. Northwood, *Int. J. Hydrogen Energy* **1992**, *17*, 41–52.
[11] S. Morimoto, H. Yukawa, T. Nambu, Y. Murata, *Mater. Trans.* **2016**, *57*, 423–427.
[12] Y. Sekiguchi, K. Arashiba, H. Tanaka, A. Eizawa, K. Nakajima, K. Yoshizawa, Y. Nishibayashi, *Angew. Chem. Int. Ed.* **2018**, *57*, 9064–9068.
[13] J. Huot, D.B. Ravnsbæk, J. Zhang, F. Cuevas, M. Latroche, T.R. Jensen, *Prog. Mater. Sci.* **2013**, *58*, 30–75.
[14] K. Aika, A. Ohya, A. Ozaki, Y. Inoue, I. Yasumori, *J. Catal.* **1985**, 92, 305–311.
[15] Kilner, J. A.; Brook, R. J. A Study of Oxygen Ion Conductivity in Doped Non-Stoichiometric Oxides. *Solid State Ionics 1982*, *6*, 237−252.
[16] H. Ubukata, T. Broux, F. Takeiri, K. Shitara, H. Yamashita, A. Kuwabara, G. Kobayashi, H. Kageyama, *Chem. Mater.* **2019**, *31*, 7360–7366.
[17] O. Hinrichsen, F. Rosowski, A. Hornung, M. Muhler, G. Ertl, *J. Catal.* **1997**, *165*, 33–44.
[18] a) H. Bielawa, O. Hinrichsen, A. Birkner, M. Muhler, *Angew. Chem. Int. Ed.* **2001**, *40*, 1061–1063; b) J. Z. Qiu, J. B. Hu, J. G. Lan, L. F. Wang, G. Y. Fu, R. J. Xiao, B. H. Ge, J. X. Jiang, *Chem. Mater.* **2019**, *31*, 9413–9421.
[19] Y. Tang, Y. Kobayashi, K. Shitara, A. Konishi, A. Kuwabara, T. Nakashima, C. Tassel, T. Yamamoto, H. Kageyama, *Chem. Mater.* **2017**, *29*, 8187–8194.
[20] C. Kemball, *J. Met.* **1952**, *5*, 292–299.
[21] T. Schober, H. Wenzl, *Hydrog. Met II* **1978**, 11–71.
[22] D. G. Westlake, M. H. Mueller, H. W. Knott, *J. Appl. Crystallogr.* **1973**, *6*, 206–216.
[23] H. Asano, M. Hirabayashi, *Phys. Status Solidi* **1973**, *15*, 267–279.
[24] H. Yukawa, D. Yamashita, S. Ito, M. Morinaga, S. Yamaguchi, *Mater. Trans.* **2002**, *43*, 2757–2762.
[25] J. J. Reilly, R. H. Wiswall, *Inorg. Chem.* **1970**, *9*, 1678–1682.
[26] R. L. Zanowick, W. E. Wallace, *J. Chem. Phys.* **1962**, *36*, 2059–2062.
[27] A. J. Maeland, *J. Phys. Chem.* **1964**, *68*, 2197–2200.
[28] F. Kubel, H. D. Flack, K. Yvon, *Phys. Rev. B* **1987**, *36*, 1415–1419.

[29] M.H. Sørby, A. Mellergård, R.G. Delaplane, A. Wannberg, B.C. Hauback, H. Fjellvåg, *J. Alloys Compd.* **2004**, *363*, 209–216.
[30] E. Zuzek, J. R. Abdata, A. San-Martin, F. Manchester, *Bull. Alloy Phase Diagrams* **1990**, *11*, 385–395.
[31] T. Maimaitiyili, A. Steuwer, J. Blomqvist, C. Bjerkén, M. S. Blackmur, O. Zanellato, J. Andrieux, F. Ribeiro, *Cryst. Res. Technol.* **2016**, *51*, 663–670.
[32] K. Aika, K. Tamaru in *Ammonia Catalysis and Manufacture*, (Ed.: A. Nielsen), Springer-Verlag, Berlin, **1995**, pp. 106−108.
[33] M. Eizo, Y. Iwao, *Surf. Sci.* **1976**, *55*, 747–753.

Figures

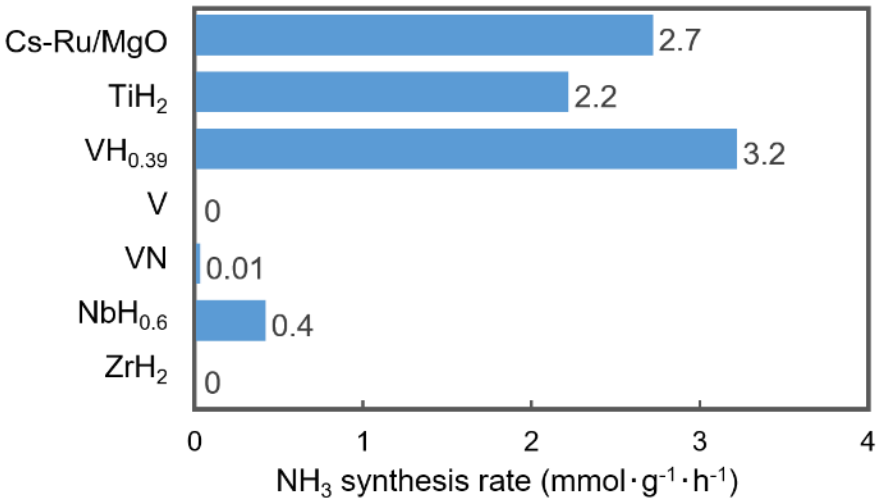

Figure 1-1. Catalytic Activities for NH_3 Synthesis at 400 °C, 5 MPa: (a) Activities comparing various catalysts; (b) Ammonia synthesis rate of $VH_{0.39}$ over 7 days (final TON 130).

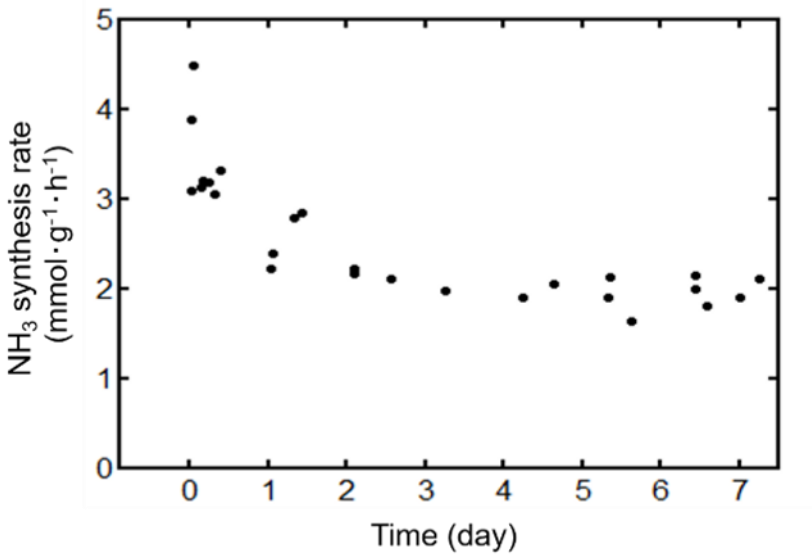

Figure 1-2. Catalytic Activities for NH_3 Synthesis at 400 °C, 5 MPa: (a) Activities comparing various catalysts; (b) Ammonia synthesis rate of $VH_{0.39}$ over 7 days (final TON 130).

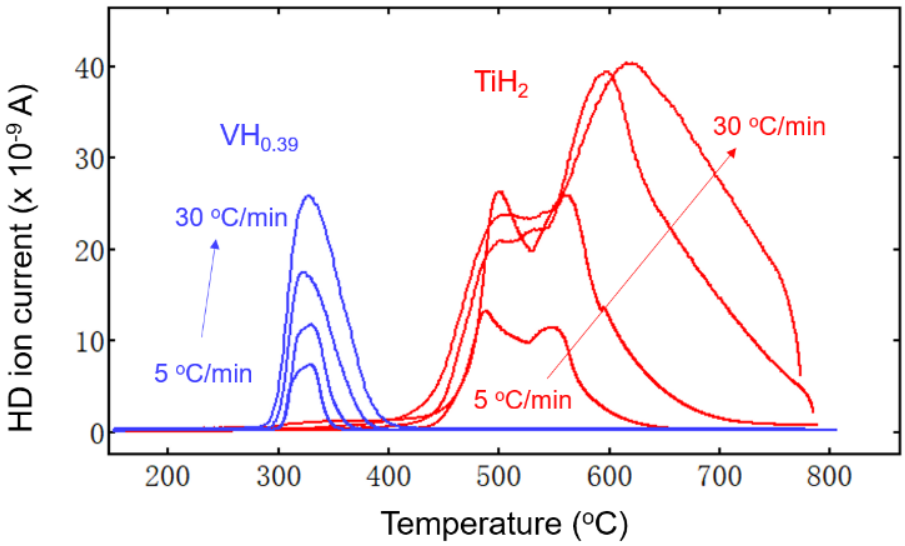

Figure 1-3. H/D Exchange on Vanadium Hydride and Titanium Hydride. Performed under flowing 5% D_2/Ar (5%, 100 mL/min) at heating rates of 5 ˚C/min, 10 ˚C/min, 20 ˚C/min, and 30 ˚C/min.

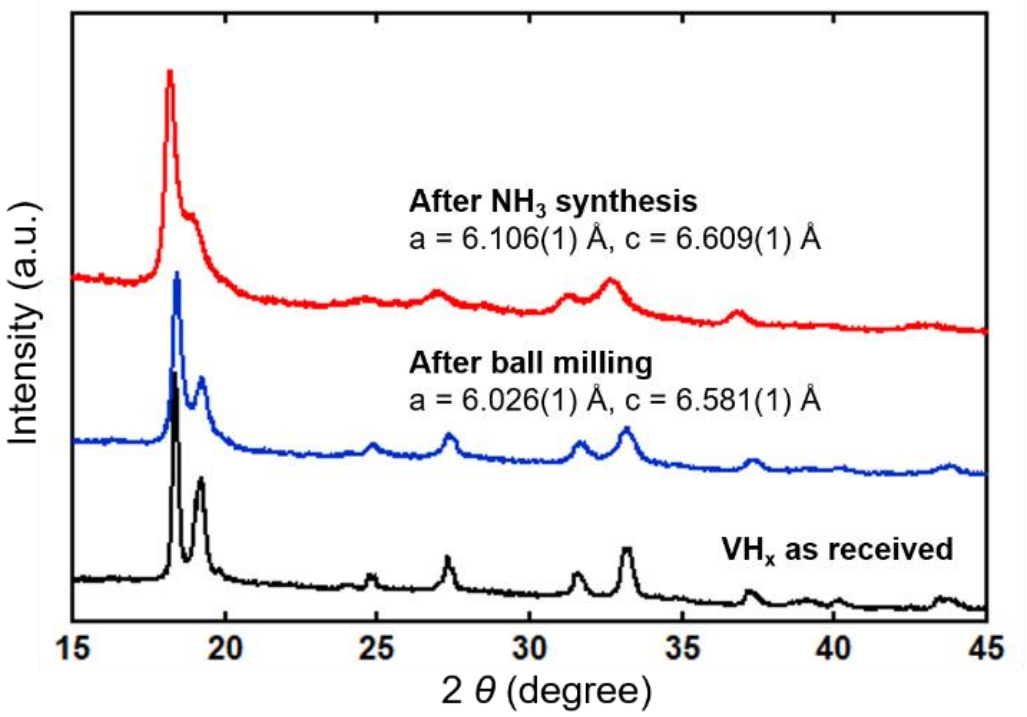

Figure 1-4. Room-Temperature XRD Patterns (Mo K_α radiation) and Lattice Parameters of Vanadium Hydride before and after Ammonia Synthesis (assuming $I4_1/amd$ space group).

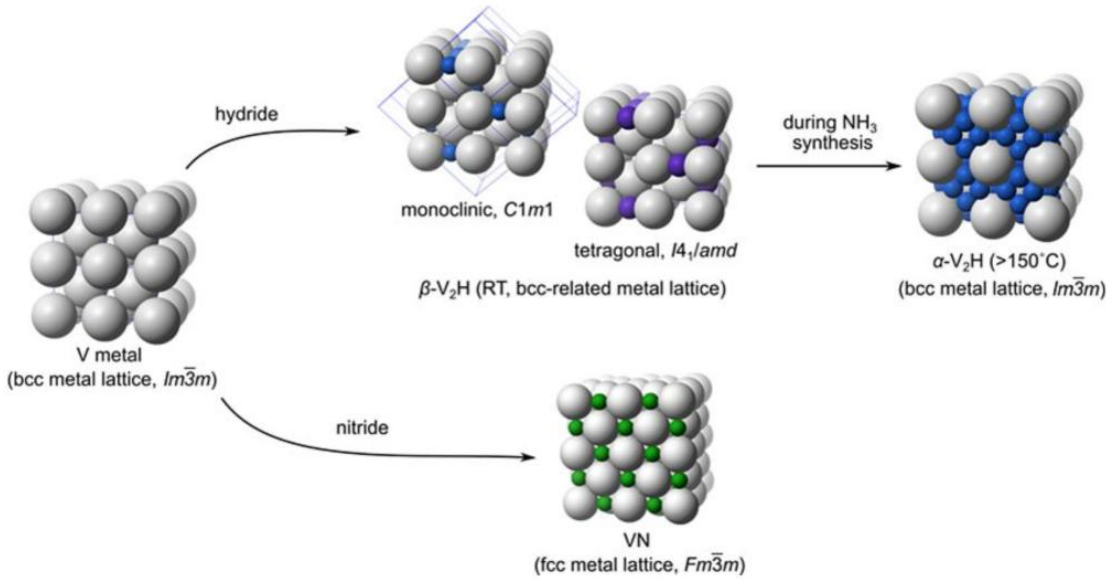

Figure 1-5. The Relationship between the Crystal Structures of V, V_2H, and VN. Although we do not have *in-situ* XRD data for the V_2H catalyst, we expect the α structure during ammonia synthesis (400 ˚C).

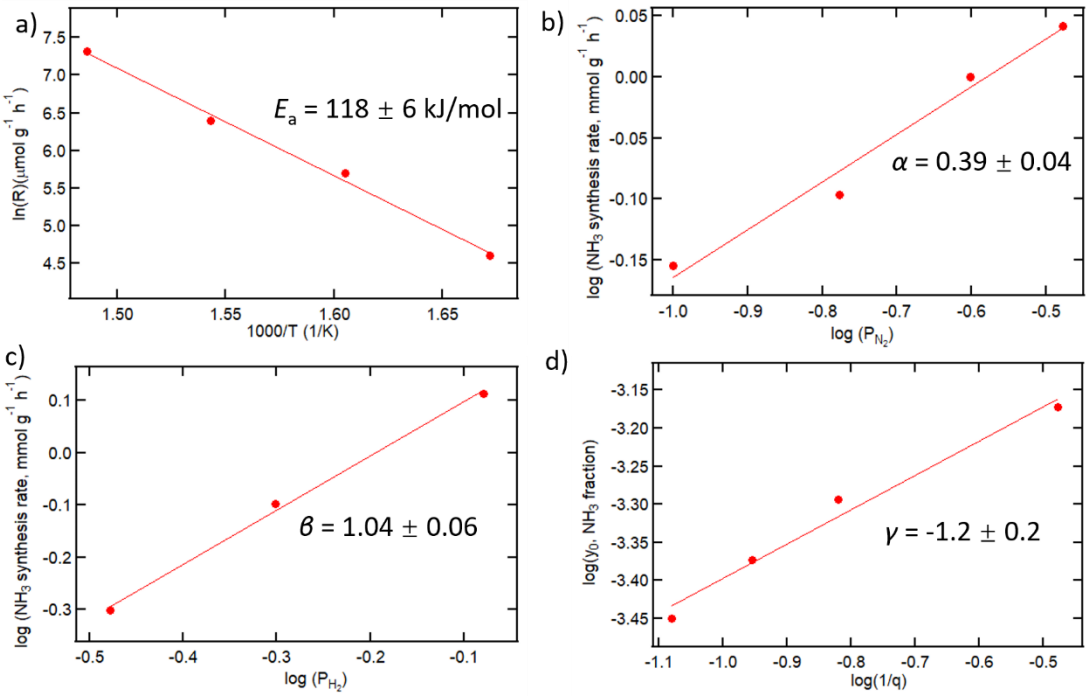

Figure 1-6. (a) Activation energy of NH_3 synthesis at 5 MPa; (b) N_2 reaction order; (c) H_2 reaction order; (d) NH_3 reaction order.

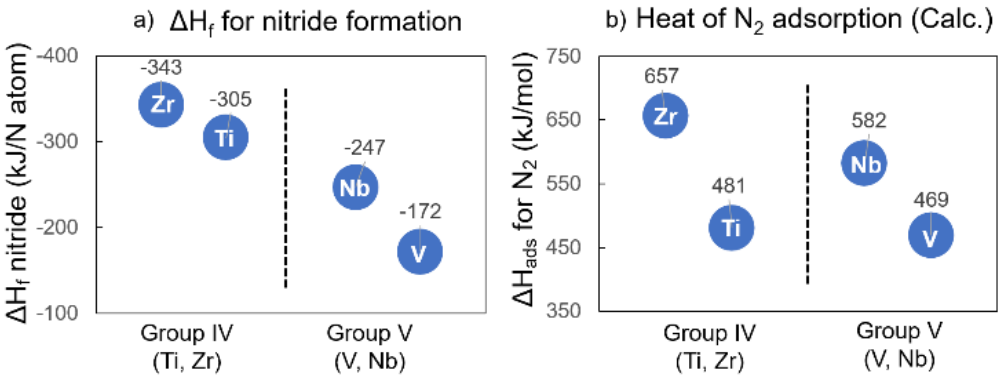

Figure 1-7. (a) Reactivity of the Elements with N_2 and (b) Calculated Heats of Adsorption of N_2.

Chapter 2.

Topochemical Synthesis of Ca_3CrN_3H Involving a Rotational Structural Transformation for Catalytic Ammonia Synthesis

2.1. Introduction

Topochemical reactions of solid oxides have attracted great attention as interesting synthetic pathways to access unusual metastable phases inaccessible by conventional high-temperature solid-state reactions.[1] (De-)intercalation and ion exchange of cations and anions offer convenient ways for the manipulation of chemical composition and structure of host compounds, resulting in changes in physical properties and chemical reactivity.[2] As shown in Figure 2-1, for the topochemical

manipulation of 3-D structures (perovskite, rutile, etc.), this may include substitution or insertion/removal of cations and anions. For 2-D layered compounds, ions can fill (or leave) the interlayer during the layer expansion/shrinkage and may occasionally be accompanied by a lateral shift of layers. [3-4] Some structures with 1-D tunnels such as tungsten bronzes or apatites may also have such exchangeable species.[5] In all of these cases, the host lattice is considered to be generally immobile and rigid, and the overall crystal architecture of the host oxides is maintained.

Compared to the development of topochemical reactions for oxides, examples involving nitrides still remain mostly unreported. To date, only a few successful topochemical cases have been reported to yield several interesting compounds, including the layered nitride $LaReN_2$,[6] oxynitride $EuTiO_2N$,[7] nitride hydride Sr_2NH,[8] nitride halides such as M_2NX (M = Ca, Sr, Ba),[9] and the nitride chalcogenides α-Zr_2N_2S, α-Hf_2N_2S.[10-11] Most topochemical reactions have their products/starting materials in the same or related symmetry. Here, we found a topochemical hydrogen intercalation involving a rotational structural transformation from orthorhombic Ca_3CrN_3 (*o*-Ca_3CrN_3) to hexagonal antiperovskite Ca_3CrN_3H (*h*-Ca_3CrN_3H). Under N_2/H_2/Ar flow, *h*-Ca_3CrN_3H exhibits continuous ammonia production, indicating catalytic activity despite the lack of Ru/Fe.

2.2. Experimental

Material synthesis and characterization. CrN was prepared by heating Cr_2O_3 powder (1.0 g) under a flow of ammonia gas to 1073 K for 12 hours. The resulting powder was reground and heated under the same conditions for an additional 12 hours. The formation of CrN was confirmed by XRD. Ca_3CrN_3 was prepared by heating a mixture of CrN (4.55 mmol), Ca_3N_2 (4.55 mmol, 99%, Sigma-Aldrich) and CaH_2 (2.29 mmol, 97%, Sigma-Aldrich) in a sealed stainless-steel tube under N_2 atmosphere at 1273 K for 4 days. Gas-solid reaction is adopted to inject hydride anions into Ca_3CrN_3 to obtain Ca_3CrN_3H using pure H_2 gas (>99.99999%) or N_2/H_2/Ar mixed gas (22.5: 67.5: 10). We characterized the purity and crystal structures of the samples by SPXRD, which was conducted at room temperature on a Debye-Scherrer camera at

SPring-8 BL02B2 of the Japan Synchrotron Radiation Research Institute (JASRI) (λ = 0.419471(1) Å). Powder samples were loaded into Pyrex capillaries with an i.d. of 0.3 mm. VESTA was used to plot the crystal structures.[12]

Thermogravimetric and mass spectrometric (TG-MS) analysis. TG experiments were conducted with a Bruker AXS TG-DTA 2000S by heating sample (ca. 20 mg, 10 K min^{-1}) in a stream of pure Ar (>99.9999%) gas up to 1073 K. The hydrogen release upon heating was monitored under flowing Ar at 200 mL/min by a Bruker MS9610 quadrupole mass spectrometer connected to the TG instrument.

Transmission electron microscopy (TEM). The sample for TEM investigation was prepared in an Ar-filled glove box (MBraun) by crushing the powder in a mortar in dimethyl carbonate and depositing drops of suspension onto holey copper grid with supporting carbon layer. The sample was transported to the TEM column being locked inside the hermetic vacuum transfer holder, thus completely avoiding the contact with air and moisture. High angle annular dark field scanning transmission electron microscopy (HAADF-STEM) images and energy-dispersive X-ray (EDX) spectra were taken with an aberration-corrected Titan Themis Z transmission electron microscope operated at 200 kV. Integrated differential phase contrast (iDPC) maps were registered in a STEM-mode at low electron dose (~10 pA) using a 4-quadrant segmented detector. iDPC-STEM maps were transformed into corresponding projected charge density maps (dDPC-STEM maps). Electron diffraction tomography (EDT) series were collected manually by rotating the selected crystal with a constant angular step of 1° over 90° and registering the corresponding reciprocal lattice sections on a 4K×4K BM-Ceta CMOS detector. The PETS and JANA2006 software were used for the treatment of the EDT patterns and the reconstruction of 3D reciprocal space.[13] Rietveld profile refinements were performed using JANA2006[13] and the GSAS suite of programs [14].

Solid-state NMR Spectroscopy. ^{1}H MAS solid state NMR spectra were recorded on Bruker AVANCE III spectrometer operating at 400 MHz with a conventional double-resonance 3.2 mm CP-MAS probe. The samples were packed into zirconium rotors under an inert atmosphere inside glovebox and dry nitrogen gas was utilized for sample spinning to prevent degradation of the samples. The spinning

frequency was set to 10 and 12 kHz. NMR chemical shifts are reported with respect to tetramethylsilane (TMS) as external reference.

***In situ* SPXRD with controlling gas.** The topochemical conversion from *o*-Ca_3CrN_3 to *h*-Ca_3CrN_3H was investigated by SPXRD at the BL02B2 beamline in SPring-8.[15] Ca_3CrN_3 powder was sealed in a 0.5 mm diameter quartz glass capillary. It was connected to a stainless-steel gas cell which can introduce gas into the capillary tube. The sample was evacuated first and raise temperature to 713 K, and then H_2 gas pressures up to 101 kPa. The SPXRD patterns were measured *in situ* under ambient H_2 gas pressure at 713 K. The incident X-ray wavelength was 0.419471(1) Å.

Ammonia synthesis. 0.1 g Ca_3CrN_3 sample was suspended in a 3/8" stainless steel tube on a bed of quartz wool. Catalyst sample was initially treated with flowing H_2 (0.1 MPa, 90 mL/min) at 723 K for 2 hours. Catalytic runs were then conducted at 5 MPa (gauge pressure), with a flow rate of 110 mL/min. Unless otherwise noted, the synthesis gas composition was N_2: H_2: Ar = 22.5: 67.5: 10, where Ar was initially intended to serve as an internal standard for calibrating a mass spectrometer. Commercially supplied gases with O_2 < 2 ppm and H_2O < 5 ppm were purified with an in-line H_2O/O_2 filter to achieve ppt-level purity. Ammonia formation was quantified by an aqueous trap (1.87×10^{-5} M NH_4Cl, 333 mL) and an ammonia-selective electrode (Horiba X 5002A).

DFT calculations. We performed first-principles calculations using the Perdew-Burke-Ernzerhof parametrization of the generalized gradient approximation[16] and the projected augmented wave (PAW) method[17] as implemented in the *Vienna Ab initio Simulation Package.*[18-21] The core states in the PAW potentials are as follows: [Ne] for Ca and Cr, [Ar]3d^{10} for Sr, [Kr]4d^{10} for Ba, and [He] for O. The Hubbard U correction[22] with the simplified rotationally invariant approach[23] was included. We used $U - J = 3$ eV for the Cr-*d* orbitals. For the *Cmcm* structure, we assumed the G-type antiferromagnetic state to represent the localized spin moments. For the $P6_3/m$ structure, we assumed the non-magnetic state. The plane-wave cutoff energy of 550 eV and the Gaussian smearing width of 0.1 eV were used. The structural optimization was continued until the Hellmann–Feynman force on each atom becomes less than 0.01 eV

$Å^{-1}$. Spin-orbit coupling was not included throughout this paper. The charge density is depicted using the VESTA software.[12]

2.3. Results and discussions

The crystal structure of the initial *o*-Ca_3CrN_3 (Figure 2-2), which is a known compound reported by DiSalvo et al.,[24] consists of 1-D Ca-N strips (blue cubes). Each of these strips consists of 2×1 rock salt-type cubes extending along the *c* axis, which are connected by trigonal-planar $[CrN_3]^{6-}$ units confined within the *ab* plane. Analysis of the synchrotron powder X-ray diffraction (SPXRD) data collected from as-prepared *o*-Ca_3CrN_3 is consistent with the reported *Cmcm* orthorhombic structure. Treating *o*-Ca_3CrN_3 in pure H_2 gas (673 K, 0.1 MPa) resulted in a drastic change in the X-ray diffraction profile (Figure 2-3a), implying that a new phase was formed. When a thermogravimetric/mass spectrometric (TG-MS) analysis of the hydrogenated sample was conducted under Ar gas flow, H_2 release was observed at around 600 K (Figure 2-3b), thus proving the presence of hydrogen in this compound and suggesting that a nitride-hydride may have been generated.

In order to solve the structure, the reciprocal space lattice of the hydrogen-treated sample was scanned by electron diffraction tomography (EDT). The nodes of 3-D difference vector space reconstructed from EDT can be indexed with the unit cell parameters $a \sim 7.23$ Å, $c \sim 5.06$ Å, $\gamma \sim 120°$, indicating hexagonal symmetry. The reconstructed [100] and [001] reciprocal lattice sections are shown in Figure 2-4. As the 00*l*: $l = 2n$ reflection condition is clearly observed in the [100] reciprocal lattice section and no special conditions are present for other groups of reflections, only three space groups are possible ($P6_3$, $P6_3/m$, $P6_322$). Among them, the centrosymmetric $P6_3/m$ space group was chosen for further treatment. EDT intensities were integrated and the structure solution was performed in a quasi-kinematical approximation with a charge flipping algorithm[25] using Superflip[26] resulting in 1 Cr and 1 Ca position. The position of N atoms was assigned by a Fourier difference map from SPXRD data (Figure 2-5). After subsequent Rietveld refinement and further analysis of Fourier difference maps, the H atoms were also localized (Figure 2-5).

The SPXRD profile can be reliably fitted with the hexagonal unit cell $P6_3/m$ with all peak intensities accounted for, as shown in Figure 2-6. The impurity CaO were also included to the Rietveld refinement, yielding the mass fractions of 4.4%. The atomic coordinates and ADPs are given in the inserted Table. Energy-dispersive X-ray (EDX) of individual particles examined for EDT showed the expected Ca:Cr = 3.02(1):0.98(1) atomic ratio (Figure 2-7). The Ca_3CrN_3H formula derived from the Rietveld refinement is in good agreement with the Ca:Cr atomic ratio calculated from the EDX analysis. The crystal structure of *h*-Ca_3CrN_3H (deposition number: 2172145)[27] is shown in Figure 2-8, where face-sharing Ca_6 octahedra are arranged in chains along the *c* axis, and each hydrogen atom is positioned in the center of the octahedron. It can be described as a hexagonal antiperovskite structure (X_3BA, $BaNiO_3$-type) where the H anions sit in the B sites octahedrally coordinated by six Ca cations, and the $[CrN_3]^{6-}$ units serve as the A site species.

The crystal structure of *h*-Ca_3CrN_3H solved from SXRD+EDT data corroborates well with the experimental [100] high angle annular dark field scanning transmission electron microscopy (HAADF-STEM) images (Figure 2-9) and differential phase contrast (DPC) maps (Figure 2-10). In the [100] HAADF-STEM image, the brightest spots correspond to heavier atomic columns, composed of Cr, Ca and N, while less intense spots are related to pure Ca columns. The [100] DPC-STEM map clearly illustrates two individual Ca columns and location of N atoms.

For the determination of nitrogen and hydride content in *h*-Ca_3CrN_3H, we confirmed that the hydrogenation reaction does not alter the nitrogen content through Rietveld refinement of SPXRD data for nitrogen occupancy (1.04(1)). Solid state ^1H magic angle spinning NMR exhibits a single peak at +5.2 ppm (Figure 2-11), which is consistent with that reported for other ionic hydrides.[28] We have also roughly estimated the hydride content based on TG-MS under Ar atmosphere (Table 2-1). Here, $VH_{0.39}$ (99%, Kojundo Chemical Lab. Co., Ltd., 150 μm; hydride content determined by combustion elemental analysis) was used to prepare a calibration curve. Different amounts of $VH_{0.39}$ were heated in Ar flow up to 1073 K. The peak area of H_2 release was integrated, yielding a calibration curve with good linearity $R^2 = 0.9995$. *h*-$Ca_3CrN_3H_x$ was heated under the same conditions as $VH_{0.39}$. The hydride content of *h*-

$Ca_3CrN_3H_x$ was then estimated by calibration curve to be ca. 0.70. Looking at the H_2 release peak in Figure 2-3b, it is quite likely that not all of the hydrogen is released at 1073 K (the maximum operation temperature of the TG furnace, instrumental limitation) and thus not quantified. Further quantitative efforts may be necessary to unambiguously characterize the hydrogen content. However, if the U_{iso} of H is fixed to be 0.01, refining the H occupancy leads to a reasonable value 0.85. Neutron diffraction can be used in the future to accurately refine the H occupancy. Although ambiguity exists in the exact hydrogen content, in what follows, let us use the stoichiometric composition (i.e., *h*-Ca_3CrN_3H).

Hydrogenation of *o*-Ca_3CrN_3 to yield *h*-Ca_3CrN_3H should result in oxidation from Cr^{3+} to Cr^{4+}. To examine this, bond valence sum (BVS) calculations of *h*-Ca_3CrN_3H have been performed using the parameters derived by Brese and O'Keeffe,[29-30] where R_{ij} for Cr-N was set to 1.85 Å. The BVS calculations yielded 1.84 for Ca and 4.24 for Cr in *h*-Ca_3CrN_3H. This contrasts to before hydrogenation (i.e. of *o*-Ca_3CrN_3) where the BVS for Cr is 3.47.[31]

It is interesting to compare *o*-Ca_3CrN_3 and *h*-Ca_3CrN_3H with the known A_3MN_3 compounds (*A* is typically alkaline earth metal Ca, Sr or Ba, and *M* is transition metal V, Cr, Mn or Fe). These can be divided into two different structure types: orthorhombic structures for Ca_3MN_3 (red in Figure 2-12), and hexagonal structures for Sr_3MN_3 and Ba_3MN_3 (blue in Figure 2-12).[31-32] We have calculated the total energy difference of orthorhombic (*Cmcm*) and hexagonal ($P6_3/m$) A_3CrN_3 (*A* = Ca, Sr, Ba) using density functional theory (DFT) (Table 2-2). For Sr_3CrN_3 and Ba_3CrN_3, the $P6_3/m$ structure is stable, while for Ca_3CrN_3, the *Cmcm* structure is stable. In our case, the hydrogenation of orthorhombic Ca_3CrN_3 resulted in the new hydride Ca_3CrN_3H, which is isostructural to hexagonal Sr_3MN_3 and Ba_3MN_3 (apart from H), thus linking these two different structure groups together. Many of the hexagonal A_3MN_3 compounds have already been suspected or demonstrated to be electride or hydride compositions, such as $(Sr^{2+})_3(Cr^{4+})(N^{3-})_3{:}e^-$[33] and Ba_3CrN_3H[34]. We suspect that our *h*-Ca_3CrN_3H can also be a hydride-electride as we show later.

It is possible to sketch out a transition from orthorhombic A_3MN_3 to hexagonal A_3MN_3H structure. As shown in Figure 2-13, when viewed along the [100]

direction, the 1-D Ca-N rock salt-like chains convert to face-sharing octahedral chains upon hydride insertion. Viewed along the [001] direction, the transformation of the structure causes the change of rotational symmetry. The transition calls to mind a hinged tessellation, where a combination of rigid units and flexible joints gives rotational structural changes. Here, the rigid unit is a pair of $[CrN_3]^{6-}$ triangles (blue dashed lines). The Ca-N units (red solid lines) behave as flexible parts which will change shape with rotation of the rigid units. These flexible rectangles are the 2×1 cubes, which contain 3 Ca atoms on top, and 3 Ca atoms immediately underneath, but they open up into the Ca_6, which requires 3 co-planar Ca atoms above and below.

The modification of rock salt motifs has been reported previously, but not in the same way. For instance, in the reaction of Ruddlesden–Popper phases Sr_2TiO_4[35] and $Sr_3Ru_2O_7$[36] to produce $Sr_2TiO_3F_2$ and $Sr_3Ru_2O_7F_2$, respectively, fluoride ions are inserted into the tetrahedral sites within the Sr-O rock salt layers between perovskite blocks, associated with a rock salt layer expansion. However, there is no rotational movement and the overall structure retains its 4-fold symmetry along the *c*-axis. In metal–organic frameworks (MOFs), some aspects of local rotation can be seen in structural transformations involving breathing. [37-39] For *Ln*Fe(CN)$_6$, structural distortions occur under high pressure, involving bending of cyanide ions linkers, leading to the twisting of *Ln*N_6 units.[40] A striking aspect of our system is the observation of structural flexibility in a relatively closely-packed inorganic material, as opposed to a coordination framework.

In order to examine the structural transformation from *o*-Ca_3CrN_3 to *h*-Ca_3CrN_3H, *in situ* XRD patterns were obtained. *o*-Ca_3CrN_3 was stable under N_2 up to 1073 K, indicating that N_2 cannot trigger the structural change of *o*-Ca_3CrN_3. In contrast, as shown in Figure 2-14, under H_2 (at 713 K), the peaks of *o*-Ca_3CrN_3 disappeared over time, while peaks assigned to *h*-Ca_3CrN_3H concomitantly emerged. No new peak from intermediate phases or peak broadening were observed, and the product *h*-Ca_3CrN_3H peaks are only slightly broader than the parent *o*-Ca_3CrN_3 peaks. The change in phase fraction can be analyzed by the Avrami-Erofe'ev equation,[41-42] (Figure 2-15), giving an Avrami exponent $n = 1.39$. This implies that the transformation

proceeds by 1-D, 2-D diffusion-controlled and/or 1-D interface-controlled growth process.[43]

We have also found that *h*-Ca_3CrN_3H (a = 7.2665(1) Å, c = 5.1139(1) Å, c/a = 0.7038, at 703 K) can be dehydrogenated to *h*-Ca_3CrN_3 while retaining the hexagonal structure upon further heating to 1073 K under vacuum and then cooling down to 703 K. As shown in Figure 2-16, XRD shows peak shifts due to different lattice parameters (and c/a ratios) for the hydride and dehydrogenated samples. The structure of *h*-Ca_3CrN_3 stays hexagonal, but with slightly different lattice parameters (a = 7.2967(1) Å, c = 5.0608(1) Å, c/a = 0.6936, at 703 K). *h*-Ca_3CrN_3 will not transform back to the orthorhombic phase upon cooling to room temperature, indicating the robustness of the metastable *h*-Ca_3CrN_3 phase (Figure 2-17). The observation of a decrease of c/a ratio as hydrogen content decreases is consistent with the reported Sr_3CrN_3 analogue.[33] The BVS calculations of *h*-Ca_3CrN_3 yield 1.52 for Ca and 4.03 for Cr, indicating that *h*-Ca_3CrN_3 is 1-D electride. When purging with H_2 again at 703 K, *h*-Ca_3CrN_3 converts back to *h*-Ca_3CrN_3H (a = 7.2647(1) Å, c = 5.1130(1) Å, c/a = 0.7038), making the process reversible (Figure 2-16).

The electronic structures of *h*-Ca_3CrN_3H and *h*-Ca_3CrN_3 were examined by DFT calculations. While *h*-Ca_3CrN_3H is an insulator (the band structure and the partial density of states are shown in Figure 2-18), *h*-Ca_3CrN_3 is metallic. Figure 2-19 shows the interstitial electrons weight on the band structure for *h*-Ca_3CrN_3. The yellow line, i.e. band with mostly interstitial electron character, possesses a parabolic behavior along the Γ-A direction, indicating that the electrons are stabilized in the 1-D Ca_6 octahedra channel. This is shown in the partial charge density map in Figure 2-19b.

Notably, recently various 3*d* transition metal nitrides, hydrides and electrides have been reported to be ammonia synthesis catalysts, such as LiH-TM(N),[44] [Ba-Cr-N-H],[45] TiH_2,[46] $BaTiO_{2.5}H_{0.5}$,[46] $VH_{0.39}$,[47] and LaCoSi,[48] despite the absence of Ru or Fe. This has provoked our interest to look into the catalytic performance of *h*-Ca_3CrN_3H. Interestingly, we found it exhibited continuous ammonia production (~ 3800 $\mu mol \cdot g^{-1} \cdot h^{-1}$ at 5 MPa and 673 K) over 120 hrs without degradation in activity (Figure 2-20). The activity of *h*-Ca_3CrN_3H is better than that of some other non-Ru/Fe

catalysts, such as TiH_2 (2800 μmol·g^{-1}·h^{-1}),[46] $BaTiO_{2.5}H_{0.5}$ (1400 μmol·g^{-1}·h^{-1}),[46] and $VH_{0.39}$ (3200 μmol·g^{-1}·h^{-1})[47] at 5 MPa and 673 K.

2.4. Conclusion

In summary, we have shown the topochemical synthesis of *h*-Ca_3CrN_3H from *o*-Ca_3CrN_3. In contrast to conventional topochemical reactions in which the host structures are maintained, we found that the intercalation of the hydride modifies the Ca-N rock salt packing in *o*-Ca_3CrN_3 to a face-shared octahedra chain in *h*-Ca_3CrN_3H involving a rotational structural transformation. The *h*-Ca_3CrN_3H also exhibited catalytic performance for ammonia synthesis. We believe that the topochemical synthesis of *h*-Ca_3CrN_3H and the following catalytic application encourage the expansion and exploration of a large group of A_3MN_3H hexagonal antiperovskite nitride-hydride materials and even other structural types as promising ammonia synthesis catalysts.

References

[1] H. Kageyama, K. Hayashi, K. Maeda, J. P. Attfield, Z. Hiroi, J. M. Rondinelli, K. R. Poeppelmeier, *Nat. Commun.* **2018**, *9*, 772-787.

[2] K. G. Sanjaya Ranmohotti, E. Josepha, J. Choi, J. Zhang, J. B. Wiley, *Adv. Mater.* **2011**, *23*, 442–460.

[3] M. A. Hayward, *Semicond. Sci. Technol.* **2014**, *29*, 064010.

[4] R. Uppuluri, A. Sen Gupta, A. S. Rosas, T. E. Mallouk, *Chem. Soc. Rev.* **2018**, *47*, 2401–2430.

[5] K. Sudarsanan, P. E. Mackie, R. A. Young, *Mater. Res. Bull.* **1972**, *7*, 1331–1337.

[6] S. D. Kloß, M. L. Weidemann, J. P. Attfield, *Angew. Chemie - Int. Ed.* **2021**, *60*, 22260–22264.

[7] R. Mikita, T. Aharen, T. Yamamoto, F. Takeiri, T. Ya, W. Yoshimune, K. Fujita, S. Yoshida, K. Tanaka, D. Batuk, A. M. Abakumov, C. M. Brown, Y. Kobayashi, H. Kageyama, *J. Am. Chem. Soc.* **2016**, *138*, 3211–3217.

[8] R. Chemnitzer, G. Auffermann, D. M. Többens, R. Kniep, *Zeitschrift fur Anorg. und Allg. Chemie* **2005**, *631*, 1813–1817.

[9] O. Reckeweg, F. J. DiSalvo, *Solid State Sci.* **2002**, *4*, 575–584.

[10] C. Stoltz, K. Ramesha, S. A. Sirchio, Z. S. Gönen, B. W. Eichhorn, L. Salamanca-Riba, J. Gopalakrishnan, *J. Am. Chem. Soc.* **2003**, *125*, 4285–4292.

[11] S. Zhang, M. Yoshikawa, K. Inumaru, S. Yamanaka, *Inorg. Chem.* **2013**, *52*, 10571–10575.

[12] K. Momma, F. Izumi, *J. Appl. Crystallogr.* **2011**, *44*, 1272–1276.

[13] V. Petříček, M. Dušek, L. Palatinus, *Zeitschrift für Krist. - Cryst. Mater.* **2014**, *229*, 345–352.

[14] A.C. Larson, R.B. Von Dreele, Los Alamos National Laboratory Report LAUR 86-748, **2000**.

[15] S. Kawaguchi, M. Takemoto, H. Tanak, S. Hiraide, K. Sugimoto, Y. Kubota, *J. Synchrotron Radiat.* **2020**, *27*, 616–624.

[16] J. P. Perdew, K. Burke, M. Ernzerhof, *Phys. Rev. Lett.* **1996**, *77*, 3865–3868.

[17] D. Joubert, *Phys. Rev. B - Condens. Matter Mater. Phys.* **1999**, *59*, 1758–1775.

[18] G. Kresse, J. Hafner, *Phys. Rev. B* **1993**, *47*, 558–561.

[19] G. Kresse, J. Hafner, *Phys. Rev. B* **1994**, *49*, 14251–14269.

[20] G. Kresse, J. Furthmüller, *Comput. Mater. Sci.* **1996**, *6*, 15–50.

[21] G. Kresse, J. Furthmüller, *Phys. Rev. B* **1996**, *54*, 11169–11186.

[22] A. I. Lichtenstein, V. I. Anisimov, J. Zaanen, *Phys. Rev. B* **1995**, *52*, 5467–5471.

[23] S. Dudarev, G. Botton, *Phys. Rev. B - Condens. Matter Mater. Phys.* **1998**, *57*, 1505–1509.
[24] D. A. Vennos, M. E. Badding, F. J. DiSalvo, *Inorg. Chem.* **1990**, *29*, 4059–4062.
[25] G. Oszlányi, A. Sütő, *Acta Cryst.* **2004**, *A60*, 134–141.
[26] L. Palatinus, *Acta Cryst.* **2004**, *A60*, 604–610.
[27] Deposition Number 2172145 contains the supplementary crystallographic data for this paper. These data are provided free of charge by the joint Cambridge Crystallographic Data Centre and Fachinformationszentrum Karlsruhe Access Structures service www.ccdc.cam.ac.uk/structures.
[28] K. Hayashi, P. V. Sushko, Y. Hashimoto, A. L. Shluger, H. Hosono, *Nat. Commun.* **2014**, *5*, 3515.
[29] N. E. Brese, M. O'Keeffe, *Acta Crystallogr. Sect. B* **1991**, *47*, 192–197.
[30] M. O'Keeffe, N. E. Brese, *J. Am. Chem. Soc.* **1991**, *2*, 3226–3229.
[31] M. G. Barker, M. J. Begley, P. P. Edwards, D. H. Gregory, S. E. Smith, *J. Chem. Soc. - Dalt. Trans.* **1996**, 1–5.
[32] R. B. King, *Can. J. Chem.* **1995**, *73*, 963–971.
[33] P. Chanhom, K. E. Fritz, L. A. Burton, J. Kloppenburg, Y. Filinchuk, A. Senyshyn, M. Wang, Z. Feng, N. Insin, J. Suntivich, G. Hautier, *J. Am. Chem. Soc.* **2019**, *141*, 10595–10598.
[34] N. W. Falb, J. N. Neu, T. Besara, J. B. Whalen, D. J. Singh, T. Siegrist, *Inorg. Chem.* **2019**, *58*, 3302–3307.
[35] P. R. Slater, R. K. B. Gover, *J. Mater. Chem.* **2002**, *12*, 291–294.
[36] R. Li, C. Greaves, *Phys. Rev. B - Condens. Matter Mater. Phys.* **2000**, *62*, 3811–3815.
[37] A. Schneemann, V. Bon, I. Schwedler, I. Senkovska, S. Kaskel, R. A. Fischer, *Chem. Soc. Rev.* **2014**, *43*, 6062–6096.
[38] G. Férey, *Dalt. Trans.* **2016**, *45*, 4073–4089.
[39] G. Férey, C. Serre, *Chem. Soc. Rev.* **2009**, *38*, 1380–1399.
[40] S. G. Duyker, V. K. Peterson, G. J. Kearley, A. J. Studer, C. J. Kepert, *Nat. Chem.* **2016**, *8*, 270–275.
[41] H. Liu, R. M. Sullivan, J. C. Hanson, C. P. Grey, J. D. Martin, *J. Am. Chem. Soc.* **2001**, *123*, 7564–7573.
[42] Y. Pang, Q. Li, *Scr. Mater.* **2017**, *130*, 223–228.
[43] S. R. Kinetics, *Compr. Chem. Kinet.* **1980**, *22*, 41–113.
[44] P. Wang, F. Chang, W. Gao, J. Guo, G. Wu, T. He, P. Chen, *Nat. Chem.* **2017**, *9*, 64–70.

[45] Y. Guan, W. Zhang, Q. Wang, C. Weidenthaler, A. Wu, W. Gao, Q. Pei, H. Yan, J. Cui, H. Wu, S. Feng, R. Wang, H. Cao, X. Ju, L. Liu, T. He, J. Guo, P. Chen, *Chem Catal.* **2021**, *1*, 1042–1054.
[46] Y. Kobayashi, Y. Tang, T. Kageyama, H. Yamashita, N. Masuda, S. Hosokawa, H. Kageyama, *J. Am. Chem. Soc.* **2017**, *139*, 18240–18246.
[47] Y. Cao, A. Saito, Y. Kobayashi, H. Ubukata, Y. Tang, H. Kageyama, *ChemCatChem* **2021**, *13*, 191–195.
[48] Y. Gong, J. Wu, M. Kitano, J. Wang, T. Ye, J. Li, Y. Kobayashi, K. Kishida, H. Abe, Y. Niwa, H. Yang, T. Tada, H. Hosono, *Nat. Catal.* **2018**, *1*, 178–185.

Figures

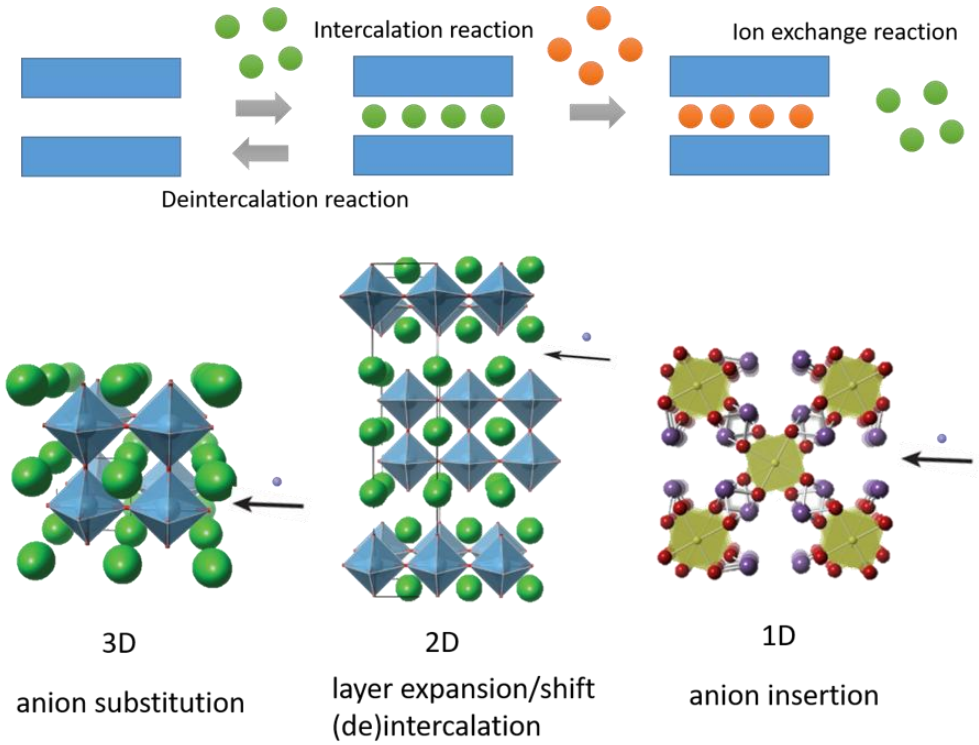

Figure 2-1. Topochemical manipulations include (de)intercalation reaction and ion exchange reactions of 3D closed-packed compounds, 2D layered compounds and 1D chain compounds.

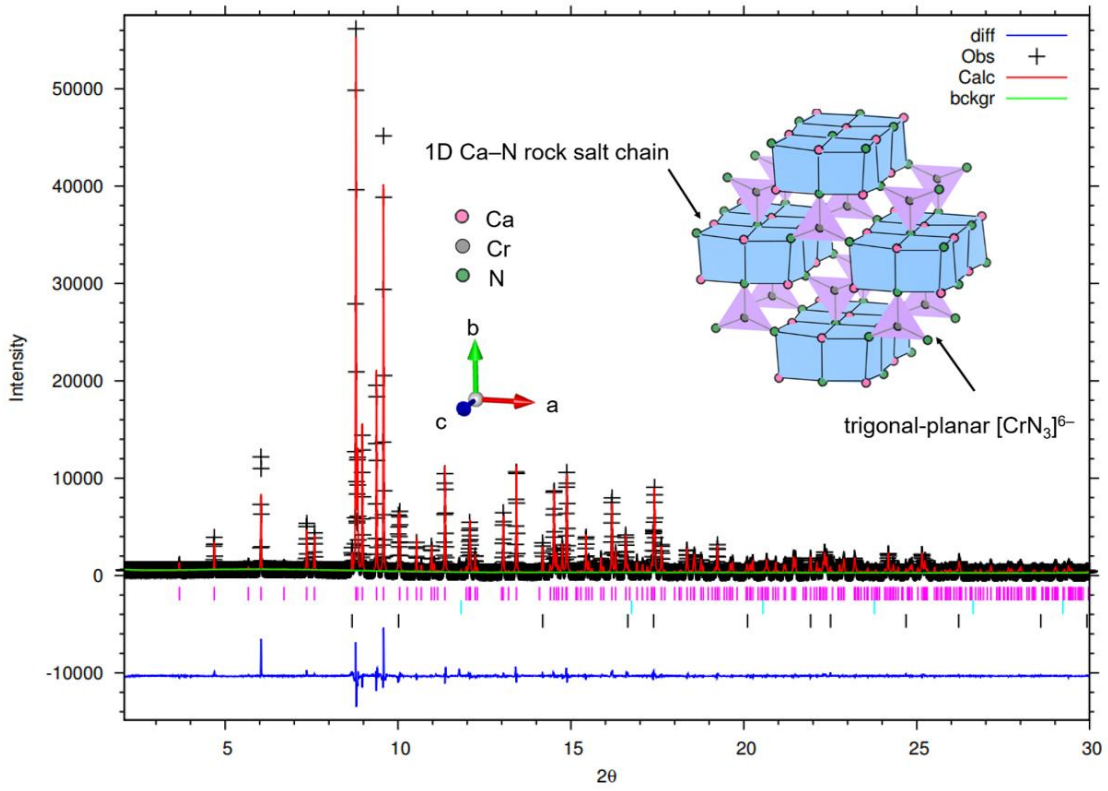

Figure 2-2. Rietveld refinement of *o*-Ca_3CrN_3, *Cmcm* orthorhombic structure, a = 8.4908(1) Å, b = 10.2766(1) Å, c = 5.0293(1) Å, with CaO (4.8%) impurities. Inset: structure of *o*-Ca_3CrN_3. Pink, gray and green spheres represent Ca, Cr and N.

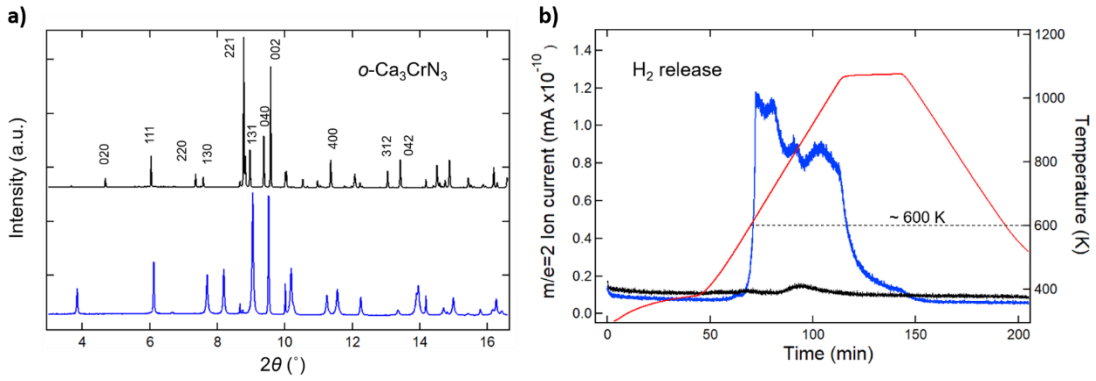

Figure 2-3. a) SPXRD patterns of *o*-Ca_3CrN_3 before (black) and after (blue) H_2 treatment (673 K, 0.1 MPa, 12 h). b) TG-MS curves. H_2 release measurements of *o*-Ca_3CrN_3 (black) and sample after hydrogenation (blue).

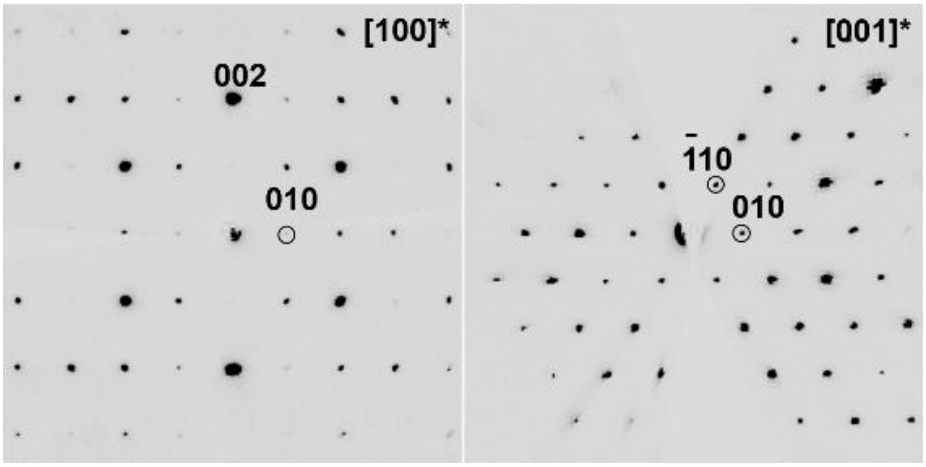

Figure 2-4. Reciprocal lattice sections from EDT data indexed with hexagonal unit cell with a ~ 7.23 Å and c ~ 5.06 Å.

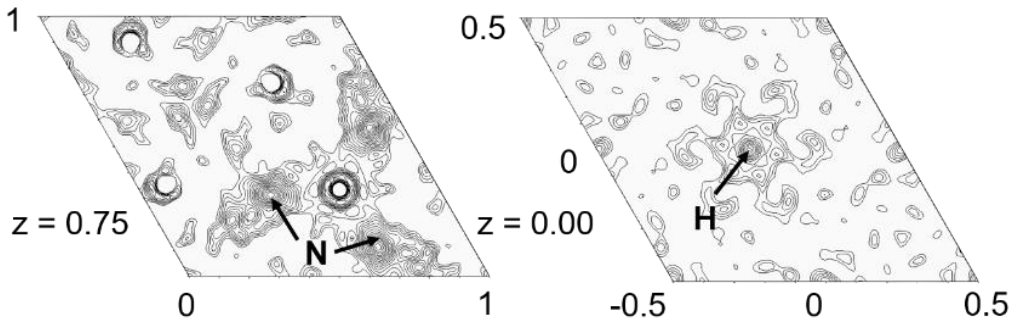

Figure 2-5. Difference Fourier maps within the *xy* plane revealing the location of N and H.

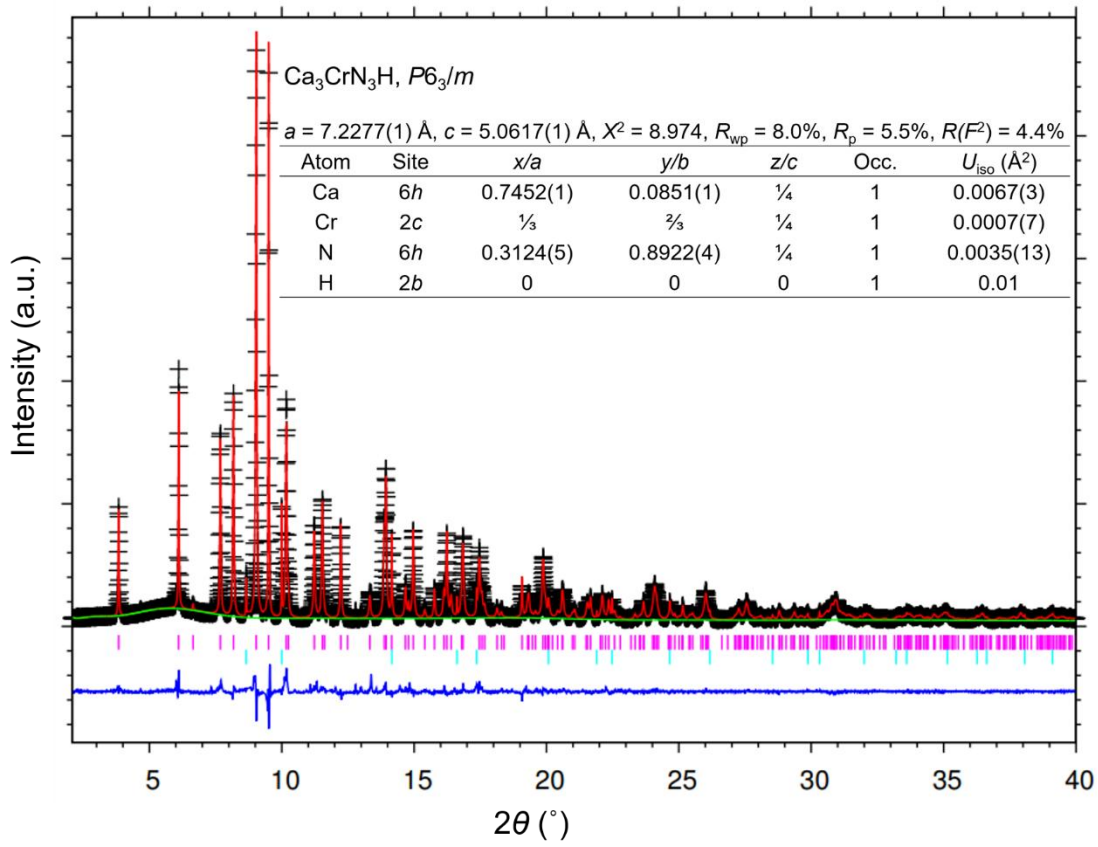

Figure 2-6. Rietveld refinement of *h*-Ca_3CrN_3H, with CaO (4.4%) impurities. Inset: structural parameters of *h*-Ca_3CrN_3H from Rietveld refinement. Black crosses, red solid line, and blue solid line represent observed, calculated, and difference intensities, respectively, while pink and cyan ticks indicate the peak positions of *h*-Ca_3CrN_3H and CaO, respectively.

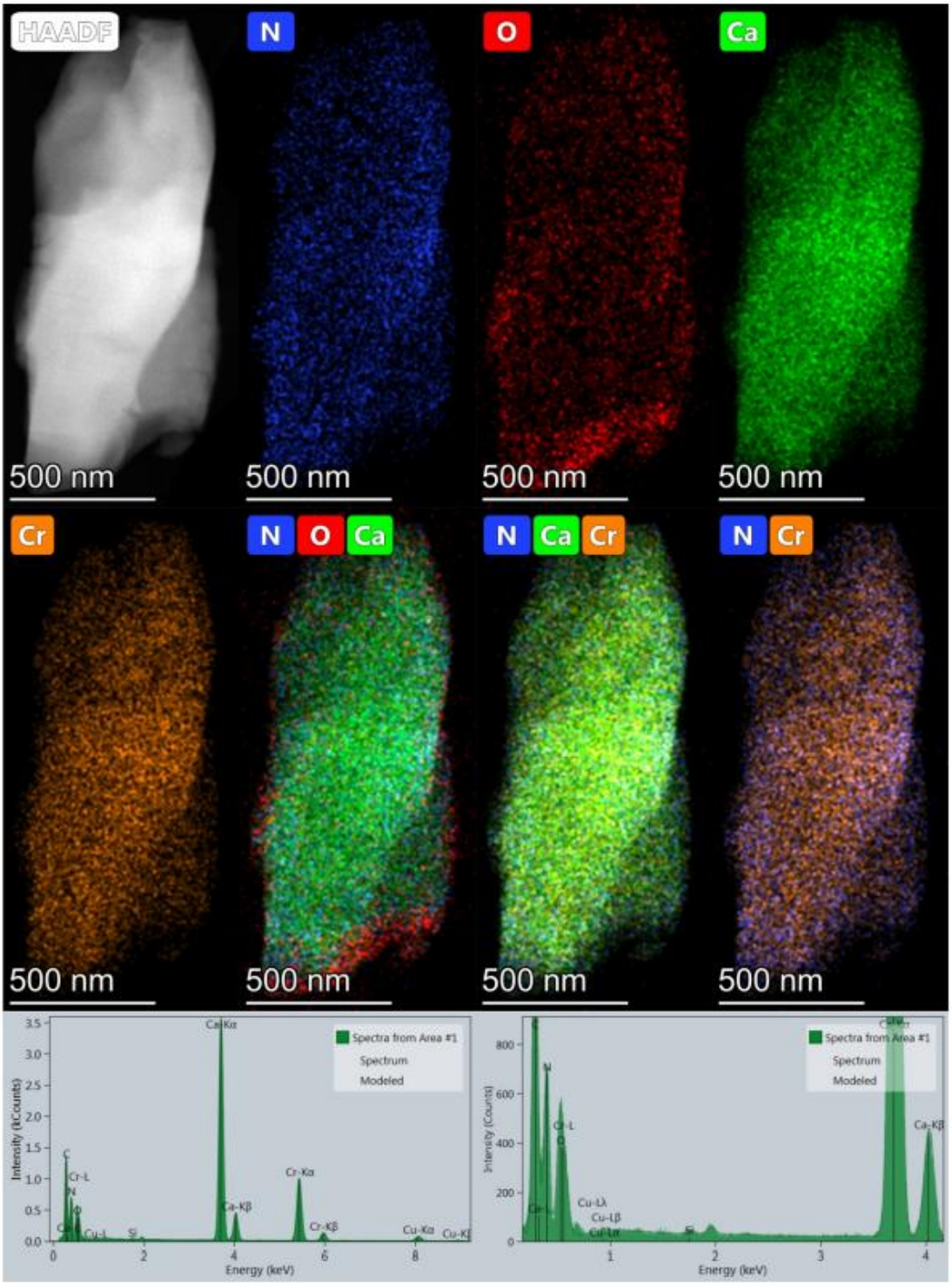

Figure 2-7. HAADF-STEM images along with corresponding EDX spectrum of the Ca_3CrN_3H.

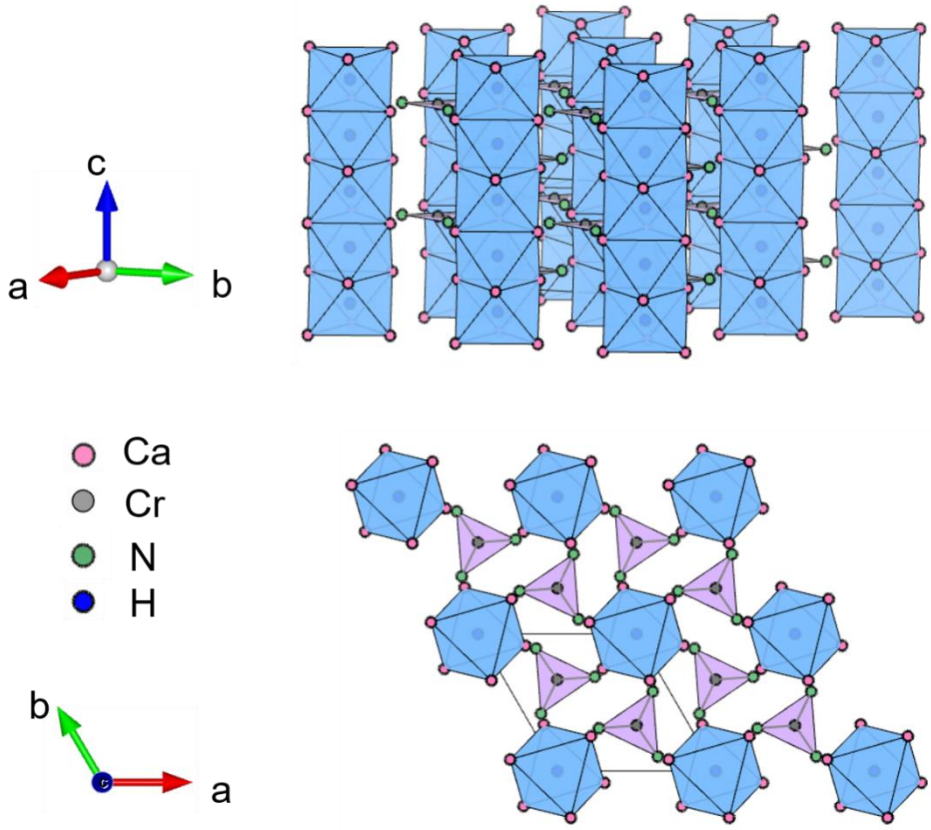

Figure 2-8. The structure of *h*-Ca_3CrN_3H. Pink, gray, green and blue spheres represent Ca, Cr, N, and H.

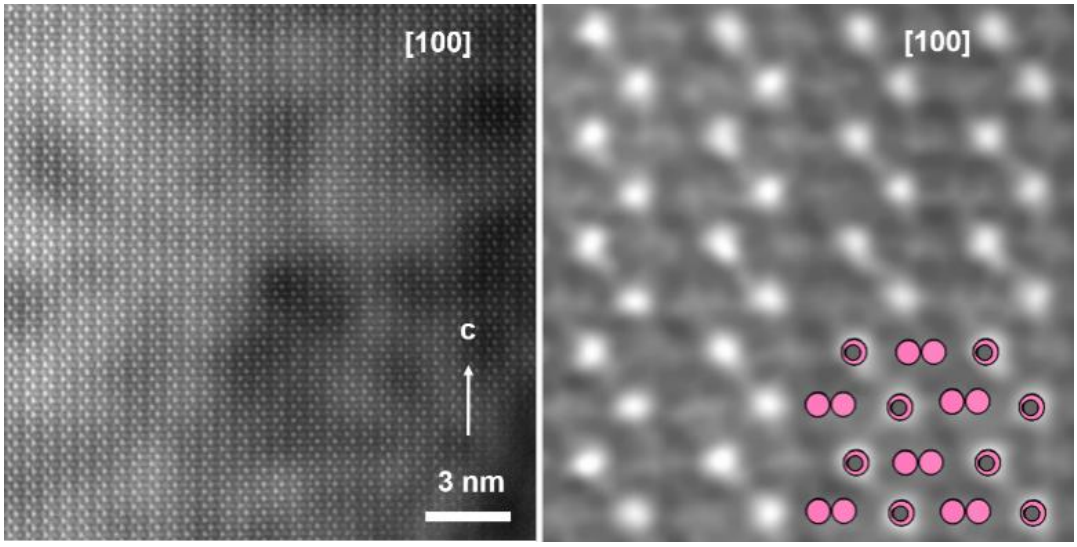

Figure 2-9. Fourier-filtered [100] HAADF-STEM images of Ca_3CrN_3H with superimposed projection of the crystal structure (only Ca and Cr are shown). The bright spots correspond to Ca-Cr columns.

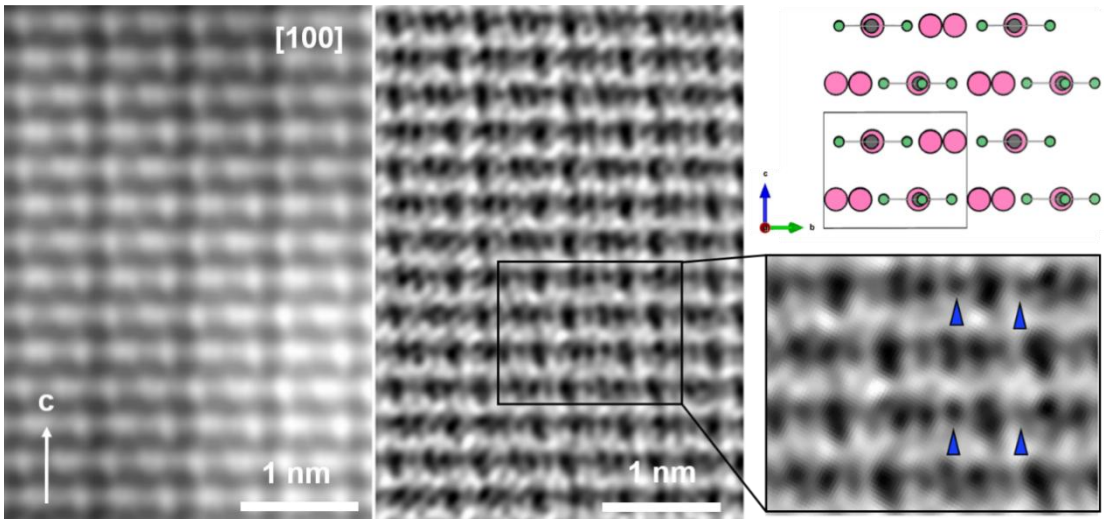

Figure 2-10. Fourier-filtered iDPC and dDPC maps; atom columns of N are marked by blue triangles. While integrated DPC (iDPC) maps look quite similar to HAADF-STEM images, the contrast on differential dDPC maps is inverted and atomic columns appear as black dots.

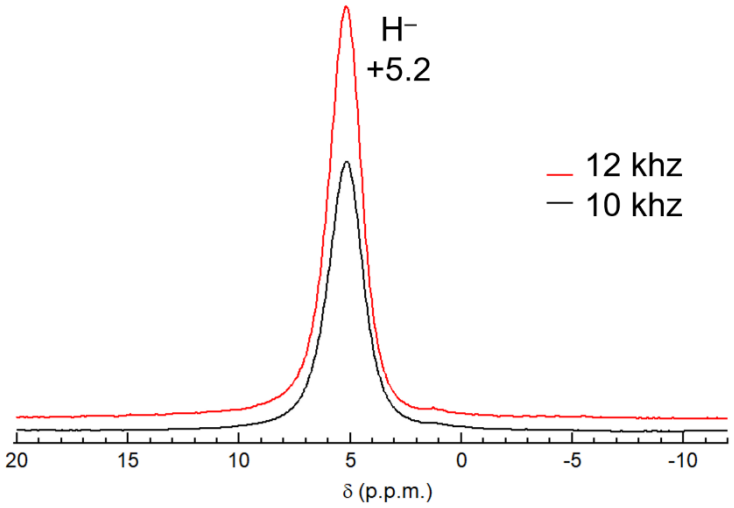

Figure 2-11. ^{1}H MAS solid-state NMR spectra of *h*-Ca_3CrN_3H (acquired at 400 MHz with a 10 kHz and 12 kHz MAS frequency).

Table 2-1. The amount of hydride in *h*-Ca_3CrN_3H determined by calibration curve.

Compound	*m*/mg	*n*/mmol	*n*(H)/mmol	Peak area/A·min	number of H
$VH_{0.39}$	1.5	0.0292	0.0114	2.00×10^{-9}	0.39
$VH_{0.39}$	4.0	0.0779	0.0304	5.30×10^{-9}	0.39
$VH_{0.39}$	4.7	0.0916	0.0357	6.00×10^{-9}	0.39
$VH_{0.39}$	8.7	0.1695	0.0661	1.14×10^{-8}	0.39
$VH_{0.39}$	17.5	0.3409	0.1330	2.20×10^{-8}	0.39
h-$Ca_3CrN_3H_x$	9.5	0.0444	0.0310	6.40×10^{-9}	0.70

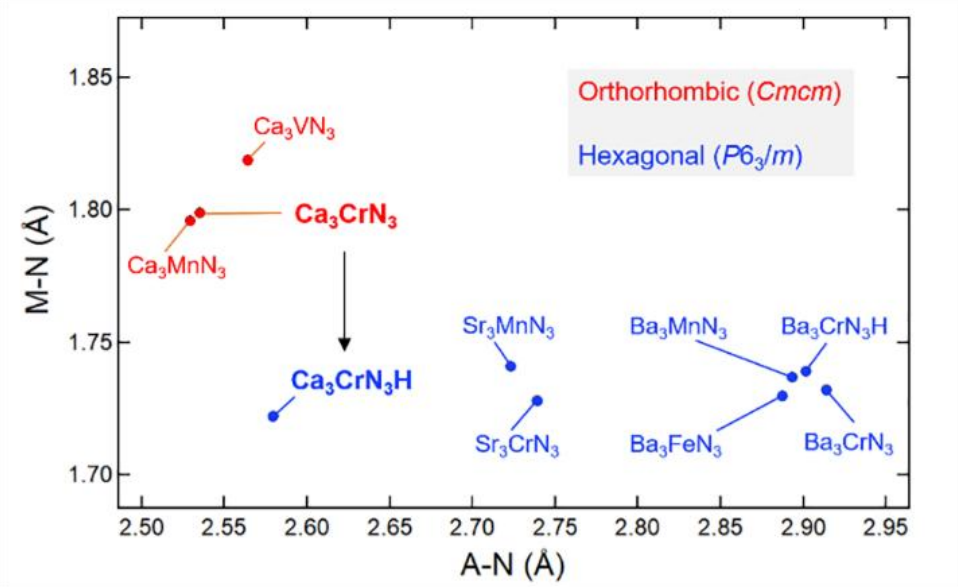

Figure 2-12. Various A_3MN_3 compounds (modified from [31]). To avoid ambiguities in defining the *A*-site radii, bond lengths have been used on the axes instead.

Table 2-2. The amount of hydride in *h*-Ca_3CrN_3H determined by calibration curve.

Compound	E_{ortho} (*Cmcm*) - E_{hex} ($P6_3/m$) (per formula unit)/ meV
Ca_3CrN_3	-330
Sr_3CrN_3	300
Ba_3CrN_3	870

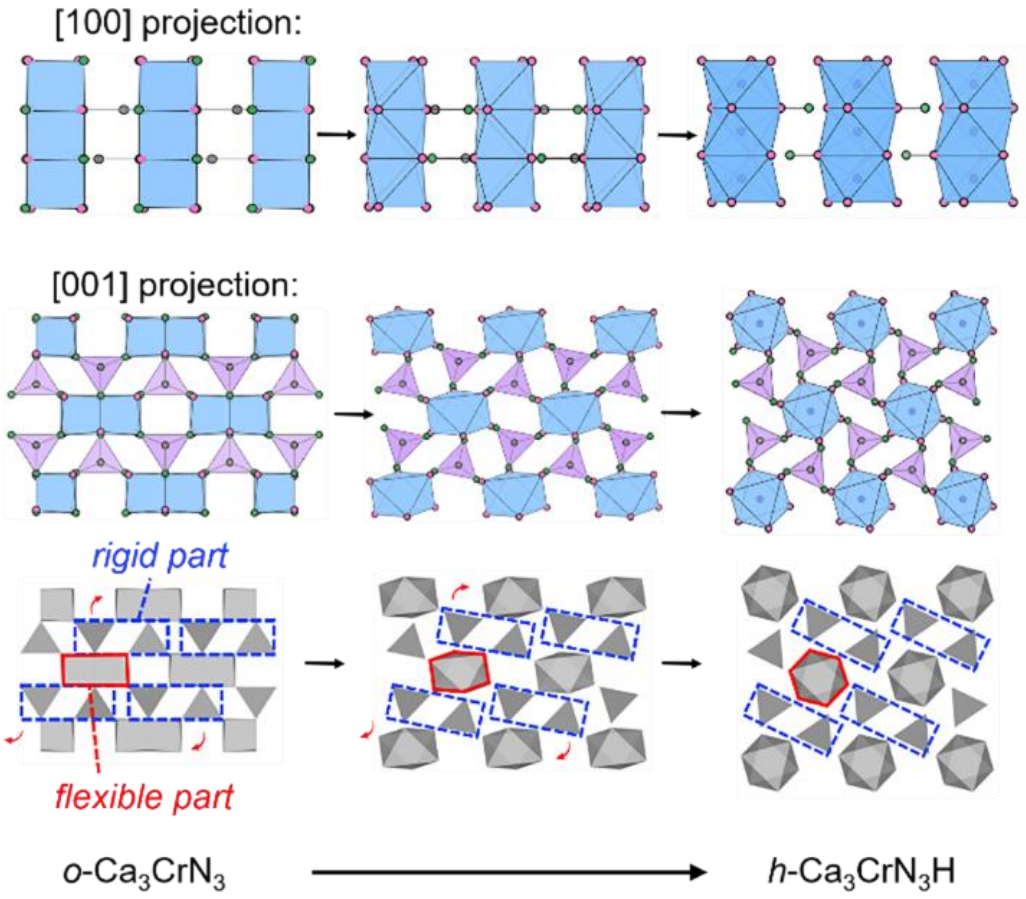

Figure 2-13. Proposed structure transformation from *o*-Ca_3CrN_3 to *h*-Ca_3CrN_3H. The lower half of the figure is a 001 projection, so the [CrN_3] units attach to the rock salt units in different *z* planes. The middle intermediate state was not observed experimentally.

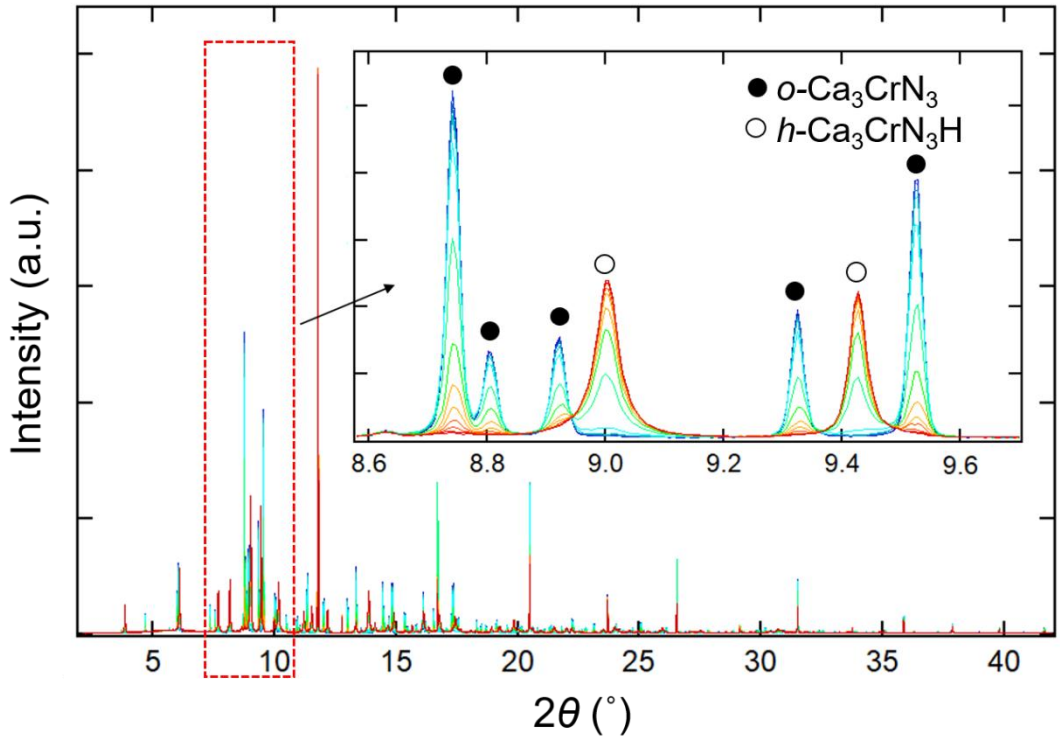

Figure 2-14. XRD patterns of the conversion from *o*-Ca_3CrN_3 to *h*-Ca_3CrN_3H under H_2 at 713 K. Inset: XRD pattern between 8.6° and 9.7°.

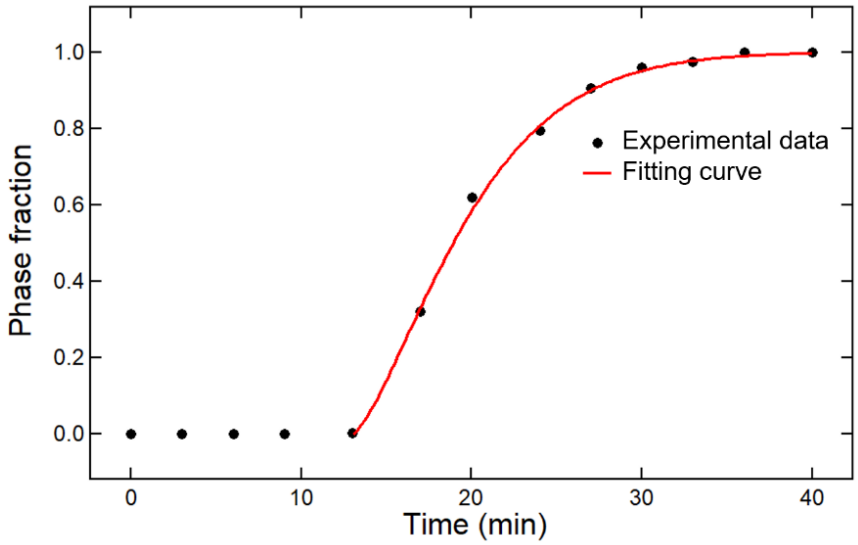

Figure 2-15. Phase fractions of *h*-Ca_3CrN_3H versus time. The Avrami exponent *n* can be fit as 1.39 (red curve).

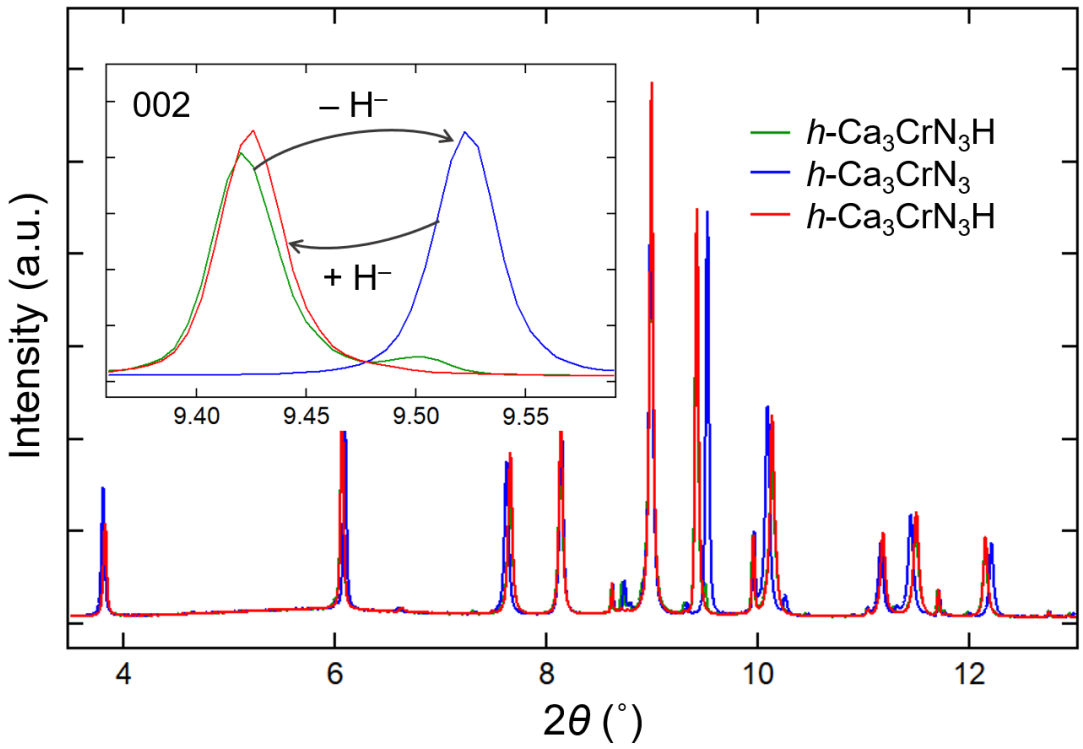

Figure 2-16. The dehydrogenation of *h*-Ca_3CrN_3H (green) to *h*-Ca_3CrN_3 (blue) and the following reversible hydrogenation to *h*-Ca_3CrN_3H (red). Inset: view of (002) peaks.

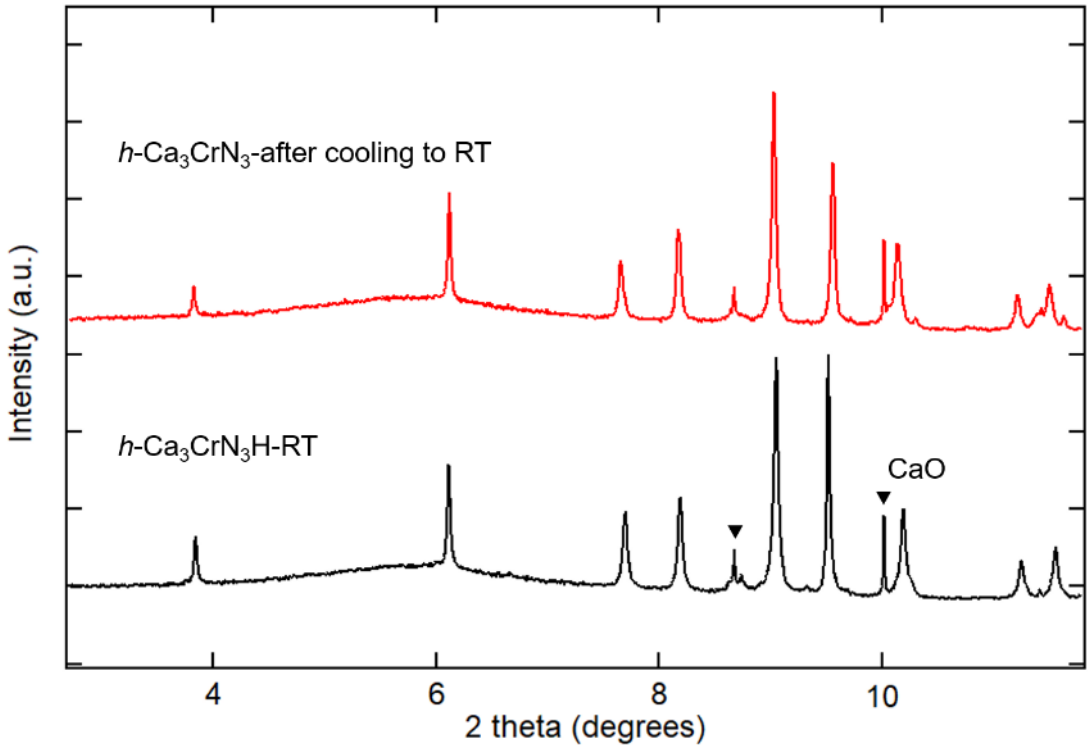

Figure 2-17. SPXRD pattern of *h*-Ca_3CrN_3 (room temperature). *h*-Ca_3CrN_3H is the starting measurement (black trace), showing a hexagonal structure at room temperature. After raising temperature to 1073 K (rate 50 K/min), H_2 was released and *h*-Ca_3CrN_3 was generated. *h*-Ca_3CrN_3 retained the hexagonal structure after cooling to room temperature (red trace, cooling rate 40 K/min).

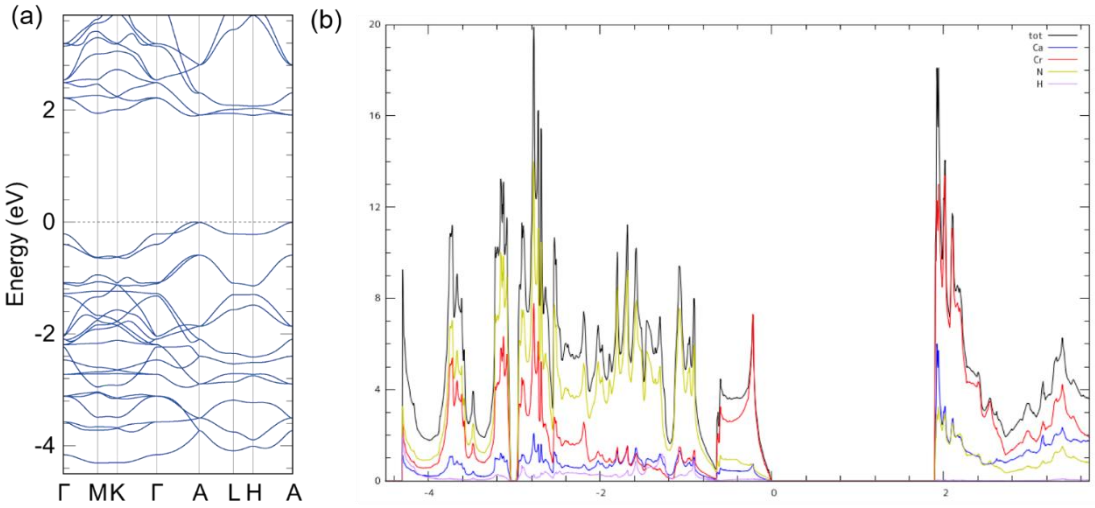

Figure 2-18. (a) Band structure (b) pDOS calculation of *h*-Ca_3CrN_3H.

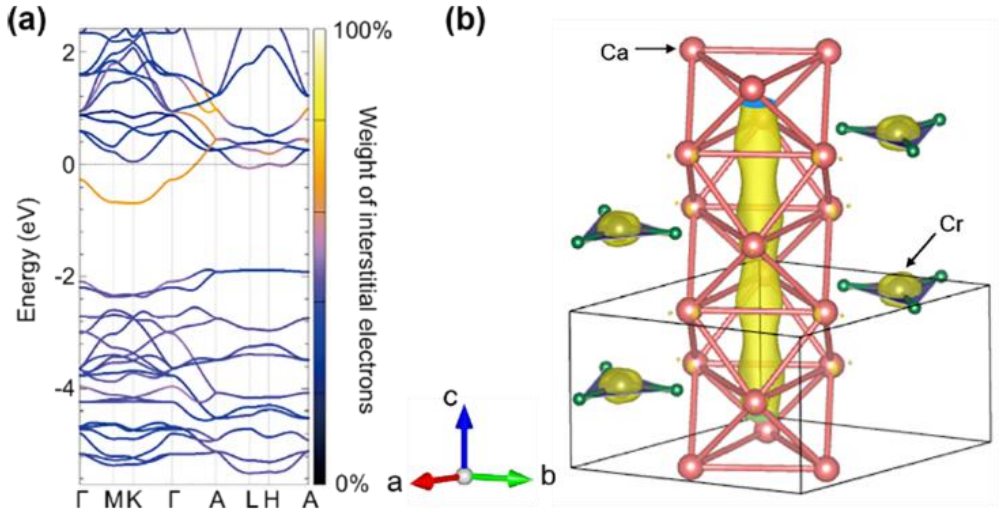

Figure 2-19. (a) Band structures of *h*-Ca_3CrN_3. (b) Partial charge density map for electrons with their eigenvalues in the energy range of [-0.8: 0.0] eV relative to the Fermi level. Yellow regions denote accumulation of charge density.

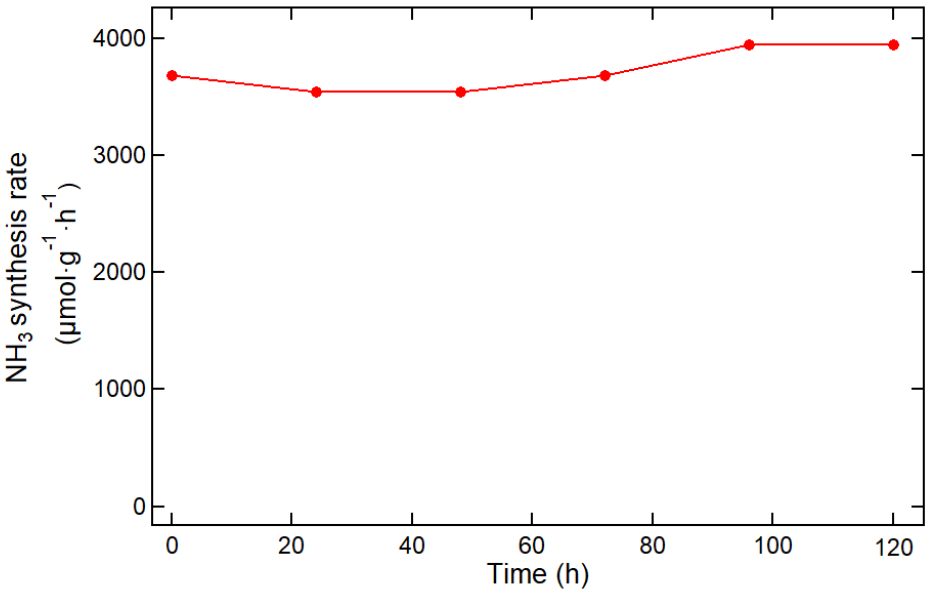

Figure 2-20. *h*-Ca_3CrN_3H catalyst remained stable over 120 hrs without degradation in activity (at 5 MPa and 673 K).

Chapter 3.

The Mechanism Study of Ca_3CrN_3H Catalyzed Ammonia Synthesis

3.1. Introduction

At present, the Haber-Bosch process is a mainstay reaction for the synthesis of ammonia under harsh conditions (400−500°C, 100−200 atm).[1] During the process, the cleavage of the inert dinitrogen triple bond is broadly viewed as the rate-determining step and transition metals are necessary for weakening and breaking the strong N≡N triple bond. In general, there are two proposed mechanisms of N_2 reduction to NH_3; the dissociative mechanism (where N_2 molecules are dissociated first on catalyst surface), and the associative mechanism (where chemisorbed N_2 undergoes stepwise hydrogenation to form NNH_x species and then undergoes cleavage of the N-N bond).[2] In conventional heterogeneous systems such as Fe- and Ru-based catalysts, N_2 activation is generally believed to follow the dissociative mechanism, and the Fe

C7 sites (composed of seven adjacent Fe atoms) on Fe(111) surface and the B5 site (five adjacent Ru atoms) of the Ru hcp surface[3] have been proposed to be the most active sites for N_2 dissociation. Most enzyme-catalysts and electrocatalysts for N_2 fixation are generally believed to go through associative adsorption and hydrogenation of the chemisorbed N_2, and these catalysts often make NH_3 synthesis under mild conditions possible.

Recently, certain heterogeneous transition-metal catalytic systems have been developed for ammonia synthesis through the associative mechanism, including Co_3Mo_3N,[4] molybdenum hydride on silica [(≡Si−O−)MoH_3],[5] Ni-LaN,[6] Ru_3 atomic clusters,[7] Ba_2RuH_6,[8-9] $KH_{0.19}C_{24}$,[10] etc. Very recently, Guan *et al.* have reported an amorphous, hydrogenated variant of Ba_5CrN_5, also exhibiting an associative mechanism, with either Ba or Cr^{3+} center assumed as the active site.[11] Recently, we reported the topochemical transformation from orthorhombic Ca_3CrN_3 to a new hexagonal antiperovskite compound Ca_3CrN_3H, in which face-sharing Ca_6 octahedra are arranged in chains along the *c* axis, and each hydrogen atom is positioned in the center of the octahedron (Figure 3-1a).[12] This compound is well-characterized structurally, and exhibits reversible hydride-electride transformation upon dehydrogenation/hydrogenation. Under Haber-Bosch conditions, catalytic activity was observed even though Cr metal is generally not an active element for ammonia synthesis due to the too strong Cr-N bond energy. However, the mechanistic details for dinitrogen reduction and ammonia formation over Ca_3CrN_3H were still not explored. Here, we further examine the catalytic performance of this new Ca_3CrN_3H compound, and the nitrogen reduction reaction pathways that occurs on the surface of the Ca_3CrN_3H were investigated in detail by theoretical studies.

3.2. Experimental

Material synthesis and characterization. Ca_3CrN_3H was synthesized following previous recipes,[12] by treating Ca_3CrN_3 under H_2 gas (>99.99999%) at 450 ^oC for 2 h and then under N_2/H_2/Ar mixed gas (22.5: 67.5: 10) at 400 ^oC for 24 h. We characterized the samples by SPXRD, which was conducted at room temperature on a

Debye-Scherrer camera at SPring-8 BL02B2 of the Japan Synchrotron Radiation Research Institute (JASRI) (λ = 0.419471(1) Å). Powder samples were loaded into Pyrex capillaries with an i.d. of 0.3 mm. VESTA was used to plot the crystal structures.[13] Ru/Ca_3CrN_3H was prepared by impregnation of the Ca_3CrN_3H support with $Ru_3(CO)_{12}$ in THF followed by carbonyl decomposition. The ICP measurement reveals a Ru content of 1.3 wt % after reaction.

Ammonia synthesis. 0.1 g catalyst was suspended in a 3/8" stainless steel tube on a bed of quartz wool. Catalyst sample was initially treated with flowing H_2 (1 bar, 90 mL/min) at 450 ºC for 2 hours. Catalytic runs were then conducted at 1-50 bar (gauge pressure), with a flow rate of 110 mL/min. Unless otherwise noted, the synthesis gas composition was N_2: H_2: Ar = 22.5: 67.5: 10, where Ar was initially intended to serve as an internal standard for calibrating a mass spectrometer. Commercially supplied gases with O_2 < 2 ppm and H_2O < 5 ppm were purified with an in-line H_2O/O_2 filter to achieve ppt-level purity. Ammonia formation was quantified by an aqueous trap (1.87×10^{-5} M NH_4Cl, 333 mL) and an ammonia-selective electrode (Horiba X 5002A).

Kinetic studies. Apparent activation energies were measured at 50 bar, over temperatures range from 623 to 723 K, with a flow rate of 110 mL/min. For reaction order measurements, gas compositions of N_2: H_2: Ar were 10: 50: 40, 16.7: 50: 33.3, 25: 50: 25, and 33.3: 50: 16.7 for determining the N_2 order, and 16.7: 33.3: 50, 16.7: 50: 33.3, 16.7: 66.7: 16.7, and 16.7: 83.3: 0 for determining the H_2 order. All measurements were conducted at 50 bar, 673 K at a flow rate of 110 mL/min. Reaction orders of NH_3 were determined by changing the flow rate of the gas (22.5: 67.5: 10) between 90, 110, 150, 200, and 250 mL/min. The data were analyzed using the method of Aika *et al*.[14]

H_2/D_2 SSITKA experiment. The catalyst (100 mg) was suspended in a quartz micro reactor (with a length of 300 mm and a diameter of 10 mm), which was inserted into a temperature-controlled oven. The catalyst was tested at 673 K and ambient pressure. The flow rates of H_2 and D_2 are both 100 mL/min. A quadrupolar mass spectrometer coupled with a computer system was used to record the signal of the reactants and products before and after the isotopic switch.

DFT calculations. We performed first-principles calculations using the plane wave based periodic DFT method as implemented in Vienna ab initio Simulation Package (VASP)[15]. The electron-ion interaction was described with the projector augmented wave (PAW) method.[16] The exchange and correlation potential was determined by Perdew-Burke-Ernzerhof (PBE) generalized gradient approximation (GGA).[17]. For dispersive intermolecular interactions and long-range van der Walls forces, dispersion corrections (DFT-D3 with Grimme function) were applied. A cutoff energy of 550 eV for expansion of the plane wave basis set was used. The convergence criteria for the electronic self-consistent iterations and forces were set to 10^{-4} eV and -0.02 eV/Å, respectively. The magnetic moment was included for the Cr atom as 3.8 to avoid the changing of magnetic moments through calculations.

Work function (ϕ) values were calculated using the following equation:[18]

$$\phi = E_{vac} - E_F \qquad \text{(DFT 1)}$$

where E_{vac} is the electrostatic potential in the vacuum region of the supercell on the adsorbate side of the slab and E_F is the Fermi level energy as calculated by the VASP code.

In order to select the most stable structure among the possible facets, we calculate the surface energies of the constructed models. The surface energies of the constructed models were calculated using the following method:[19-20]

For symmetric surfaces, we compute the surface energy (γ_{sym}) as:

$$\gamma_{sym} = \frac{E_{tot} - nE_{bulk}}{2A} \qquad \text{(DFT 2)}$$

where E_{tot} and E_{bulk} are the energies of the constructed slab and bulk parent structure, respectively. n and A are the number of formula unit in the slab and surface area of the modeled slab, respectively.

For asymmetric Ca_3CrN_3H surfaces, we select the chemical potential of the excess H on the surface to be adjusted in the former equation DFT 2.

$$\gamma_{unsym} = \frac{E_{tot} - nE_{bulk} - \frac{N}{2}E_{H_2}}{2A} \qquad \text{(DFT 3)}$$

where E_{H_2} is the DFT calculated cohesive energy of an isolated hydrogen gas molecule.

The adsorption energy of the reactants (H and N_2) and product (NH_3) we computed using:

$$E_{ads} = E_{slab+adsorbate} - E_{slab} - E_{adsorbate} \quad \text{(DFT 4)}$$

where adsorbate can be H, N_2 or NH_3. $E_{slab+adsorbate}$ and E_{slab} are the total energies of the slab with the adsorbed reactant/product and parent slab, respectively.

The adsorption energy for the all intermediates were computed with respect to the energy of gas-phase molecules of hydrogen (E_{H_2}) and nitrogen (E_{N_2}):

$$E_{ads} = E_{slab-N_xH_y^*} - (E_{slab} + \frac{x}{2}E_{N_2} + \frac{y}{2}E_{H_2}) \quad \text{(DFT 5)}$$

where $E_{slab-N_xH_y^*}$ and E_{slab} are the total energies of the slab with the intermediate and parent slab, respectively.

3.3. Results and discussions

In our preliminary work, we found that Ca_3CrN_3H exhibited good stability and catalytic activity (~3800 μmol·g^{-1}·h^{-1} at 50 bar and 673 K over 120 hrs) for ammonia synthesis despite the lack of iron and ruthenium.[12] As presented in Figure 3-1b, Ca_3CrN_3H demonstrates an activity of 865 μmol·g^{-1}·h^{-1} at ambient pressure and 673 K, which is comparable to well-known catalysts such as Co_3Mo_3N (796 μmol·g^{-1}·h^{-1}), Fe-K_2O-Al_2O_3 (330 μmol·g^{-1}·h^{-1}), and Ru-Ba/C (148 μmol·g^{-1}·h^{-1}) catalysts.[2] A kinetic analysis was also conducted; Figure 3-1c displays the Arrhenius plots of activities in the temperature range of 623−723 K. The apparent activation energy (E_a) of Ca_3CrN_3H is 75 kJ·mol^{-1}, which is comparable to other reported hydride-based catalysts such as $BaTiO_{3-x}H_x$ (80 kJ·mol^{-1})[21] and $BaCeO_{3-x}N_yH_z$ (72 kJ·mol^{-1}),[22] and much lower than conventional Ru-based catalysts (85−121 kJ·mol^{-1}).[22] Reaction orders of Ca_3CrN_3H are estimated as shown in Figure 3-1d−f. The reaction orders with respect to N_2, H_2, and NH_3 are 1.13, 2.45, and −0.48, respectively. While conventional Ru catalysts generally show negative H_2 reaction orders because of hydrogen poisoning effect, Ca_3CrN_3H is not poisoned by hydrogen with a positive H_2 reaction order.

Electrides, which have low work functions and high electron densities, facilitate N_2 dissociation on the Ru surface via electron transfer to the supported Ru particles.[3a] A similar effect is possible with hydride compounds, either by electron donation from the hydride itself, or a smaller amount of electride formed under catalytic conditions.[23] For the 001 surface of the full hydride form (Ca_3CrN_3H), we have calculated a work function of 2.75 eV (Figure 3-2), which is close to that of metallic Na or Ba.[3a] The electride form Ca_3CrN_3 has a calculated work function even lower at 2.40 eV. In reality, our samples' hydride content has been roughly estimated by TG-MS to be close to $Ca_3CrN_3H_{0.70}$,[12] so the actual work function may be at some intermediate value. The resulting electron donation properties should be a major factor in the relatively high activity observed at atmospheric pressure when Ru is deposited (1.3 wt % Ru; 1329 $\mu mol \cdot g^{-1} \cdot h^{-1}$ at 400 °C and 1 bar).

We now examine the special aspects of Ca_3CrN_3H when no Ru is supported and functions as a catalyst by itself. For other hydride catalysts, such as $BaTiO_{3-x}H_x$[21] and VH_x,[24] etc., the lattice hydride species is exchangeable with reactant H_2 gas and this hydride exchangeability plays an important role in ammonia synthesis, leading to suppression of hydrogen poisoning.[25-26] Such an effect has also been strongly suspected in materials such as $BaCeO_{3-x}N_yH_z$[14] and hydrogenated Ba_5CrN_5[11]. However, unlike these materials, Ca_3CrN_3H possesses a unique structure of 1-D tunnels where H is relatively loosely bound, and diffusion is relatively facile. In the isostructural compound Sr_3CrN_3H, a very fast H diffusion constant was predicted theoretically.[27] Additionally taking into account the reversible hydride/electride nature of Ca_3CrN_3H, we may say that a large store of lattice hydride exists, and is readily replenishable and accessible to assist NH_3 synthesis.

To demonstrate this, we have performed steady-state isotopic transient kinetic analysis (SSITKA) experiments involving a H_2/D_2 switch over Ca_3CrN_3H. Despite the presence of kinetic isotope effects, H/D SSITKA experiments have been previously reported on Pt to quantify surface hydrogen reservoirs and (de-)absorption kinetics.[28] When applied to Ca_3CrN_3H, these SSITKA experiments allow us to directly observe the exchangeable nature of the lattice hydrogen over time. As shown in Figure 3-3, in a blank experiment (dashed lines), as the gas is switched from H_2 to

D_2, the signal of HD (black dot-ted line) is quite small. In the presence of Ca_3CrN_3H, substantial HD (black solid line) is generated, indicating that H_2/D_2 exchange and scrambling occurs during the transient period. Apart from the HD, H_2 from the lattice is also being released, resulting in the slight offset between the two H_2 decay lines (blue dotted vs. solid lines). Integration of the normalized of HD signal (green line) leads to approximately 2.0 s. Since the gas flow rate is 100 mL/min, or 148.7 μmol H(D)/s, the total amount of released HD is 2974 μmol for each gram of catalyst, which amounts to approximately 60% of the bulk lattice hydride. Bulk hydride is only accessible via the ends of 1-D HCa_6 chains exposed on the particle surface; on Figure 3-1 these are equivalent to the faces on the top of the blue octahedral chains. Hence, considering the particle size and area, we can estimate the number of hydride exchange sites available. The peak height of the HD signal (~0.3) implies the HD generation TOF for each site is 275.4 s^{-1}. This exceeds to the TOF of NH_3 synthesis 2.1 s^{-1} (assuming the active sites as mentioned later), implying that during ammonia synthesis, the lattice hydride is being constantly replenished at an extremely high rate. The abundant nature of surface hydride, fueled from the bulk probably serves an important role in the hydrogenation of adsorbed N_2 species, as we see in the following mechanistic investigation.

Even though Ca_3CrN_3H exhibits catalytic activity, our preliminary results shows that the isostructural Sr_3CrN_3H has negligible activity. To gain more insights into the catalytic mechanism of the Ca_3CrN_3H catalyst, density functional theory (DFT) calculations were carried out. To find the most stable surface, we compared the (001) and (100) facets of Ca_3CrN_3H and $Ca_3CrN_3(e^-)$ in terms of surface energies. (Figure 3-2, Table 3-1). As the (001) facet of symmetric Ca_3CrN_3H slab has the lowest surface energy (0.67 J/m^2), it was selected for further study. As shown in Figure 3-4a, the surface consists of exposed CrN_3 units, and two types of Ca_3 triangles. Half of these Ca_3 holes are in fact the faces of the HCa_6 octahedra, and the other Ca_3 holes are approximately 2.6 Å above a recessed Cr atom. We found that N_2 prefers to be adsorbed via an end-on configuration on the latter Ca_3 hollow sites above the underlying Cr atom (Figure 3-4b-c). The most active site for H adsorption is also this same Ca_3 hollow site (Figure 3-5); surprisingly, the exposed CrN_3 units are less favored as N_2, N, or H adsorption sites. As already shown by the blue spheres in Figure 3-4, H adsorption on

Ca_3 hollow sites above of the CrN_3 site is also thermodynamically favorable (Table 3-2). Therefore, this surface, consisting of surface hydride resting on top of the CrN_3 site, and N_2* on the other Ca_3 holes, was used for further modeling reactivity.

There are two possible nitrogen fixation pathways in general: dissociative and associative pathways. Several possible configurations of dissociated N and adsorbed N_2 on the $Ca_3CrN_3H(001)$ surface were checked and their thermodynamic energies were compared. Figure 3-4d shows the N atoms after dissociation on Ca_3 site; the other N atom is coordinated at a neighboring equivalent Ca_3 site. However, the site is 7.20 Å away, requiring extensive surface diffusion after N−N bond dissociation. Furthermore, this arrangement is quite high in energy (2.66 eV). In Figure 3-4e, we assume dissociation of N_2* occurs with bond elongation (2.59 Å) and the bottom N to bury deeper into the Ca_3 hole towards Cr; this again results in a higher energy. Finally, as we show in Figure 3-4f, dissociation involving N* on an exposed Cr site is not energetically favorable either. In short, a dissociative mechanism necessitates two neighboring adsorption sites for each N atom; however, our catalyst surface consists of isolated active sites, making associative mechanisms favorable. Based on the high energies for N_2 dissociation, and the easy thermodynamics of N_2 hydrogenation through the associative pathways (see below), we did not investigate further the dissociative pathway.

Figure 3-6 illustrates the free energy pathway for stepwise H addition to the end-on adsorbed N_2 on the $Ca_3CrN_3H(001)$ surface. The consequent hydrogenation steps can proceed through the alternating pathway (the nitrogen atoms of N_2* are hydrogenated alternatively) or the distal pathway (the terminal nitrogen is hydrogenated preferentially). We find that both reaction pathways are competitive based on the thermodynamic profiles. The hydrogenation of N_2* to NNH* is the most energy-demanding step, with an energy cost of ~0.8 eV. The next hydrogenation will preferably occur on the surface-bound N rather than the distal N, making the alternating associative pathway favored by ~0.4 eV. The dissociation of NH=NH and NH_2NH_2 from the surface will cost 1.14 and 0.97 eV, respectively. Further addition of H atom results in the exothermic release of NH_3 and formation of NH_2* by -2.69 eV.

The role of Cr is rather indirect, taking part in only the distal pathway. In the alternating pathway, N is always at a large distance from Cr, > 4 Å (Figure 3-7). In the distal associative pathway, after releasing the first NH_3 from the surface, the remaining N can squeeze through the Ca_3 hole to approach the underlying Cr atom to form a Cr−N bond (1.70 Å; Figure 3-7). This binding occurs with negligible displacement of the surrounding three surface Ca atoms. Consequent addition of three H atoms towards formation NH_3* is also thermodynamically favored. The Cr−N distance increases slightly upon the first H addition to NH* (1.86 Å), and then this Cr−N bond is essentially broken upon addition of the second H atom to NH_2* (Cr−N 4.00 Å). Finally, desorption of ammonia from the surface is endothermic by ~0.8 eV, which is comparable to the value calculated for some effective nitrogen reduction reaction catalysts.[29-30]

3.4. Conclusion

We show that unlike many other early transition metal hydride catalysts, N_2 activation and hydrogenation over Ca_3CrN_3H involves the alkali earth cations Ca, rather than the Cr sites as one would normally expect. Of course, this does not mean alkali earth hydrides in general are catalytically active; for example, CaH_2 is known to be inactive.[21] The activity of Ca_3CrN_3H is a result of carefully arranged Ca_3 holes (probably modified electronically by a distant Cr), closely positioned near hydride channels which are in fast equilibrium with gaseous H_2. This results in the activity, and the diluted active sites on the surface area due to inherent structure help enforce an associative mechanism.

The question remains as to how general this mechanism can be and how many other materials may function in the same way. Chen *et al*. have emphasized the important roles of alkali and alkaline earth metals in dinitrogen activation and ammonia synthesis.[31] To our knowledge, there are so far only a few reports in which the activation of N_2 has been demonstrated to take place on the alkali or alkaline metal center (Ba_2RuH_6,[9] $KH_{0.19}C_{24}$,[10] a low-valent Ca complex, (BDI)Ca–Ca(BDI),[32]). Our preliminary results with isostructural Sr_3CrN_3H show negligible activity, so the

choice of alkali earth metal indeed makes a difference. There are many other materials with similar 1-D hydride structures, based on A_3MN_3 analogues (*A* is typically alkaline earth metal Ca, Sr or Ba, and *M* is transition metal V, Cr, Mn or Fe),[33-34] intermetallics, phosphates, and borates; changing the *d*-electron count by different choice of M may further enhance the activity. The recently reported hydrogenated Ba_5CrN_5-related material (consisting of Cr^{3+}, as opposed to Cr^{4+} as in Ca_3CrN_3H) also has been demonstrated to promote an associative mechanism.[11] Here, the long-range structure is amorphous, but thought to locally reflect structure of Ba_5CrN_5, with edge-sharing $(H,N)Ba_6$ octahedral dimers and isolated CrN_4 tetrahedra. While the active sites were not identified with this material, our proposed mechanism for Ca_3CrN_3H shows how the alkali earth centers can be critical, and in general of the future potential with how these alkali-earth metal hydride catalysts can function.

References

[1] a) Q. Wang, J. Guo, P. Chen, *J. Energy Chem.* **2019**, *36*, 25–36; b) S. L. Foster, S. I. P. Bakovic, R. D. Duda, S. Maheshwari, R. D. Milton, S. D. Minteer, M. J. Janik, J. N. Renner, L. F. Greenlee, *Nat Catal* **2018**, *1*, 490–500.

[2] a) S. Wang, F. Ichihara, H. Pang, H. Chen, J. Ye, *Adv. Funct. Mater.* **2018**, *28*, 1803309; b) V. S. Marakatti, E. M. Gaigneaux , *ChemCatChem* **2020**, *12*, 5838–5857; c) H. Fang, D. Liu, Y. Luo, Y. Zhou, S. Liang, X. Wang, B. Lin, L. Jiang, *ACS Catal.* **2022**, *12*, 3938–3954.

[3] a) H. Hosono, M. Kitano, *Chem. Rev.* **2021**, *121*, 3121–3185; b) J. Humphreys, R. Lan, S. Tao, *Adv. Energy Sustain. Res.* **2021**, *2*, 2000043.

[4] C. D. Zeinalipour-Yazdi, J. S. J. Hargreaves, C. R. A. Catlow, *J. Phys. Chem. C* **2018**, *122*, 6078–6082.

[5] L. M. Azofra, N. Morlanés, A. Poater, M. K. Samantaray, B. Vidjayacoumar, K. Albahily, L. Cavallo, J. M. Basset, *Angew. Chem. Int. Ed.* **2018**, *57*, 15812–15816.

[6] T. N. Ye, S. W. Park, Y. Lu, J. Li, M. Sasase, M. Kitano, T. Tada, H. Hosono, *Nature* **2020**, *583*, 391–395.

[7] L. Li, Y. F. Jiang, T. Zhang, H. Cai, Y. Zhou, B. Lin, X. Lin, Y. Zheng, L. Zheng, X. Wang, C. Q. Xu, C. tong Au, L. Jiang, J. Li, *Chem* **2022**, *8*, 749–768.

[8] Q. Wang, J. Pan, J. Guo, H. A. Hansen, H. Xie, L. Jiang, L. Hua, H. Li, Y. Guan, P. Wang, W. Gao, L. Liu, H. Cao, Z. Xiong, T. Vegge, P. Chen, *Nat. Catal.* **2021**, *4*, 959–967.

[9] C. Liu, Q. Wang, J. Guo, T. Vegge, P. Chen, H. A. Hansen, *ACS Catal.* **2022**, *12*, 4194–4202.

[10] F. Chang, I. Tezsevin, J. W. de Rijk, J. D. Meeldijk, J. P. Hofmann, S. Er, P. Ngene, P. E. de Jongh, *Nat. Catal.* **2022**, *5*, 222–230.

[11] Y. Guan, W. Zhang, Q. Wang, C. Weidenthaler, A. Wu, W. Gao, Q. Pei, H. Yan, J. Cui, H. Wu, S. Feng, R. Wang, H. Cao, X. Ju, L. Liu, T. He, J. Guo, P. Chen, *Chem Catal.* **2021**, 1042–1054.

[12] Y. Cao, M. A. Kirsanova, M. Ochi, W. al Maksoud, T. Zhu, R. Rai, S. Gao, T. Tsumori, S. Kobayashi, S. Kawaguchi, E. Abou-Hamad, K. Kuroki, C. Tassel, A. M. Abakumov, Y. Kobayashi, H. Kageyama, *Angew. Chem. Int. Ed.* **2022**, *61*, e202209187.

[13] K. Momma, F. Izumi, *J. Appl. Crystallogr.* **2011**, *44*, 1272−1276.

[14] R. Kojima, K. Aika, *Appl. Catal. A* **2001**, *218*, 121−128.

[15] a) G. Kresse, J. Furthmüller, *Comput. Mater. Sci.* **1996**, *6*, 15–50; b) G. Kresse, J. Furthmüller, *Phys. Rev. B* **1996**, *54*, 11169–11186.

[16] a) P. E. Blöchl, *Phys. Rev. B Condens. Matter* **1994**, *50*, 17953–17979; b) D. Joubert, *Phys. Rev. B - Condens. Matter Mater. Phys.* **1999**, *59*, 1758–1775.
[17] J. P. Perdew, K. Burke, M. Ernzerhof, *Phys. Rev. Lett.* **1996**, *77*, 3865–3868.
[18] A. Etxebarria, S. L. Koch, O. Bondarchuk, S. Passerini, G. Teobaldi, M. Á. Muñoz-Márquez, *Adv. Energy Mater.* **2020**, *10*, 2000520.
[19] J. C. W. Swart, P. van Helden, E. van Steen, *J. Phys. Chem. C Nanomater. Interfaces* **2007**, *111*, 4998–5005.
[20] X. Tian, T. Wang, L. Fan, Y. Wang, H. Lu, Y. Mu, *Appl. Surf. Sci.* **2018**, *427*, 357–362.
[21] Y. Kobayashi, Y. Tang, T. Kageyama, H. Yamashita, N. Masuda, S. Hosokawa, H. Kageyama, *J. Am. Chem. Soc.* **2017**, *139*, 18240–18246.
[22] M. Kitano, J. Kujirai, K. Ogasawara, S. Matsuishi, T. Tada, H. Abe, Y. Niwa, H. Hosono, *J. Am. Chem. Soc.* **2019**, *141*, 20344–20353.
[23] M. Kitano, Y. Inoue, H. Ishikawa, K. Yamagata, T. Nakao, T. Tada, S. Matsuishi, T. Yokoyama, M. Hara, H. Hosono, *Chem. Sci.* **2016**, *7*, 4036–4043.
[24] Y. Cao, A. Saito, Y. Kobayashi, H. Ubukata, Y. Tang, H. Kageyama, *ChemCatChem* **2021**, *13*, 191–195.
[25] Y. Kobayashi, O. J. Hernandez, T. Sakaguchi, T. Yajima, T. Roisnel, Y. Tsujimoto, M. Morita, Y. Noda, Y. Mogami, A. Kitada, M. Ohkura, S. Hosokawa, Z. Li, K. Hayashi, Y. Kusano, J. E. Kim, N. Tsuji, A. Fujiwara, Y. Matsushita, K. Yoshimura, K. Takegoshi, M. Inoue, M. Takano, H. Kageyama, *Nat. Mater.* **2012**, *11*, 507–511.
[26] a) Y. Tang, Y. Kobayashi, K. Shitara, A. Konishi, A. Kuwabara, T. Nakashima, C. Tassel, T. Yamamoto, H. Kageyama, *Chem. Mater.* **2017**, *29*, 8187–8194; b) Y. Tang, Y. Kobayashi, N. Masuda, Y. Uchida, H. Okamoto, T. Kageyama, S. Hosokawa, F. Loyer, K. Mitsuhara, K. Yamanaka, Y. Tamenori, C. Tassel, T. Yamamoto, T. Tanaka, H. Kageyama, *Adv. Energy Mater.* **2018**, *8*, 1801772.
[27] M. Xu, C. Wang, B. J. Morgan, L. A. Burton, *J. Mater. Chem. C* **2022**, *10*, 6628–6633.
[28] M. G. Basallote, S. Bernal, J. M. Gatica, M. Pozo, *Appl. Catal. A Gen.* **2002**, *232*, 39–50.
[29] L. Lin, L. Gao, K. Xie, R. Jiang, S. Lin, *Phys. Chem. Chem. Phys.* **2020**, *22*, 7234–7240.
[30] Z. Xu, R. Song, M. Wang, X. Zhang, G. Liu, G. Qiao, *Phys. Chem. Chem. Phys.* **2020**, *22*, 26223–26230.
[31] Q. Wang, J. Guo, P. Chen, *Chem* **2021**, *7*, 3203–3220.

[32] B. Rösch, T. X. Gentner, J. Langer, C. Färber, J. Eyselein, L. Zhao, C. Ding, G. Frenking, S. Harder, *Science* **2021**, *371*, 1125–1128.
[33] M. G. Barker, M. J. Begley, P. P. Edwards, D. H. Gregory, S. E. Smith, *J. Chem. Soc. - Dalt. Trans.* **1996**, 1–5.
[34] R. B. King, *Can. J. Chem.* **1995**, *73*, 963–971.

Figures

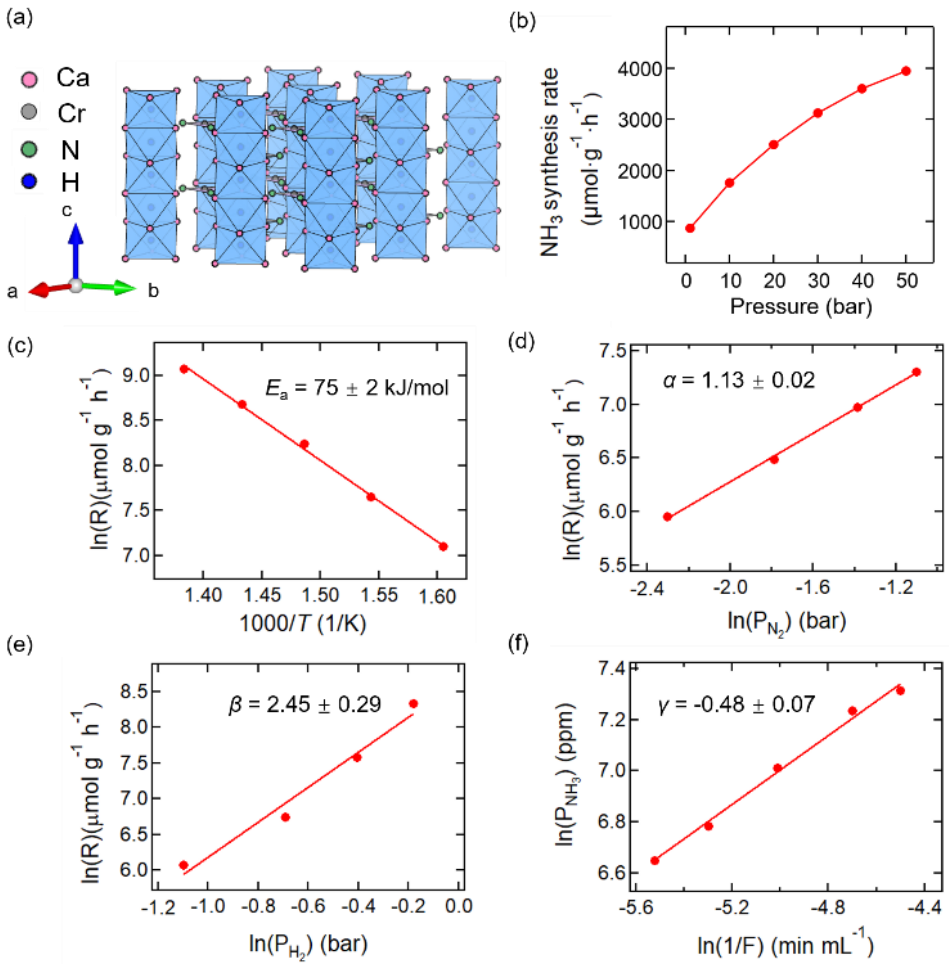

Figure 3-1. Catalytic performance and kinetic parameters. (a) The structure of Ca_3CrN_3H. (b) Pressure dependence of the ammonia synthesis rate for Ca_3CrN_3H at 673 K. (c) Arrhenius plot of Ca_3CrN_3H catalyst in the temperature over 623-723 K under 50 bar. (d) to (f) are the dependences of ammonia synthesis rates on the partial pressures of N_2 (d), H_2 (e) and NH_3 (f), respectively, under 50 bar at 673 K.

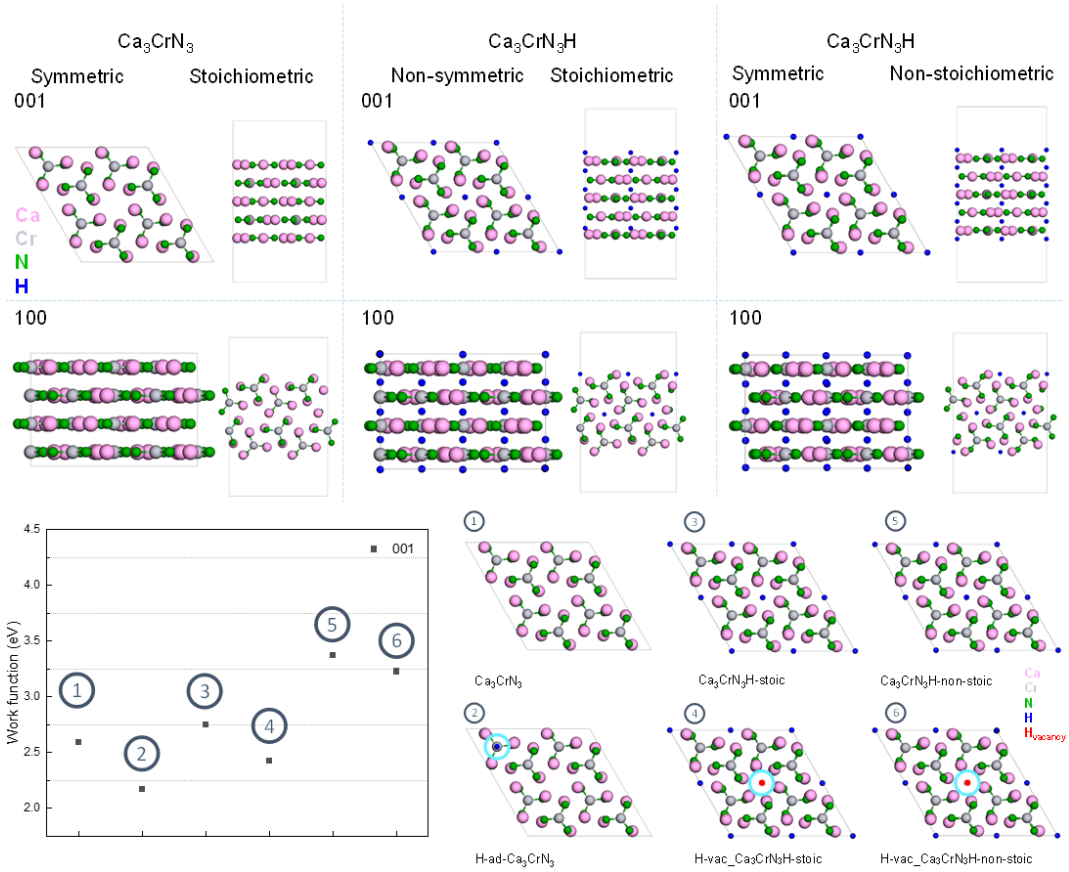

Figure 3-2. a) Completely optimized geometries of (001) and (100) slabs of Ca_3CrN_3 and Ca_3CrN_3H. b) Work function values for the modeled (001) slabs of Ca_3CrN_3 and Ca_3CrN_3H. Completely optimized geometries of (001) slabs of Ca_3CrN_3 and Ca_3CrN_3H with added H on the surface and with H vacancy on the surface, respectively. The pink, green, grey and blue colors depict Ca, N, Cr, and H atoms, respectively.

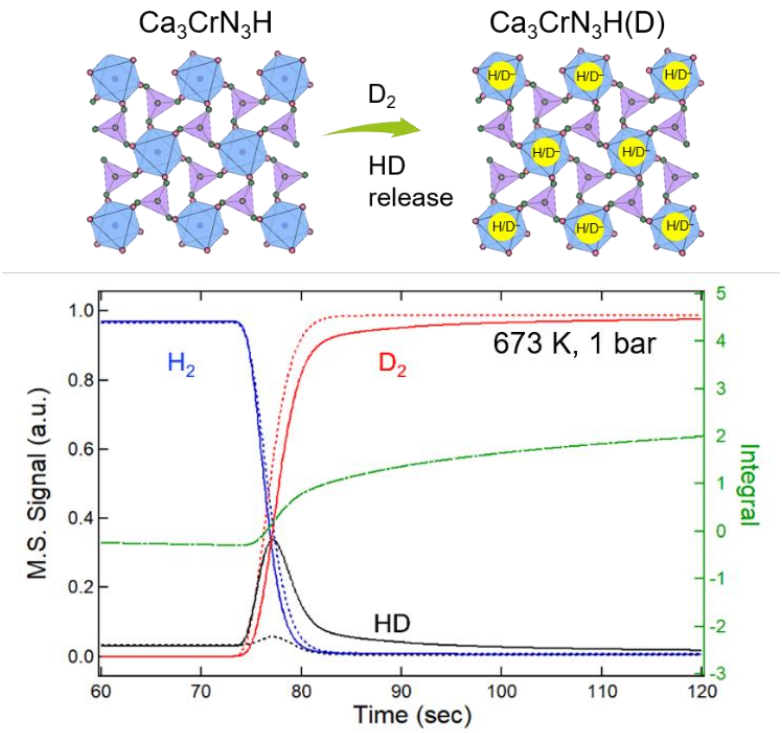

Figure 3-3. Time dependence of gas composition during H_2/D_2 exchange at 673 K and 1 bar. H_2 (D_2) gas flow rate is 100 mL·min^{-1}. Sample weight is 0.1 g. Dashed lines indicate blank experiment, and solid lines indicate experiments with Ca_3CrN_3H.

Table 3-1. Surface energy values for (001) and (100) slabs of Ca_3CrN_3 and Ca_3CrN_3H.

Compound	Geometries	Facet	$E_{surface}$ (J/m^2)
Ca_3CrN_3	Stoichiometric	001	0.82
		100	1.12
Ca_3CrN_3H	Stoichiometric (unsymmetrical)	001	0.77
		100	1.31
Ca_3CrN_3H	Non-stoichiometric (symmetrical)	001	0.67
		100	1.07

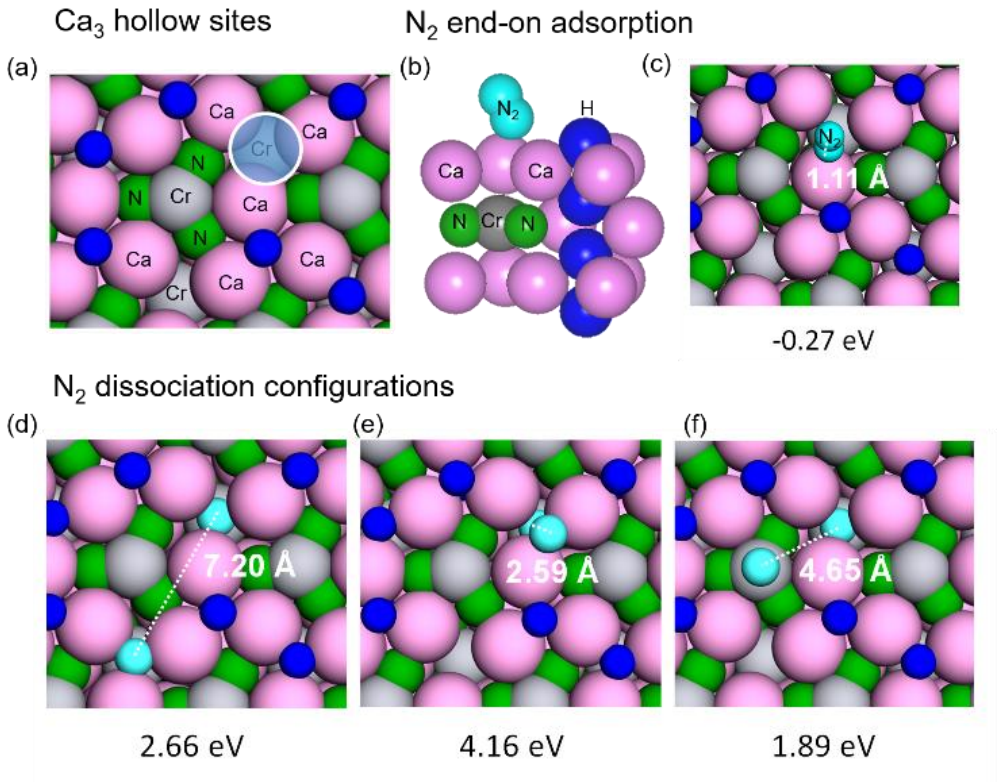

Figure 3-4. The possible configurations of dissociated N−N and adsorbed N_2 on $Ca_3CrN_3H(001)$ surface and their adsorption energies. a) surface Ca_3 hollow sites above the underlying Cr atom. b) N_2 end-on adsorption (a side view). c) N_2 end-on adsorption (viewed along the [001] direction). d) Both "N" located in two different Ca_3 hollow sites. e) "N"−"N" with one N penetrated in hollow site and another on top of it. f) One "N" in hollow site, the second "N" on neighboring Cr site. The pink, green, grey, dark blue and sky-blue colors depict Ca, N, Cr, H, and adsorbed N atoms, respectively.

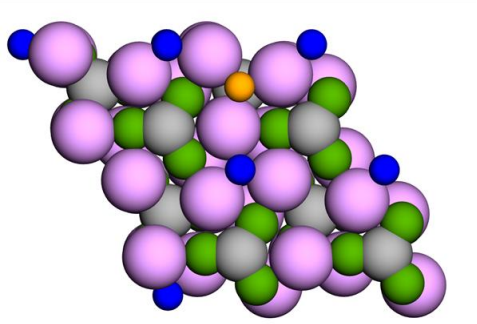

Figure 3-5. The optimized configurations of H adsorption on Ca_3CrN_3H (001) surface with the lowest formation energy. The pink, green, grey, blue, and orange colors depict Ca, N, Cr, H and H_{ads} atoms, respectively.

Table 3-2. The adsorption energy values of subsequent H adsorption on (001) slab of Ca_3CrN_3H

Number of H atom	E_{ads} (eV)
1	-0.70
2	-0.34
3	0.03
4	0.05

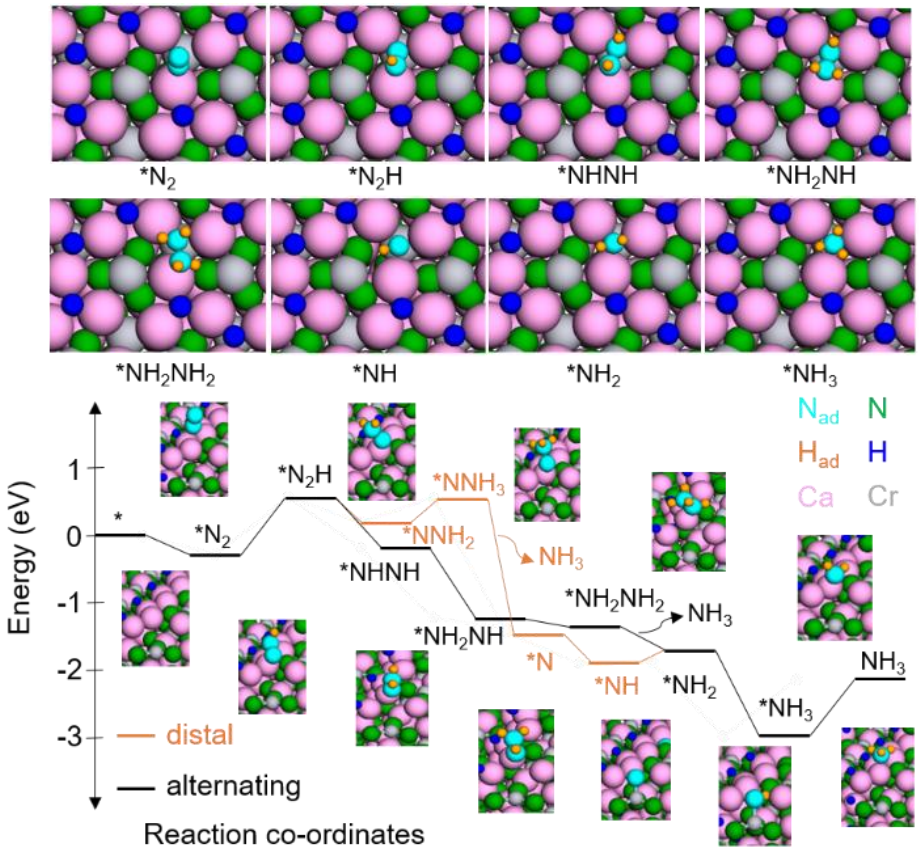

Figure 3-6. Thermodynamic reaction energy profiles for associative distal (black line) and alternating (red line) pathways for nitrogen hydrogenation to ammonia at the hollow site of three Ca atom on $Ca_3CrN_3H(001)$. The panel of structures above the graph shows the top view of intermediates at the reaction site (Ca_3 hollow site) via the more favorable alternating associative pathway. The insets in the graph are representations of the adsorbed intermediates in a side-view for both alternating and distal associative pathways. The pink, green, grey, dark blue, sky blue and orange colors depict Ca, N, Cr, surface H, adsorbed N, and adsorbed H atoms, respectively.

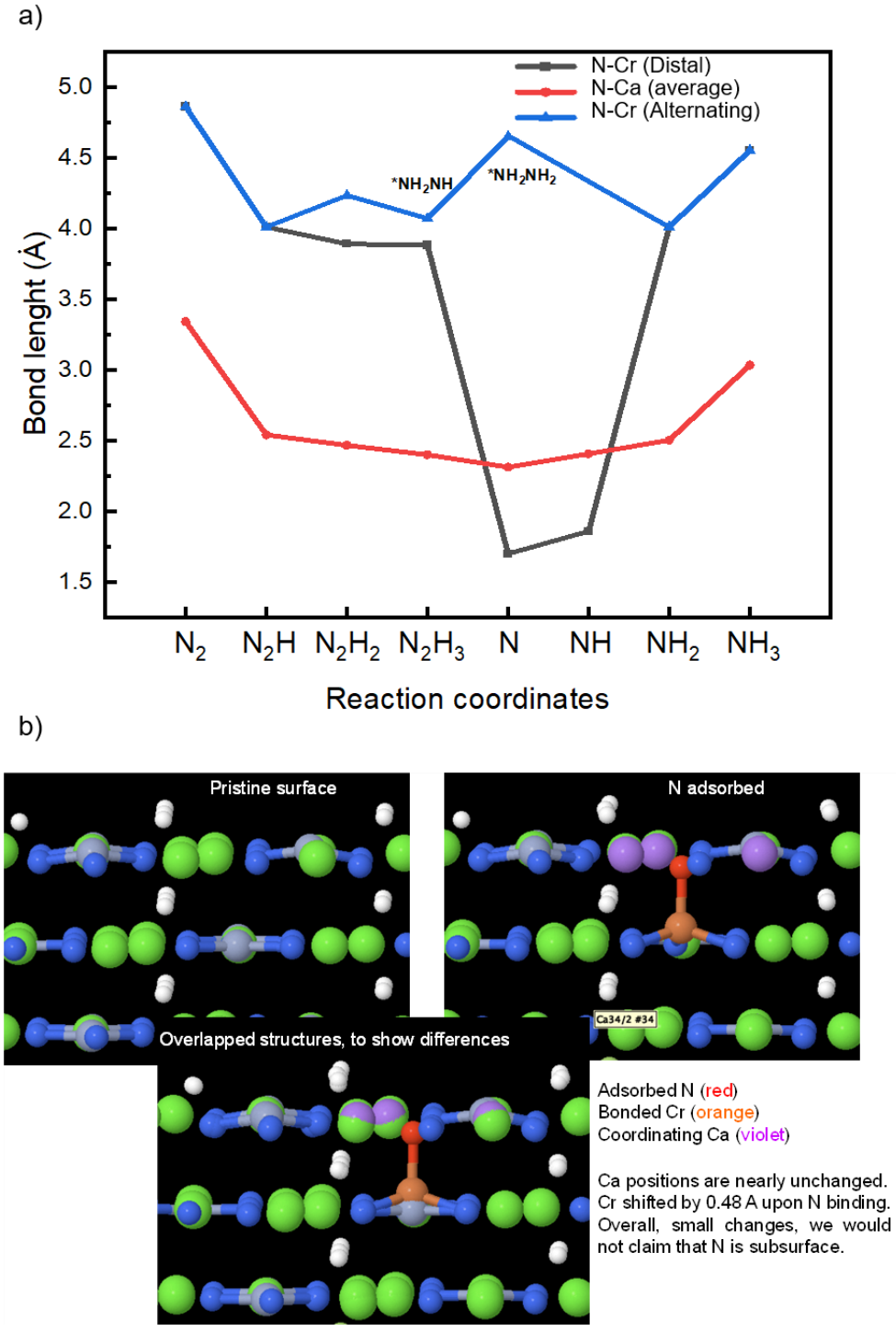

Figure 3-7. a) The Ca-N and Cr-N distances with subsequent hydrogenation of *N_2. In the distal associative pathway, the underlying Cr could attract the *N as the distal N is hydrogenated to NH_3. Further hydrogenation of *N increases Cr-N bond length. b) In the presence of an N atom, the Cr moves forward to the surface by 0.48 A.

Chapter 4.

Zr-based Laves Phases with Nitride/Hydride Ions for Ammonia Synthesis

4.1. Introduction

Hydrogen storage materials, such as AB_5-, AB_3-, AB-, and AB_2-type intermetallic compounds, where A is usually a hydride-forming element and B is a weaker hydride former, can reversibly absorb and desorb hydrogen under mild conditions via the formation of interstitial-type metal hydrides.[1] H_2 dissociates at the surface and then is stored in tetrahedral and/or octahedral interstitial sites of the metal lattice. Intermetallic compounds have been reported as promising ammonia synthesis catalysts. Takeshita *et al*. found some intermetallic compounds which involve lanthanides and Fe, Co, or Ru as synthetic ammonia catalysts with high specific activities.[2] However, XRD studies showed that these intermetallic compounds were

decomposed into lanthanide nitride and finely divided transition metal that appears to be the active phase.

An AB_5-type intermetallic hydride, $LaNi_5H_6$, has been reported for ammonia synthesis under 5 MPa at room temperature.[3] A possible mechanism for nitrogen activation is the formation of hydrides during ammonia synthesis, which is accompanied by a large cell volume expansion and provides suitable sites for nitrogen adsorption and dissociation. In addition, the inserted hydrogen sometimes acts as an electron donor. Recently, YRu_2 intermetallic hydride has been developed for ammonia synthesis.[4] The addition of Y with less electronegativity increases the electron density over Ru and therefore facilitates N_2 dissociation and results in a reduced activation energy. RTX intermetallic compounds (R = rare earth, T = transition metal, X = *p*-block element) with electride-like natures, such as LaRuSi[5] and LaCoSi,[6] were also reported as ammonia synthesis catalysts. During the catalytic reactions, the electronegative transition metal atoms sitting in the lattice act as a strong adsorption site to N_2 and is effectively used for N_2 dissociation.

Among hydrogen storage compounds, the AB_2-type (Laves phase) intermetallic compounds, such as zirconium-based materials (ZrM_2, M = Cr, V, Ti, Mn), are reported to have high hydrogen storage capacity.[7] Laves phase compounds consist of two elements with a 1:2 molar ratio and an ideal radius ratio of 1.225 for A and B atoms, forming mostly cubic C15 and hexagonal C14 structures.[8] In both structures, all interstices in the crystal lattices are formed by tetrahedra, i.e., A_2B_2, AB_3, and B_4 type sites, as shown in Figure 4-1. As the number of A (Zr) atoms surrounding the site increases (chemical affinity effect), there is a greater tendency for the interstices to attract hydrogen, so the absorbed hydrogen will preferably occupy A_2B_2 tetrahedral interstices with some occupation in AB_3, but never enter the B_4 tetrahedron.[7] Furthermore, Laves phase hydrides AB_2H_x have a distinctly higher diffusivity than other intermetallic hydrides, due to the similar network and connectivity of tetrahedral interstitial sites with a bcc structure.[9]

Additionally, nitrogen absorption–desorption behaviour was also observed in Laves-type intermetallic compounds, e.g., ZrVFe,[10] $TiFe_2$.[11] When ammonia or nitrogen were used as nitrogen source, the crystalline samples interstitially absorbed

nitrogen into the disordered lattice and then transformed to an amorphous phase with some new phases separated. The desorption of ammonia could be observed by the subsequent hydrogenation. Thus, if AB_2 intermetallic compounds are able to activate N_2 on their surfaces or absorb nitrogen in their crystal lattices and denitrogenate under hydrogen gas, these compounds would have potential as ammonia synthesis catalysts. Here, we have developed Zr-based AB_2-type intermetallic compounds as ammonia synthesis catalysts, without using noble transition metals and rare earth metals. The large compositional range of Laves phases enables us to fine-tune hydride/nitride reaction energetics, making it a good system to explore.

4.2. Experimental

Preparation of Catalysts. ZrM_2 (M = Cr, Mn, and V) samples were prepared by arc-melting the starting elements (99.9% purity) on a water-cooled copper hearth under argon atmosphere (remelted three times to improve homogeneity and purity).[12] After melting, the ingots were crushed using a high-energy planetary ball mill (Fritsch P5). Each sample was put into an Ar-filled zirconia pot with zirconia balls and was ball-milled for 20 hrs at 400 rpm to reduce the size of particles and expose non-oxidized surfaces. The surface areas of these powders were 0.5–1.0 $m^2 \cdot g^{-1}$ as measured by the conventional BET method (N_2 physisorption). We characterized the purity and crystal structures of the samples by SPXRD, which was conducted at room temperature on a Debye-Scherrer camera at SPring-8 BL02B2 of the Japan Synchrotron Radiation Research Institute (JASRI) (λ = 0.419471(1) Å). Powder samples were loaded into Pyrex capillaries with an i.d. of 0.3 mm. VESTA was used to plot the crystal structures.[13]

Ammonia synthesis. 0.1 g ZrM_2 sample was suspended in a 3/8” stainless steel tube on a bed of quartz wool. Catalyst sample was initially treated with flowing H_2 (3 MPa, 90 mL/min) at 673 K for 3 hours. Catalytic runs were then conducted at 3 MPa (gauge pressure), with a flow rate of 110 mL/min. Unless otherwise noted, the synthesis gas composition was N_2: H_2: Ar = 22.5: 67.5: 10, where Ar was initially intended to serve as an internal standard for calibrating a mass spectrometer.

Commercially supplied gases with $O_2 < 2$ ppm and $H_2O < 5$ ppm were purified with an in-line H_2O/O_2 filter to achieve ppt-level purity. Ammonia formation was quantified by an aqueous trap (1.87×10^{-5} M NH_4Cl solution, 333 mL) and an ammonia-selective electrode (Horiba X 5002A).

Thermogravimetric and mass spectrometric (TG-MS) analysis. TG experiments were conducted with a Bruker AXS TG-DTA 2000S by heating (10 K min^{-1}) sample (ca. 20 mg) in a stream of pure Ar (>99.9999%) gas up to 1073 K. The hydrogen release upon heating was monitored under flowing Ar at 200 mL/min by a Bruker MS9610 quadrupole mass spectrometer connected to the TG instrument.

***In situ* SPXRD with controlling gas.** In order to check the nitrogen storage ability of $ZrCr_2$, *in situ* SPXRD under N_2 gas was carried out at the BL02B2 beamline in SPring-8. $ZrCr_2$ powder was load into a 0.5 mm diameter quartz glass capillary. It was connected to a stainless-steel gas cell which can introduce gas into the capillary tube. The sample was evacuated first and raise temperature to 400 ºC (or 800 ºC), and then N_2 gas pressures up to 101 kPa. The SPXRD patterns were measured *in situ* under ambient N_2 gas pressure at 400 ºC (or 800 ºC). The incident X-ray wavelength was 0.419471(1) Å.

4.3. Results and discussions

A Rietveld refinement of the synchrotron powder X-ray diffraction (SPXRD) data collected from the as-prepared $ZrCr_2$ sample shows a hexagonal C14 Laves phase (Figure 4-1, space group $P6_3/mmc$) with a small amount of Cr impurity (7.1%). The rapid quench and the lack of an annealing process are probably responsible for the formation of only the hexagonal phase here. Then, catalytic tests were conducted on milled $ZrCr_2$ at 400 °C under 3 MPa. After NH_3 synthesis, as indicated by X-ray diffraction, there was no severe chemical degradation of the initial $ZrCr_2$, but the expansion of the hexagonal unit cell took place, along with a partial formation of amorphous (Figure 4-2, Table 4-1). The SPXRD profile can be reliably fitted with the $P6_3/mmc$ structure (a = 5.2243(1) Å, c = 8.5782(5) Å, R_p = 6.8%, R_{wp} = 8.6%, GOF = 4.33).

It has been reported that hydrogen absorption into the $ZrCr_2$ metal lattice could form a hydride phase[12] and is typically accompanied by a modest (few percent) increase in the volume (the volume increase per hydrogen atom was 2.2 $Å^3$ for $ZrCr_2H_x$). [14] Using a comparison with the literature values of lattice parameters[14] and assuming that hydrogen is the only inserted species, the equivalent hydrogen content would be ~1.2. In our case, exposure of $ZrCr_2$ to N_2/H_2 at 400 °C was accompanied not only by hydrogenation but also nitrogenation, and the amounts of hydrogen and nitrogen were determined to be 0.6 wt%, and 2.7 wt% respectively, by combustion elemental analysis. Considering that the intermetallic compound decomposes slightly into Cr and N-containing impurity (ZrN), a Rietveld refinement was conducted to find approximate phase fractions and the N/H content in $ZrCr_2N_xH_y$. Since no hydride impurities was detected, elemental analysis gives y = 1.4. ZrN phase fraction was found (1.9 wt%), and subtracting this contribution from N by elemental analysis yields x = 0.4, giving the chemical formula $ZrCr_2N_{0.46}H_{1.57}$. We deduce that this increase in lattice parameter could be ascribed to H and/or N incorporation into the A_2B_2 and/or AB_3 tetrahedral sites, as shown in Figure 4-1.

In order to check the nitrogen storage ability of $ZrCr_2$, *in situ* SPXRD measurements under N_2 gas atmosphere were carried out. It turned out that heating up to 400 °C in N_2 gas under ambient pressure did not change the XRD peak intensities and lattice constants. When increasing temperature to 800 °C, severe amorphization and decomposition of $ZrCr_2$ occurred (Figure 4-3). Apparently during ammonia synthesis, nitrogen can go into the Laves structure when hydrogenation is a concurrent process. This is likely due to the cell volume expansion upon hydrogenation, which facilitates access to bulk coordination sites for nitrogen adsorption and dissociation.

Catalytic tests were conducted on ball-milled samples of ZrM_2 (M = Cr, Mn, and V) at 400 °C under 3 MPa, and the results are shown in Figure 4-4. Despite the lack of ruthenium, $ZrCr_2$ exhibited stable ammonia synthesis activity, and its ammonia synthesis rate (0.6 $mmol \cdot g^{-1} \cdot h^{-1}$) is higher than that of $ZrMn_2$ or ZrV_2. Normally, activation of N_2 with early transition metals is not catalytic due to the overly strong M-N bond. The situation changes in the presence of hydride, as TiH_2, $VH_{0.5}$, and $NbH_{0.6}$ are known to be active catalysts;[15] ZrH_2 is not active presumably as the Zr-N bond is

simply too strong for any electronic effects from hydride to overcome.[15] However, adding incorporating the additional B element modifies this situation in our case, as the (V, Cr, Mn)-N bonds are weaker than Zr-N bonds (the standard heat of formation of binary nitrides for Zr, V, Cr, Mn is −343 kJ·mol^{-1}, −172 kJ·mol^{-1}, −121 kJ·mol^{-1}, −117 kJ·mol^{-1}, respectively).[16]

In addition, the catalytic activity orders in ZrM_2 (M = Cr, Mn, and V) are reversed to the thermal stability order of the corresponding hydride compounds, i.e., ZrV_2H_x > $ZrMn_2H_x$ > $ZrCr_2H_x$.[17] We speculate that ZrV_2 and $ZrMn_2$ have lower activity also due to their excessive hydride stability. However, the hydride-forming ability at the A site cannot be too weak either, as TaV_2 has no activity at all (Figure 4-4). Note that the enthalpy of formation of binary hydrides for Ta is −39.8 kJ·mol^{-1} and for Zr, −190.3 kJ·mol^{-1}.[18] The partial substitution of the A or B element in AB_2 intermetallic compounds with other transition elements like Fe, Co, Ni, Cu, and Mn, will alter the hydride capacity, hydride stability, surface reaction and hydriding/dehydriding kinetics.[12] Then, we conducted the partial substitution of Cr in $ZrCr_2$ to get Zr($Cr_{1-x}M_x$)$_2$ (M = Fe, Co Ni, and Cu, x = 0.2). Thermogravimetric and mass spectrometric (TG-MS) analysis in Ar gas results show that the stability of the hydrides was reduced, as indicated by a lower H_2 releasing temperature (Figure 4-5). However, the catalytic tests on the ternary Laves phases failed to improve the activity. The possible reason may be that the alloying of $ZrCr_2$ with Fe/Co/Ni/Cu also weakens (destabilizes) the adsorption of N_2 on the surface. The value of standard heat of formation of nitrides of Cr (−121 kJ·mol^{-1}) is very small compared with those for Fe (−12 kJ·mol^{-1}), Ni (+0 kJ·mol^{-1}), and Cu (+75 kJ·mol^{-1}),[16] i.e., Fe, Co, Ni, and Cu have weaker M–N binding energy, which is not conducive to the dissociative adsorption of N_2 (the possible rate-limiting step). On a different note, it has been reported that the addition of alkaline metal hydride to early transition metals can extract and hydrogenate the dissociated N from transition metals and mediate the following hydrogenation to produce NH_3, leading to the enhancement of NH_3 synthesis activity.[19] Therefore, LiH (50 wt%) was added to $ZrCr_2$ by simply hand milling, as well as to Zr($Cr_{0.8}Fe_{0.2}$)$_2$. The catalytic performances have been improved successfully, despite the smaller amount of active material (ZrM_2) in the $ZrCr_2$-LiH catalyst.

4.4. Conclusion

We have examined and demonstrated the possibility of preparing a nitride-hydride phase through direct hydrogenation and nitrogenation with high-purity hydrogen and nitrogen gas. This work exhibits the potential of Zr-based AB_2-type intermetallic compounds as ammonia synthesis catalysts. However, these catalysts have low surface area (0.5–1.0 $m^2 \cdot g^{-1}$) and insufficient activity so far. For the application of hydrogen storage alloys for ammonia synthesis, further investigations could be focused on the further activity promotion with electropositive elements, such as barium which has previously been demonstrated to be excellent promoter for Ru or Fe-based catalysts. Zr-based AB_2-type intermetallic compounds may also behave as potential supports for Ru metal. To have a deeper understanding of explicit experimental data on the N_2/H_2 adsorption (nitrogenation/hydrogenation) enthalpies may also benefit rational catalyst design for intermetallic compounds catalysed ammonia synthesis.

References

[1] N. A. A. Rusman, M. Dahari, *Int. J. Hydrogen Energy* **2016**, *41*, 12108–12126; A. Züttel, *Mater. Today* **2003**, *6*, 24–33.

[2] T. Takeshita, *J. Catal.* **1976**, *44*, 236–243; A. P. Walker, T. Rayment, R. M. Lambert, *J. Catal.* **1989**, *117*, 102–120.

[3] H. Y. Zhu, *J. Alloys Compd.* **1996**, *240*, L1–L3.

[4] T. Ogawa, Y. Kobayashi, H. Mizoguchi, M. Kitano, H. Abe, T. Tada, Y. Toda, Y. Niwa, H. Hosono, *J. Phys. Chem. C* **2018**, *122*, 10468–10475.

[5] H. Hosono, M. Kitano, *Chem. Rev.* **2021**, *121*, 3121–3185; J. Wu, J. Li, Y. Gong, M. Kitano, T. Inoshita, H. Hosono, *Angew. Chem. Int. Ed.* **2019**, *58*, 825–829.

[6] Y. Gong, J. Wu, M. Kitano, J. Wang, T. Ye, J. Li, Y. Kobayashi, K. Kishida, H. Abe, Y. Niwa, H. Yang, T. Tada, H. Hosono, *Nat. Catal.* **2018**, *1*, 178–185.

[7] D. G. Ivey, D. O. Northwood, *Z. Phys. Chem. N. F.* **1986**, *147*, 191–209.

[8] F. Stein, A. Leineweber, *J. Mater. Sci.* **2021**, *56*, 5321–5427.

[9] Y. Fukai, *The Metal-Hydrogen System: Basic Bulk Properties*, Springer-Verlag, Berlin Heidelberg, **2005**.

[10] Y. Watanuki, S. Morii, T. Kaneko, T. Toyama, Y. Kojima and N. Nishimiya, *J. Alloys Compd.* **2018**, *731*, 423–427.

[11] M. Itoh, K. I. Machida, K. Hirose, T. Sakata, H. Mori, G. Y. Adachi, *J. Phys. Chem. B* **1999**, *103*, 9498–9504.

[12] J. L. Soubeyroux, M. Bououdina, D. Fruchart, L. Pontonnier, *J. Alloys Compd.* **1995**, *219*, 48–54.

[13] K. Momma, F. Izumi, J. Appl. Crystallogr. 2011, 44, 1272-1276.

[14] H. Imoto, M. Sasaki, T. Saito and Y. Sasaki, *Bull. Chem. Soc. Jpn.* **1980**, *53*, 1584–1587.

[15] Y. Cao, A. Saito, Y. Kobayashi, H. Ubukata, Y. Tang, H. Kageyama, *ChemCatChem* **2021**, *13*, 191–195; Y. Kobayashi, Y. Tang, T. Kageyama, H. Yamashita, N. Masuda, S. Hosokawa, H. Kageyama, *J. Am. Chem. Soc.* **2017**, *139*, 18240–18246.

[16] K. Aika, K. Tamaru, *Ammonia: Catalysis and Manufacture*, Springer-Verlag, Berlin Heidelberg, **1995**.

[17] D. Shaltiel, I. Jacob, D. Davidov, *J. Less-Common Met.* **1977**, *53*, 117–131.

[18] M. G. Shelyapina, in *Handbook of Ecomaterials*, Springer International Publishing, Cham, **2018**, pp. 1–36.

[19] P. Wang, F. Chang, W. Gao, J. Guo, G. Wu, T. He, P. Chen, *Nat. Chem.* **2017**, *9*, 64–70.

Figures

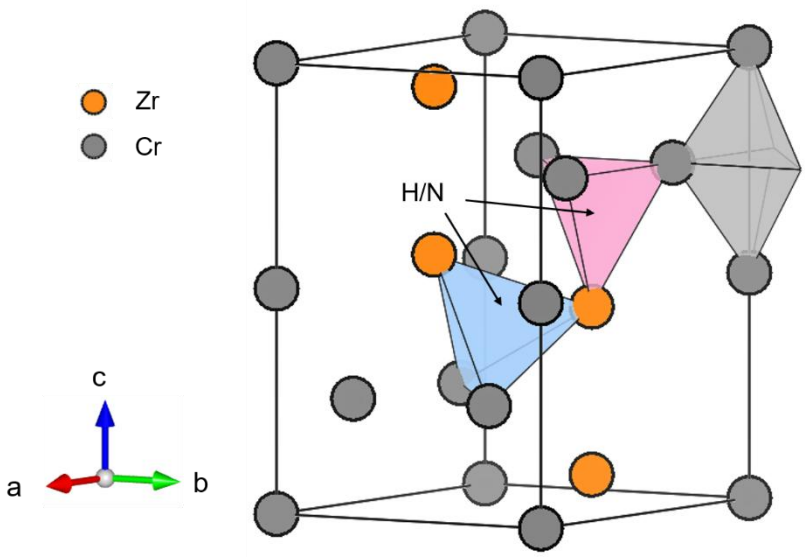

Figure 4-1. Crystal structure of $ZrCr_2$ (hexagonal C14 Laves phase). H/N atoms could insert into A_2B_2 (blue) and AB_3 (pink) tetrahedral sites, whereas no atoms occupy the B_4 (grey) tetrahedra.

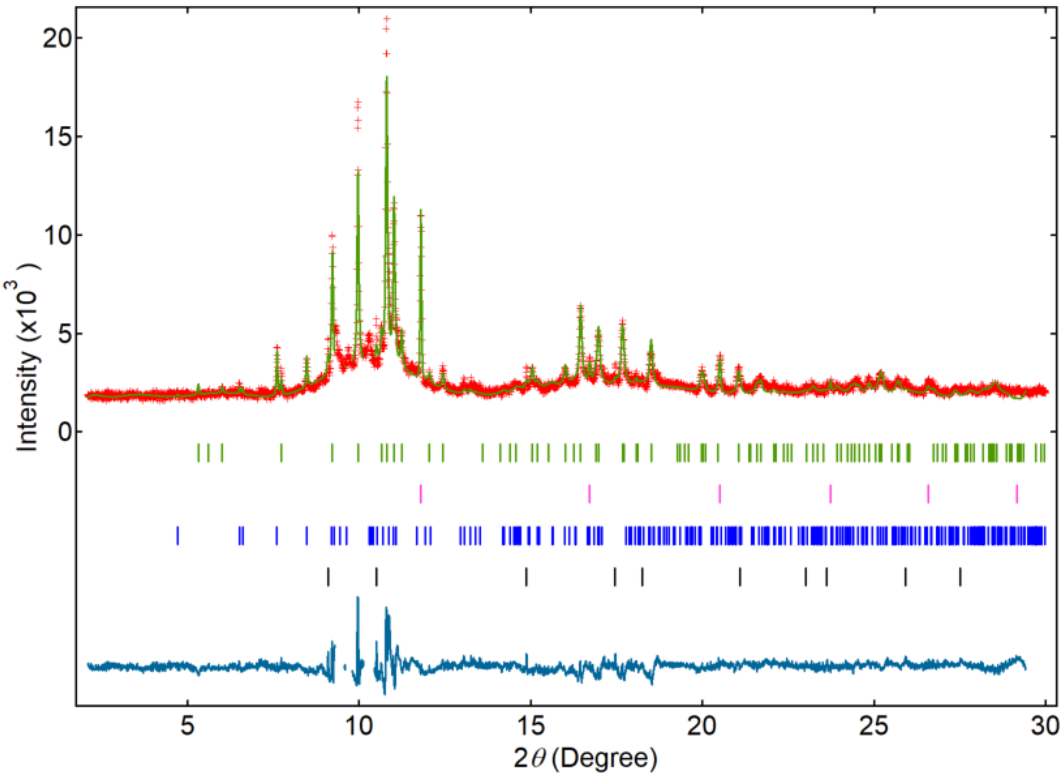

Figure 4-2. The Rietveld refinement of $ZrCr_2N_{0.46}H_{1.57}$ with Cr (11.6%), ZrO_2 (9.0%), and ZrN (1.9%) impurities. The green, pink, blue, and black color dashes represent calculated Bragg reflections for $ZrCr_2N_{0.4}H_{1.4}$, Cr, ZrO_2, and ZrN, respectively.

Table 4-1. Refined crystallographic parameters for the $ZrCr_2N_{0.46}H_{1.57}$ from SXRD refinements.

Atom	Site	*x*	*y*	*z*	Occ.	U_{iso}
Zr1	4*f*	0.3333	0.6667	0.0593(4)	1.000	0.001(1)
Cr1	2*a*	0	0	0	1.000	0.003(1)
Cr2	6*h*	0.8345(6)	0.6690	0.25	1.000	0.003(1)
N1	24*l*	0.0405	0.3298	0.5643	0.090	0.02
N2	12*k*	0.5417	0.0833	0.1270	0.280	0.02
N3	6*h*	0.4668	0.9336	0.25	0.420	0.02
N4	6h	0.2011	0.4022	0.25	0.260	0.02

Space group: $P6_3/mmc$ (a = 5.2243(1) Å, c = 8.5782(5) Å, R_p = 6.8%, R_{wp} = 8.6%, GOF = 4.33). H atoms were not considered in the SXRD analysis due to the insensitivity to X-rays. The position and the atomic displacement of N were fixed with the same values as those in the reported $ZrCr_2D_x$ with tetrahedral sites due to low quantity of XRD data.

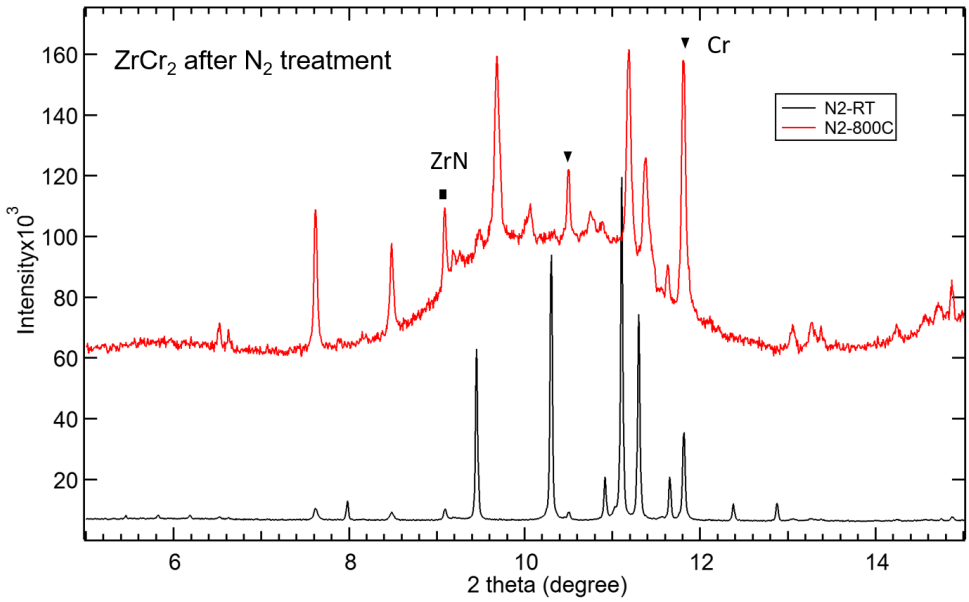

Figure 4-3. *In situ* SPXRD with N_2 up to 800 ^{o}C.

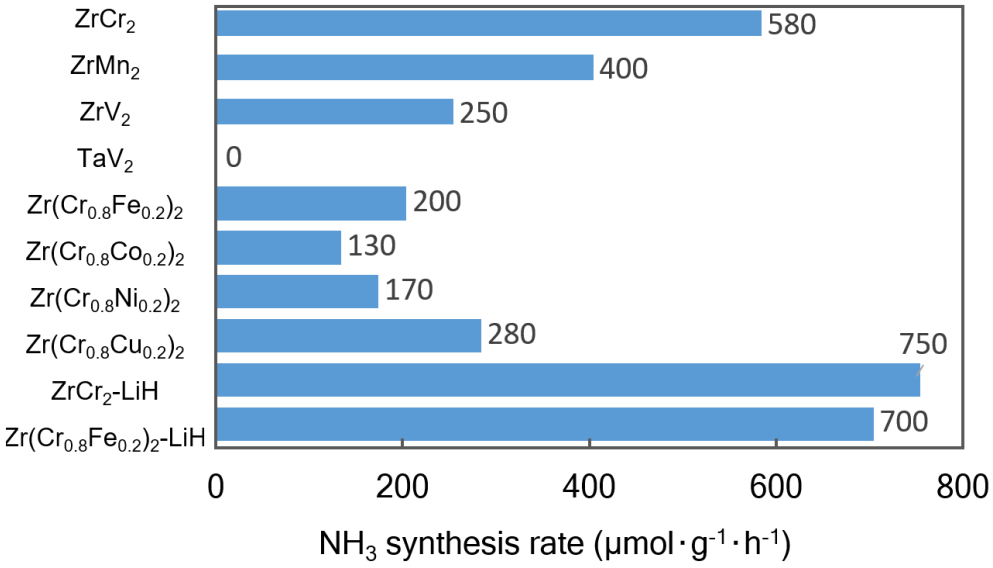

Figure 4-4. The catalytic performances of Zr-based AB_2-type intermetallics for ammonia synthesis under 3 MPa at 400 ^{o}C.

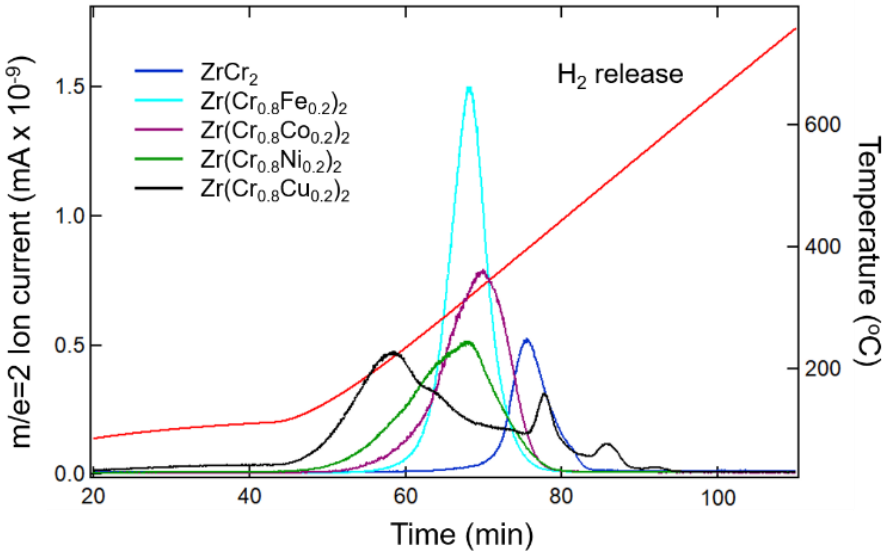

Figure 4-5. H_2 release experiments performed under flowing Ar (100 mL min^{-1}) at heating rates of 10 °C·min^{-1}. The red line is the temperature curve.

General Conclusion

Conclusion

Early 3*d* transition metals, such as Ti, V, or Nb are known to be inactive for the Haber-Bosch process, due to their strong M-N bonds. However, recently some early transition metal hydride compounds have been found to effectively counteract this effect, imparting catalytic activity on a wider range of elements. With these hydride catalysts, hydride (and nitride) bulk diffusion mechanisms have been proposed; if so, more open structures should enhance their activity. In Chapter 1, the author expanded the study to hydrides of other early transition metals, i.e., V and Nb. These metals benefit from body-centered cubic (bcc) related structures which enhance hydride diffusion, in addition to having relatively lower M-N bond strengths. The activity of vanadium hydride, most likely with an active composition of $VH_{0.44}N_{0.16}$, is superior to the previously reported TiH_2 and $BaTiO_{2.5}H_{0.5}$, and comparable to Cs-Ru/MgO at 400 °C under 5 MPa. These results show that there is more potential for developing new single-phase hydride catalysts of previously overlooked elements without sacrificing activity.

Topochemical reactions have led to great progress in the discovery of new metastable compounds with novel chemical and physical properties, making it an effective method of synthesizing new hydride materials. With these reactions, the overall crystal structure of the host material is generally maintained. In Chaper 2, the author reported a topochemical synthesis of a new hexagonal nitride hydride, *h*-Ca_3CrN_3H, by heating an orthorhombic nitride, *o*-Ca_3CrN_3, under hydrogen at 673 K, accompanied by a rotational structural transformation. The hydrogen intercalation modifies the Ca-N rock-salt-like atomic packing in *o*-Ca_3CrN_3 to a face-sharing octahedral chain in *h*-Ca_3CrN_3H, mimicking a 'hinged tessellation' movement. Impressively, the *h*-Ca_3CrN_3H exhibited stable ammonia synthesis activity when used as a catalyst, even though the early transition metal Cr is not an active element for ammonia synthesis.

In Chapter 3, the author further examined the catalytic performance of this new Ca_3CrN_3H compound and when it is used as a catalyst support for Ru. Ca_3CrN_3H exhibits good ammonia synthesis activity and the absence of hydrogen poisoning is presumably associated with the facile hydride diffusion within face-shared 1-D octahedral channel of Ca_3CrN_3H, as well as the superior hydrogen exchangeability of lattice hydride with reactant H_2 gas. DFT calculations reveal that nitrogen reduction could be effectively achieved through an associative mechanism. The surface Ca_3 hollow sites formed at the Ca_3CrN_3H (001) surface play a critical role in N_2 adsorption and activation to the successive hydrogenation. The topochemical synthesis of *h*-Ca_3CrN_3H and the following catalytic application encourage the expansion and exploration of a large group of A_3MN_3H hexagonal antiperovskite nitride-hydride materials as promising ammonia synthesis catalysts.

AB_2-type intermetallic compounds, such as $ZrCr_2$, etc., are of great interest for hydrogen storage. In Chapter 4, the author found a dissociative hydrogen chemisorption together with nitrogen storage proceed on Laves phase compounds to form intermetallic nitride hydrides, which exhibit the potential as ammonia synthesis catalysts. However, these catalysts have low surface area and insufficient activity so far. For the application of hydrogen storage alloys for ammonia synthesis, further investigations could be focused on the further activity promotion with electropositive

elements, such as barium which has previously been demonstrated to be excellent promoter for Ru or Fe-based catalysts.

Outlook

Hydride materials have drawn great attention as promising ammonia synthesis catalysts with unique advantages such as exhibiting superior catalytic performance, breaking scaling rules, and preventing H poisoning effect. However, there still a long way to go from fundamental research to achieve practical application. The target for the future development of hydride catalysts will aim at synthesizing new hydride compounds and expanding the scope of catalytically active metals; realizing efficient ammonia synthesis under low pressure and temperature; using earth abundant transition metals with low cost and superior catalytic activity; improving robustness and stability of the hydride catalysts which are usually air and/or moisture sensitive.

Topochemical reactions have led to great progress in the discovery of new metastable compounds with novel chemical and physical properties. With these reactions, the synthesis of new mixed-anion hydride materials is possible, encouraging the expansion and exploration of a large group of hydride compounds as promising ammonia synthesis catalysts. In addition, there is still much to discover about the scientific principles and technological applications of early transition metal hydrides for ammonia synthesis, such as the metal support interaction, promoter effects, catalysts morphology. Moreover, advanced characterization techniques such as *in-situ* electron microscopy, synchrotron X-ray Absorption, etc., will also provide key mechanistic information for catalyst structure and reaction intermediates. Computational guidance could also be important for catalyst design and the understanding of reaction mechanism.

Publications

[1] Topochemical Synthesis of Ca_3CrN_3H Involving a Rotational Structural Transformation for Catalytic Ammonia Synthesis

Yu Cao, Maria A. Kirsanova, Masayuki Ochi, Walid Al Maksoud, Tong Zhu, Rohit Rai, Shenghan Gao, Tatsuya Tsumori, Shintaro Kobayashi, Shogo Kawaguchi, Edy Abou-Hamad, Kazuhiko Kuroki, Cédric Tassel, Artem M. Abakumov, Yoji Kobayashi,* and Hiroshi Kageyama*

Angew. Chem. Int. Ed. **2022**, *61*, e202209187

[2] Vanadium Hydride as an Ammonia Synthesis Catalyst

Yu Cao, Ayaka Saito, Yoji Kobayashi,* Hiroki Ubukata, Ya Tang, and Hiroshi Kageyama*

ChemCatChem **2021**, *13*, 191–195

[3] Ca_3CrN_3H Catalyzed Ammonia Synthesis via an Associative Mechanism

Yu Cao, Ekaterina Toshcheva, Walid Almaksoud, Rafia Ahmad, Tatsuya Tsumori, Ya Tang, Rohit Rai, Luigi Cavallo, Yoji Kobayashi,* and Hiroshi Kageyama*

ChemSusChem, submitted.

[4] Zr-based Laves Phase with Nitride/hydride Anions for Ammonia Synthesis

Yu Cao, Yoji Kobayashi,* and Hiroshi Kageyama*

In preparation

[5] Dehydration of Electrochemically Protonated Oxide: $SrCoO_2$ with Square Spin Tubes

Hao-Bo Li, Shunsuke Kobayashi, Chengchao Zhong, Morito Namba, **Yu Cao**, Daichi Kato, Yoshinori Kotani, Qianmei Lin, Maokun Wu, Wei-Hua Wang, Masaki Kobayashi, Koji Fujita, Cédric Tassel, Takahito Terashima, Akihide Kuwabara, Yoji Kobayashi, Hiroshi Takatsu,* and Hiroshi Kageyama*

J. Am. Chem. Soc. **2021**, *143*, 17517−17525

[6] ヒドリド化合物によるアンモニア合成 Ammonia Synthesis with Hydrides

小林 洋治, 唐 亜, **曹 禹**, 陰山 洋

セラミックス **2020**, *55*, 274-278

Acknowledgments

Per Aspera Ad Astra

穿过逆境，抵达繁星

It has been an incredible honor and pleasure studying in Kageyama lab, with so many excellent people and challenging projects. Most importantly I would like to say a massively huge thanks to my supervisor Kageyama sensei. With his passion of scientific research, wisdom, diligence, he is a professional model and a shining example to all the younger people, showing us how to behave as an excellent researcher. He is also a constant source of encouragement for giving me the inspiration and confidence to pursue a PhD. Always inspire me to try new things and motivate me to keep challenging myself. Under his guidance, after three years of study, I really gained a lot and opened up more possibilities in my life. Every important node is inseparable from his kind help and support.

Secondly, I would like to express my sincere thanks to Kobayashi sensei (KAUST). I have spent unforgettable nine months in Saudi Arabia as a visiting student in Kobayashi group. I could not have wished to work for a more kind, talented or supportive person and I am so thankful for all the help and guidance he has given me over the years, from Kyoto to KAUST. He is a constant source of support and inspiration. Thanks for the patience and tolerance all the time, putting up with me for so many silly questions and help me grow into a better me. Couldn't have done it without you.

A huge thanks to all the members of the Kageyama group, Prof. Cedric, Prof. Takatsu, Dr. Kato, Dr. Kageyama, Dr. Haobo, Dr. Shou, Dr. Tong, Dr. Ding, Dr. Sasahara, Watanabe, Arai, Ishida, Ubukata, Gao, Namba, Xia, Yang, Zheng, Wei, Murayama, Taguro, Okada, Goto, Kawai, Tsumori, Terada, Matsuzaki, Qianmei, Sijia, Okuda, etc. for their kind help and company. Special thanks to secretary Ms. Nojiri, Ms. Kataoka and Ms. Aoki for their strong support all the time. A massive thank you goes to all the members of the Kobayashi group, Dr. Walid, Dr. Rohit, Dr. Vijaykumar, Marcell, Yuvraj, Bogdan, for all the great help and friendship during my visit in KAUST. Further afield thanks to my research collaborates for all their help at the experiments and theoretical

calculations. The author is grateful for the financial support from Japan Society of the Promotion of Science (JSPS) for Young Scientists.

Finally, I need to thank all my good friends for the constant pep talks and laughter. Thanks to Gao, Wei, Tong, Shou, Ding, Haobo, Zheng, Xia, Yang, Bian, you are amazing and little rays of sunshine. Thanks to my friends in KAUST, Xiaofei, Huiwen, Chengyang, Yan, Mengmeng, Haicheng, Hong, Xueli, Xueqin, Teng, Qinpeng, for all the fun and laughter. Thanks so much to my parents for their love and support all the time. Because of the COVID-19, I have not been home for more than three years. Thank you to those who have always been there for me, listening to my troubles and share my happiness.

When looking back on the past three years, I was thinking about the meaning of this experience and keep asking myself questions about what is my growth and progress. Has the original goal been achieved? Am I still on the path to self-realization? After some tough times, I admit it is hard to start in a new direction, but I still believe it is worth trying because it will help gain experience and broaden horizons. It is the necessary scientific training to lay a solid and comprehensive foundation that sparks academic crossovers. Just like what Kageyama sensei mention in his review (Nature Comm. 2018, 9, 772), Mixed is Different. The goal will be finally attained through dauntless and persistent efforts. As a result, confidence increases. Catalytic synthesis of ammonia is a never-ending story, so is friendship, courage, growth and the polishing of personality. To face challenges, overcome difficulties and surmount the storms. To establish a balance between life and work, and find a career direction for the future. The realization of dreams is a step-by-step process. Failure and pain sharpen a more peaceful mind and stronger heart. I could say it is a wonderful journey, and I really have a lot of fun.

Thank you very much!

Yu

2022/12